UNIVERSITÄT BONN
Physikalisches Institut

Measurement of electron production from cosmic rays in the ATLAS detector

by
Jana Kraus

The special topology of cosmic events traversing all subdetectors offers the unique opportunity to investigate the combined performance of the ATLAS detector in identifying and reconstructing particles before first proton collisions at the LHC.
Through interaction with the inner detector material or through decays high-energy electrons can be produced from the traversing cosmic muons. A sample of 3.5 million cosmic ray events with a high-level trigger track candidate in the central part of the inner detector is used as a basis to extract the electrons from the different processes. To separate the electrons from the large background of muon bremsstrahlung among the about 10000 candidates, the characteristic properties of electrons in the detector are exploited accounting for the special nature of cosmic events. The resulting extraction of about 34 electrons mainly originating from ionisations enables an observation and investigation of real electrons in the ATLAS detector for the first time.

Post address:
Nussallee 12
53115 Bonn
Germany

BONN-IB-2010-01
Bonn University
January 2010

UNIVERSITÄT BONN
Physikalisches Institut

Measurement of electron production from cosmic rays in the ATLAS detector

von
Jana Kraus

Dieser Forschungsbericht wurde als Diplomarbeit von der Mathematisch - Naturwissenschaftlichen Fakultät der Universität Bonn angenommen.

Angenommen am:	11. Januar 2010
Referent:	Prof. Norbert Wermes
Korreferent:	Prof. Klaus Desch

Contents

1 Introduction

The Large Hadron Collider in Geneva is the first machine which will advance to center-of-mass energies in the TeV scale in proton-proton collisions. The main goal of its experiments, including the ATLAS detector, is the discovery of the Higgs particle, which has so far only been predicted in theory as an essential completion of the Standard Model to explain the origin of particle masses. In addition, the LHC offers the possibility to search for other new physics phenomena such as supersymmetry. However, the particles of interest cannot be detected directly in the detector as most of them immediately decay due to their large masses. Instead, they are recognized by their decay products: The invariant mass of these provides a direct access to the initial particle's mass. Leptons, especially electrons, play a crucial role as final state particles in nearly all important decay channels, e.g. $H \rightarrow WW^{(*)} \rightarrow l\nu l\nu$ or $H \rightarrow \tau\tau \rightarrow l\nu\nu l\nu\nu$.

Electrons leave a clear signature in the ATLAS detector - an isolated track in the Inner Detector and a shower in the Electromagnetic Calorimeter providing two independent measurements of momentum and energy. Therefore, they can easily be distinguished from the large background of hadronic particle showers and are good candidates to trigger on. The possibility to measure transition radiation in the Inner Detector offers an additional tool to identify them. Also in the early phase of data taking at the ATLAS detector, electrons are important observables for the exact measurement of various Standard Model parameters, for instance in the decay of Z and W bosons or τ leptons.

Since the interesting physics processes have cross sections which are several orders-of-magnitude smaller than the total proton-proton interaction cross section, an effective and accurate measurement of the final state particles including electrons needs to be ensured to draw reliable conclusions from an analysis of the data. One of the first important tasks of the ATLAS detector therefore is to verify and optimize the reconstruction and identification of electrons.

Although the LHC has only started taking collision data recently, the detectors have already been commissioned with cosmic rays as a permanent source of high-energy particles. Several hundred million events have already been recorded with the ATLAS detector. The special topology of cosmic muon events which cross the full profile of the ATLAS detector from top to bottom and are distributed over the full detector volume, offers the unique possibility to commission and improve the individual performance of all detector subsystems and to verify their combined performance in the detection of particles before the first collisions. In particular, cosmic muons traversing the ATLAS detector can interact with the material or decay and produce high-energy electrons. The recorded cosmic data can therefore be used to study for the first time the performance of ATLAS finding and extracting electrons which is the aim of this diploma thesis.

The three electron processes and their different signatures in the detector are therefore analysed, which are muon decay, knock-on of delta electrons and conversion of bremsstrahlung photons. An estimate of the expected number of high-energy electrons from these processes is obtained from an analytical calculation and the investigation of the truth electrons in a cosmic Monte Carlo sample. In addition, possibly occurring background processes are examined which might fake an electron candidate, such as muon bremsstrahlung.

A data sample of 3.5 million cosmic events featuring a high-level trigger track candidate in the Inner Detector which was recorded with ATLAS in autumn 2008 is used as a basis to extract the electrons from the different processes. To separate the real electrons from the background among the about 10000 candidates, their signature in the detector is exploited, and the ATLAS standard cut-based method for the identification of electrons is applied. The latter makes use of characteristic properties of the electron track and shower and needs to be adapted to the special topology of the cosmic events. The remaining sample of electrons is investigated in detail and a method is developed to estimate the contamination with background events. Finally, the analysis applied to the data sample is tested on a sample of ca. 10 million simulated cosmic events, to back up the obtained results. Furthermore, the exact cut efficiencies for an electron identification are extracted to compare the results with the theoretical expectation.

The thesis is organized as follows: In section 2, 3 and 4 an overview of cosmic rays, the ATLAS detector components and the different reconstruction algorithms as an ingredient for electron detection are discussed, focussing on the differences and necessary adjustments which arise from the special topology of cosmic events. A short description of the simulation of cosmic events is given in section 5. The possible production processes for electrons are investigated in detail in section 6. The analysis of the cosmic ray data sample is presented in section 7, explaining the applied method to isolate a sample of electrons and the results obtained. In section 8 the comparison to a sample of simulated cosmic events is described, including the determination and discussion of the cut efficiencies. A conclusion of the results is provided in section 9.

2 Cosmic rays

Primary and secondary cosmic rays in outer space

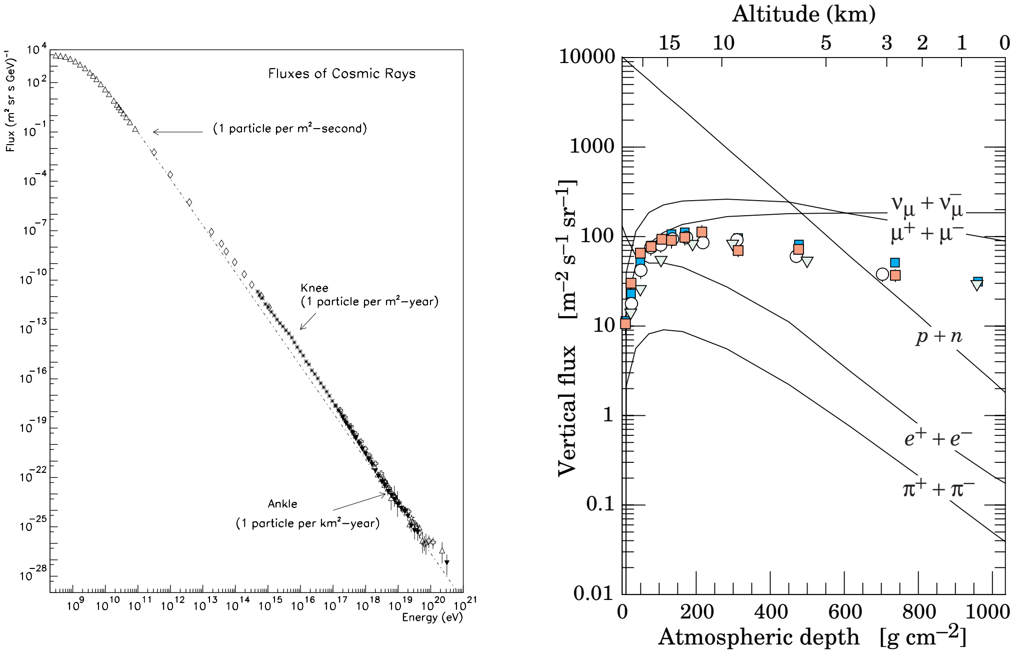

Figure 2.1: Left: Particle spectrum of cosmic rays [1]. Right: Vertical fluxes of cosmic rays in the atmosphere. The data points show measurements of negative muons [2].

Cosmic ray particles come from different astrophysical sources and penetrate the atmosphere of the earth with a frequency of 1000 $\mathrm{m}^{-2}\,\mathrm{s}^{-1}$. They were first discovered by Hess and Kohlhörster in 1912 as ionizing particles during measurements on hot-air balloon flights. A lot of research is still done on the different kinds of sources of cosmic rays and the exact explanation for propagation and acceleration processes in the universe.

The cosmic rays consist mainly of ionized nuclei (98%) and additionally of other stable particles which have a lifetime of 10^6 years or longer, such as electrons, positrons, gammas or neutrons [3]. Among the nuclei, 87% are protons, 12% alpha particles and 1% are heavier elements. One distinguishes between primary and secondary particles. Primary cosmic rays are nuclei and electrons which originate from stellar sources. On their way through space they interact with the interstellar gas and produce secondary particles for instance through the spallation of nuclei[1]. This explains the abundance of elements like lithium or berrylium among the cosmic ray particles which are usually not products of stellar sythesis. At small rates also antiparticles, positrons and antiprotons ($< 10^{-4}$), are produced in interactions of the primary particles with matter[2].

[1]The distinction between primary and secondary particles produced in the universe is chosen in this thesis according to [2]. In other sources, all particles arriving at the earth's atmosphere are referred to as *primaries*, and the particles which are produced in interaction with the earth's atmosphere are called *secondaries*.

[2]Whether an even smaller fraction of the anti-protons may be part of the primary rays is of current interest, since these could be the decay products of supersymmetric dark matter candidates [4].

The energies of the cosmic rays range from several 100 MeV to 300 EeV which is $3 \cdot 10^{20}$ eV [5]. The spectrum can be seen in fig. 2.1 (left). Up to the so called *knee* at 10^{15} eV, the number of particles decreases proportional to $\mathrm{E}^{-2.7}$. Above this, the spectrum gets steeper up to the *ankle* at 10^{18} eV where it changes slope again. This behaviour can be understood considering the different astrophysical sources from which particles can only be produced up to a certain energy.

Some cosmic rays are produced by the sun, associated with solar flares. These are eruptions of magnetic plasma at the sun where a large amount matter is emitted. Most cosmic ray sources, however, are of extrasolar nature such as explosions of supernovae, pulsars or neutrons stars which all emit highly accelerated particles [5], [6]. The acceleration can be explained by diverse processes, e.g. by the moving of magnetic plasmas or shock waves from Supernova explosions [3]. The extremely high-energy cosmic rays are believed to originate from outside our galaxy, for instance from active cores of other galaxies. Charged cosmic particles are affected by the inhomogeneous galactical magnetic field which influences their trajectories and velocities. Near the earth's atmosphere, especially the low-energy charged cosmic ray particles are decelerated and deflected the time dependent magnetic activity of the sun in sun winds and the geomagnetic field. As a consequence, the exact intensity spectrum of cosmic rays is always time and location dependent. The deflection of the particles through magnetic fields and their interactions with matter also are a reason why identifying their origins is still a challenge.

Cosmic rays in interaction with the earth atmosphere

When cosmic rays penetrate the atmosphere of the earth at a height larger than 20 km above sea level, they interact with the air molecules and produce new cascades of particles which also undergo energy-loss and decay processes on their propagation towards the surface of the earth [2]. If a proton or nucleus of the primary rays collides with an air molecule and interacts with one of the nucleons, lighter particles are produced which are mainly kaons or pions as they are the lightest mesons. They either interact with other particles in the atmosphere afterwards, or they decay ($\tau_{K^\pm} = 1.2 \cdot 10^{-8}$s, $\tau_{\pi^\pm} = 2.6 \cdot 10^{-8}$s, $\tau_{\pi^0} = 8.4 \cdot 10^{-17}$s, [7]). Kaons can decay to pions or directly to muons. Charged pions decay nearly exclusively to muons and neutrinos, while neutral pions immediately turn into two photons. The main decay channels are listed here with the corresponding branching ratios [8], [7]:

$$
\begin{array}{rcll}
K^\pm & \to & \mu^\pm + \nu_\mu & (63.5\%) \\
\pi^\pm & \to & \mu^\pm + \nu_\mu & (\tilde{1}00\%) \\
\pi^0 & \to & \gamma\gamma & (98.8\%)
\end{array}
$$

The photons produced from the neutral pions at high energies undergo pair production with high probability near the Coulomb field of a nucleus. The resulting high-energy positrons and electrons lose energy via bremsstrahlung which leads to the development of an electromagnetic shower. The produced muons can also decay further to electrons which the evolve in electromagnetic particle cascades:

$$\mu^\pm \to e^\pm + \nu_\mu + \nu_e \quad (100\%) \tag{2.1}$$

The exact propagation and flux of cosmic ray particles in the atmosphere is dependent on all the different interaction and decay probabilities, the energy spectrum and the structure of the atmosphere. The development of the different particle fluxes with decreasing height above sea level is shown in fig. 2.1 (right). The interaction probability for electrons and photons in electromagnetic cascades and for protons, neutrons, kaons and pions in hadronic cascades is large. Therefore, their flux decreases with increasing atmospheric depth. In contrast, the muon flux stays nearly constant and the neutrino flux even increases due to their small interaction probability in matter.

Cosmic rays at sea level

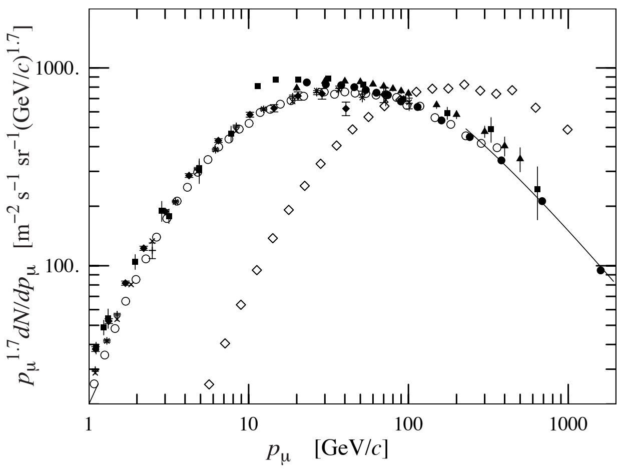

Figure 2.2: Momentum spectrum of cosmic muons at sea level (scaled with $p_\mu^{1.7}$) for an incident zenith angle of $\theta = 0°$ (black symbols and white circles) and $\theta = 75°$ (white squares) [2].

As discussed before, due to the interaction processes of the cosmic rays in the atmosphere, most of them do not reach the surface of the earth. Besides the neutrinos, only muons are still very numerous at sea level and make up 80% of the charged particle flux [2]. This results from the fact that muons lose their energy mostly via ionization processes as minimum ionizing particles and thus their energy decreases on average only by 2 GeV for the whole path through the atmosphere. In addition, they are highly relativistic particles and have a relatively long life time of $2.2 \cdot 10^{-6}$s. As a consequence, muons with energies above 10 GeV can cross the distance from the top of the atmosphere where they are produced to the sea level without decaying. A 5 GeV muon, for instance, already has a decay length of 30 km which is only slightly reduced by energy losses on the way.

The total flux for different energies is a convolution of production, ionization and decay probabilities. Their spectrum can be seen in fig. 2.2. At lower energies (< 10 GeV), it is dominated by muon interaction and decay probabilities, towards larger energies it is mostly influenced by the spectrum of the primary cosmic rays. At very large energies (>100 GeV) it decreases much steeper as pions and kaons of this energy tend to rather interact than decay. As it can be noticed in fig. 2.2, the spectrum also depends on the zenith angle, the incident angle of the muon with respect to the surface of the earth. The larger this angle, the longer is the distance muons travel through the atmosphere. As a consequence, also the probability becomes larger that low-energy muons decay on their way and that muons with higher energies are produced by decaying mesons. The spectrum thus shifts towards higher energies. The angular distribution of the intensity at sea level is given by $I_\mu(\theta) = I_\mu(0)\cos^2\theta$ in general. The intensity integrated over all energies for vertical muons above 1 GeV is $I = 70$ m^{-2}s^{-1}sr^{-1} at the sea level. The integral over the angular distribution yields an intensity of $I \approx 1$ cm^{-2}min^{-1} [2].

Also to be mentioned is the charge ratio of positively and negatively charged cosmic muons which is different from one. Since the primary spectrum of cosmic rays consists mainly of protons, an excess of positively charged mesons is produced from the interactions in the atmosphere. This charge imbalance of kaons and pions transfers directly to the muons as their decay products.At Cern, the cosmic muon charge ratio was measured to be $N_{\mu^+}/N_{\mu^-} \approx 1.25$ for energies below 100 GeV with an increasing tendency towards higher muon energies [9].

Other components of the cosmic rays with much smaller intensities at the surface of the earth are electrons, positrons, mesons, neutrons and protons or other nucleons from the primary rays.

Cosmic rays penetrating underground

Of the known particles, only cosmic muons and neutrinos can penetrate to significant depths underground. The other particles have too short ranges in solid matter and lose their energy very quickly. Muons undergo energy losses mainly through ionization and also through bremsstrahlung at higher energies [5],[2].

Their intensity as a function of depth is a combination of their flux spectrum at the surface and the rate of their energy losses [10]. Average rock properties (nucleus charge $Z = 11$, atomic mass $A = 22$ and density $\rho = 2.65\text{g/cm}^3$) can be assumed to calculate the muon intensity at a certain depth, see fig. 2.3. For the ATLAS detector at the LHC (see next chapter) which is situated in a cavern underground and has an overburden of about 80 m of rocks, the intensity integrated over the energy spectrum of vertical muons reaching the detector is ca. 0.5 m^{-2} s^{-1} sr^{-1}. Integrated over the angular distribution which is roughly the same as at the surface, the intensity of cosmic muons is $\text{I} = 1\text{m}^{-2}\text{s}^{-1}$ [10]. This is more than two orders of magnitude smaller than at the surface.

However, the area above the ATLAS detector does not entirely consist of dense rocks since two large supply shafts are situated above it. A lot of low-energy muons can access the detector through these shafts without being attenuated in the rock. This modifies the intensity spectrum and also the angular distribution of the incoming cosmic muons (see sec. 4.2).

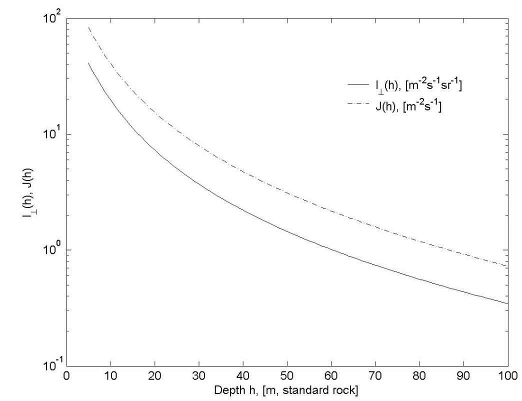

Figure 2.3: Muon flux at shallow depths underground, shown is the vertical intensity $I_\perp$ and the integral of the muon flux J versus the standard rock overburden [10]

3 The LHC and the ATLAS detector

3.1 The LHC

The Large Hadron Collider is a proton-proton-collider which is situated about 100 m underground in a tunnel at CERN near Geneva (see fig. 3.1). It was built with the purpose to advance to the high-energy frontier of particle physics where on the one hand precise measurements of different Standard Model parameters can be provided, and on the other hand new physics phenomena may be discovered. It is foreseen to accelerate protons up to a center of mass energy of 14 TeV which are injected in opposite directions in a ring with a circumference of 27 km. They are brought to collision at four interaction points where four main detectors were built for different purposes in order to study the results.

The aspired luminosity is $10^{34}\mathrm{cm}^{-2}\mathrm{s}^{-1}$, although for the first several years it is anticipated that the LHC will be operated at lower energies (7-10 TeV) and luminosities. The LHC has only recently started to take data with proton beam collisions, but the detectors have already been commissioned with a large amount of cosmic ray events.

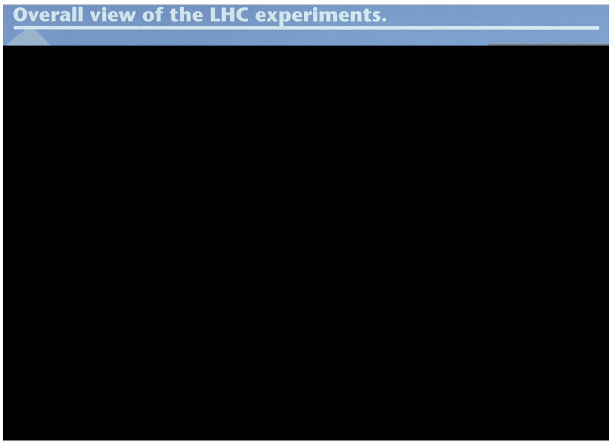

Figure 3.1: The LHC and its detectors [11]

3.2 The ATLAS detector

The ATLAS detector (**A** **T**oroidal **L**HC **A**pparatu**S**) is one of the four main experiments at the LHC which was built as a general purpose detector to study proton-proton collisions. It consists of three main detector subsystems (fig. 3.2) which are arranged in cylindrical shapes around the beam pipe. In combination they cover nearly hermetically the whole angular space and provide precise measurement of energies and momenta for all kinds of particles [12].

For cosmic events, more precisely muons, a combined detection and measuring in all subsystems is necessary, because muons are at not too high energies minimum ionizing particles [13]. This means they only lose a small fraction of their energy in the inner subsystems and cross in most cases the full volume of the ATLAS detector including the outmost Muon Spectrometer (MS). For electrons the inner tracking detector (ID) and the Electromagnetic Calorimeter (EM) are of largest importance for exact momentum and energy measurements. A summary of all detector components from inside out will be given in the following, as well as a list of the commonly used variables and coordinates to describe particles within the ATLAS detector geometry.

Important variables

The coordinate system used for ATLAS is the following [12]: The interaction point of the two protons is defined as the origin of the coordinate system. The direction of the proton beam in the beam pipe is defined as the positive z axis. The x axis is pointing towards the center of the LHC ring and the y axis points upwards. Particles are often described in a polar coordinate system - by their radial distance from the beam line, the azimuthal angle in the transverse plane of the detector ϕ and the pseudorapidity $\eta = -\ln\tan\frac{\theta}{2}$ which is derived from the polar angle θ with respect to the z axis. A general measure for angular distances in ATLAS is therefore $\Delta R = \sqrt{\Delta\phi^2 + \Delta\eta^2}$.

In proton-proton collisions not the particles themselves but their partons, quarks or gluons, interact which carry an only theoretically accessible fraction of the proton's momentum. The longitudinal component of the total momentum is therefore difficult to measure. Because of that, most quantities in ATLAS are examined only in the transverse plane since in this direction the total momentum can be assumed to be zero before the interaction of the partons. The variables $p_T = \sqrt{p_x^2 + p_y^2}$ or E_T denote for instance the transverse momentum or energy. Thus, many thresholds and cuts are applied only to the transverse component of these variables. For cosmic events these kinematical constraints cannot be applied. Nevertheless, to be able to compare the performance of the analysis for cosmics with collision events, the examined variables will be chosen conform to what would be used in collision data.

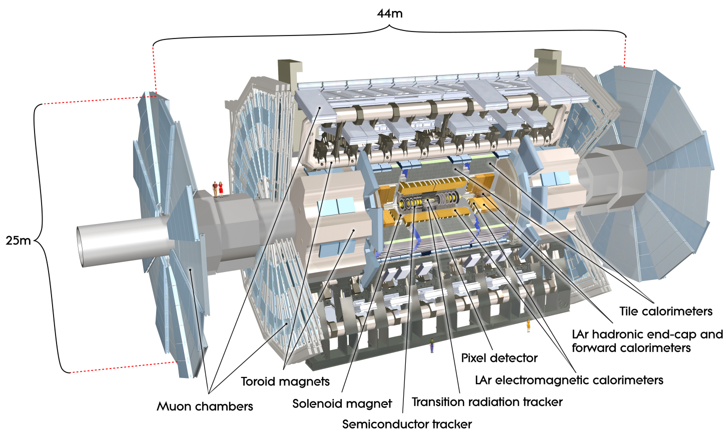

Figure 3.2: The ATLAS detector [11]

Inner Detector

The Inner Detector provides precision measurements of charged particle tracks. In addition, it is enclosed by a superconducting solenoid which constitutes a magnetic field of 2 T parallel to the beam axis. This causes a bending of the particle trajectories in the transverse plane, and from the radius of curvature a momentum and charge measurement is obtained. The Inner Detector consists of three detection subsystems [12], separated into a central region (barrel) and two front and rear regions (end-caps), a sketch is shown in fig. 3.3.

Closest to the beam line the silicon **Pixel Detector** is situated, a semiconductor detector. It consists of three cylindrical layers in the barrel region and three disks in each end-cap region. With a pixel size of 50 $\times$ 400 μm^2 (in $R - \phi \times$ z) they offer very precise track and vertex measurements which is important, for example, for the reconstruction of photon conversions and future identification of b quark hadron or τ candidates with short lifetimes which decay close to the primary vertex.

The next subdetector is also a semiconductor detector, the **Silicon Microstrip Detector (SCT)** consisting of four layers of microstrips in the barrel region parallel to the beam axis and nine disks at each side in the end-caps. The strips have a pitch of 80 μm. They provide a precise position measurement in the R-ϕ plane. A measurement of the z coordinate is obtained via a small stereo angle between the two surfaces of each layer.

The outermost part of the ID is the large **Transition Radiation Tracker (TRT)**. It consists of several thousand straw tubes filled with a Xenon based gas mixture which are in principle proportional counters [14]. They have a diameter of 4 mm and are 144 cm long in the barrel region. Thus, only an accurate position measurement in the transverse plane can be obtained for charged particles in the barrel part, not in z direction. This is a small drawback for cosmic events as in many cases the silicon detectors are not crossed, and thus only the transverse components of the track can be measured.

The TRT has an additional feature which is very important for the identification of electrons. Between the straw tubes polypropylene fibres or foils are included which cause the emission of transition radiation [15]. It occurs when particles traverse the interface of two media with different dielectric constants. The emission probability depends on the particle's Lorentz boost factor $\gamma = E/m$ and therefore plays an important role in differentiating muon tracks from electron tracks in cosmic data. The transition radiation photons are also detected inside the straw tubes and cause a signal with a higher amplitude than the signal of the ionizing particles themselves. By applying two different thresholds on the signal, the fraction of high threshold hits from transition radiation with respect to the total number of low threshold TRT hits for each particle can be determined and be used as a discriminating variable for particle identification.

In total, the combination of fine granularity semiconductor trackers and the TRT providing a large amount of space points at larger distances ensures an optimal resolution and track reconstruction, at the same time keeping the amount of material crossed by the particles as small as possible and thus reducing energy losses through bremsstrahlung in the ID. A cosmic muon that crosses each subdetector centrally in the upper and lower hemisphere, will typically have about 6 Pixel hits, 8 SCT hits and 72 TRT hits, twice as much as a typical collision track.

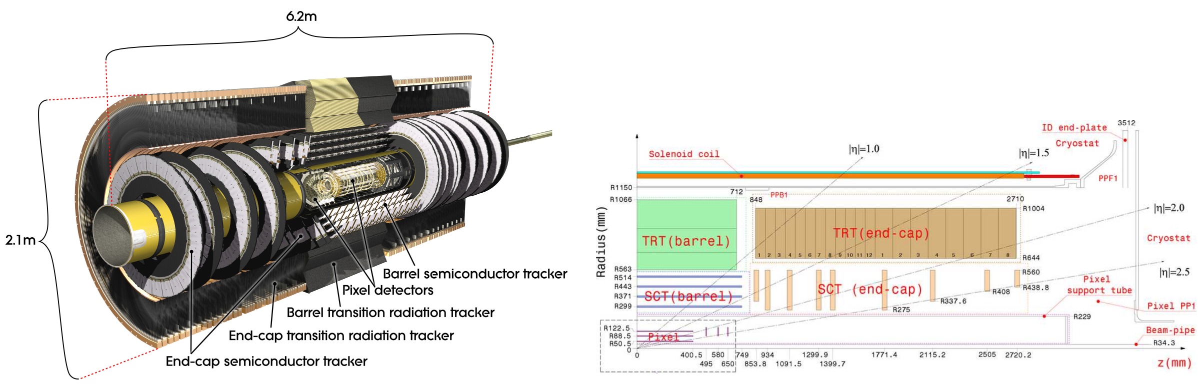

Figure 3.3: Inner Detector. Left: Cut away view. Right: Plan view of a quarter section. [12]

Calorimeter

The Calorimetry which is situated outside the Inner Detector and solenoid envelope, is essential for precise energy measurements of different kinds of particles [12] (see fig. 3.4 (left)). Therefore, it has to cover a large η region (< 4.9) and be nearly hermetic. It is also separated in a barrel and two end-cap regions.

The inner **Electromagnetic Calorimeter** with a very fine granularity serves as a measurement device for electrons and photons. It makes use of their high interaction probability via pair production and bremsstrahlung at high energies in matter. This causes the formation of particle showers that can be detected. The radiation length (X_0) is a measure for the longitudinal extension of the shower, depending on the material. All Calorimeters in ATLAS are so called sampling calorimeters where passive and active material for absorption and detection of showering particles are arranged in alternating order [14]. The EM is designed in a special accordion shape which provides short drift paths and is thus suited for high particle rates. The active material are chambers filled with Liquid Argon (LAr) in which the ionizing particles of the showers are detected, and the passive absorption material is lead [16].

The EM barrel consists of three layers in depth and an additional Presampler in front of the Calorimeter used to correct for the energy losses in the Inner Detector and the solenoid region. A picture of the detailed segmentation can be seen in fig. 3.4 (right). The first layer consists of strips with a size of $\Delta\eta \times \Delta\phi = 0.003 \times 0.1$, thus it has a very fine granularity in η. The second layer consists of cells of size 0.025×0.025. Both contain the main part of the shower and provide also precise position measurements. In the third layer which is only reached by electrons or photons with high energies, the cells have a size of 0.05×0.025. All cells point towards the interaction point in both angular coordinates. Therefore, the direction of electromagnetic showers in cosmic data can differ strongly from the symmetry axes of the cells in contrast to collision events (see sec. 4.3.1). The EM end-caps consist of two layers with a slightly coarser granularity.

The coarser and larger **Hadronic Calorimeter (HCal)** will be used for energy measurements of the hadronic component of jets and missing transverse energy.[3] For cosmic data it plays only an inferior role, as muons as minimum ionizing particles only leave a small fraction of their energy in the Hadronic Calorimeter, and electrons have already lost nearly their entire energy in the EM.

In the barrel region, tiles of scintillators are used as detection material and steel as absorber material, while in the end-cap regions the HCal consists of copper and LAr gaps [16].

Muon Spectrometer

The outermost part of the ATLAS detector is the **Muon Spectrometer** which was designed for precision momentum and position measurements of muons as all other particles should have lost their complete energy by showering in the Calorimeters before [12], [17]. Due to their large mass, muons lose their energy primarily by ionization and leave only a small fraction of their energy in the inner parts of the detector. Thus a large detector volume is needed to track them. A plan view of the MS is shown in fig. 3.5. The Muon Spectrometer is interspersed with superconducting air-core toroid magnets. These cause a deflection of the muon trajectories dependent on their

[3] This is the transverse momentum carried away by neutrinos which only weakly interact with the detector material. It can be determined by the negative vectorial sum of all measured transverse momenta, assuming that the total sum of all involved transverse momenta is zero.

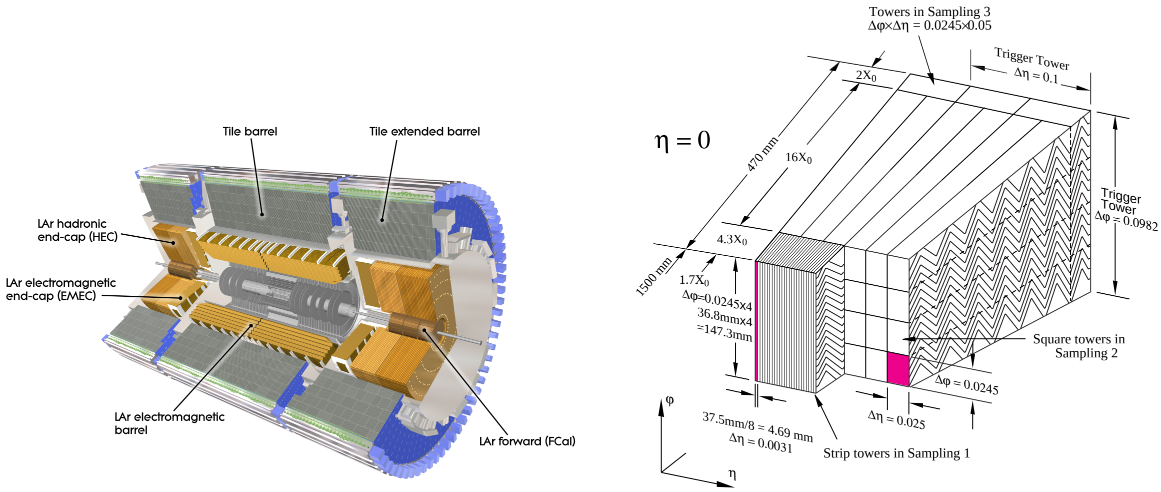

Figure 3.4: Left: Cut-away view of the ATLAS Calorimeter System. Right: Section of the EM Barrel Calorimeter showing the three layers and the granularity of cells/strips [12].

charge and momentum which provides an independent precise momentum measurement that can be combined with the Inner Detector measurement.

The muon traverses on its path three chamber in the MS which arranged in cylindrical shells around the beam axis in the barrel and perpendicular to the beam in the end-caps. In the central region Monitored Drift Tubes (MTDs) provide the measurement, while at large pseudorapidities Cathode Strip Chambers (CSCs), multiwire proportional chambers with strip cathodes of a higher granularity are used. Additional chambers are included in the MS which provide measurements for the trigger system (see next section). In the barrel this is done by Resistive Plate Chambers (RPCs) and by Thin Gap Chambers (TGCs) in the end-caps.

High-energy cosmic muons cross the MS twice, once when they enter the detector in the upper hemisphere and once when they leave it in the lower hemisphere. These two measured muon track segments differ in their momentum typically by 6 GeV which is the average momentum lost during the crossing of the detector volume.

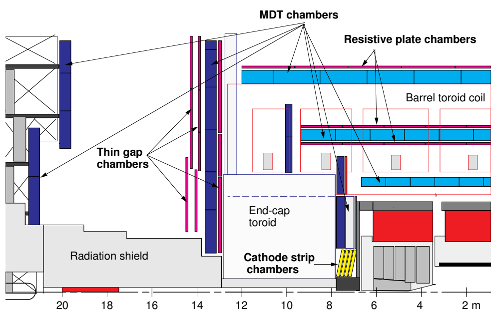

Figure 3.5: Quarter section of the ATLAS Muon Spectrometer [18]

3.3 The ATLAS trigger system

Due to the large bunch crossing rate planned for the LHC, a dedicated trigger system for the detectors is required to reduce the amount of input data recorded to disk and at the same time select the events potentially containing interesting events of new physics with very small cross sections compared to the total proton-proton interaction cross section. In ATLAS this is realized through a three level trigger system which includes the level-1 trigger (L1) based on electronics and providing regions of interest (RoIs) where possibly interesting events are detected, and the software-based high-level trigger (HLT) consisting of level (L2) and event filter (EF). Each level refines the information of the previous level and possibly applies additional or tighter cuts to the events. The event selection criteria are defined in a so called trigger menu. It consists of a set of trigger items for each level with energy and momentum thresholds and additional isolation requirements for different particles and can therefore be adapted to individual requests. The trigger system manages to reduce the initial collision event rate of 40 MHz to 200 Hz storable data [19]. A sketch of the ATLAS trigger system can be seen in fig. 3.6.

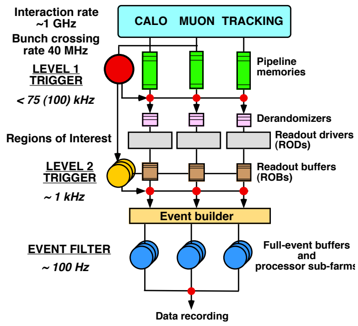

Figure 3.6: The ATLAS trigger system [20]

The L1 trigger needs to make fast decisions in a time less than 2.5 μs and therefore uses simple algorithms applied to reduced granularity information from Calorimeters and the TGC and RCP stations of the muon system. The information of the Calorimeters is used to search for electron/photon clusters, hadronically decaying τ and jet candidates. The energy of the particles is gained from different sets of trigger towers which stretch longitudinally over of the Calorimeters with a granularity of 0.1×0.1 in $\Delta\eta \times \Delta\phi$ and in which the energy depositions in the cells are summed. Different combinations of tower sets and isolation criteria are used to identify the individual particles [20]. A central trigger processor (CTP) combines the information from Calorimeter and muon triggers and makes the final decision based on the trigger menu on whether the event is kept or deleted. In the former case the trigger acceptance signal is transferred to the HLT together with the RoI information. It contains the geometrical η and ϕ position of the detected particles and the energy or momentum value associated to them [12].

The HLT trigger uses the RoIs from L1 as seeds to investigate the events further and make more sophisticated decisions. It already involves full detector granularity, but as it only evaluates detector information locally in the RoIs and applies sequentially processed algorithms, it can still be executed quite fast and at the same time with a high efficiency. The different detected features of the particle are reconstructed step by step and after each step the event can be discarded if the trigger menu cuts are not passed. The L2 trigger implies still simplified algorithms while the subsequent Event Filter (EF) applies a better calibration and the full reconstruction software and thus reaches the highest background rejection. If an event is finally accepted after the three trigger steps, it is passed to the final data storage.

For cosmic events which have a much smaller input data rate the trigger menu is mainly used to test its performance and to fill events in different streams, e.g. to investigate all events which feature an ID track. A special Start-Up trigger menu has therefore been applied especially adjusted to these events [21], [22].

4 Reconstruction of particles from cosmic ray data in the ATLAS detector

Different algorithms are applied in data to reconstruct tracks and Calorimeter clusters and finally the particles of different types.

To handle the different kinds of data recorded with the ATLAS detector - testbeam, collision or cosmic ray events - and also simulated data, a common software framework is used for ATLAS which is called ATHENA. It provides the access to data, the correct execution of the different algorithms and the conversion of the results to histograms or ntuples [23].

The reconstruction chain of real data is executed in the following steps [24]: First, the raw data from the different subdetectors is read and converted to digits. Then, various algorithms are implemented in order to reconstruct the events, for example track fitting or energy measurements and corrections in the different subdetector systems. This information is finally combined to receive the fully reconstructed particle hypothesis. During the reconstruction different databases provide information on the geometry and material of ATLAS and allocate alignment constants to correct the position of sensors and calibration constants to account for dead or noisy channels. The detailed output of the algorithms is stored as *ESD* (Event Summary Data). For cosmic events a special data format of *Commissioning DPDs* (Derived Physics Datasets) has been used. These contain the full ESD information, but have been filtered, 'skimmed', and divided in different streams, so that the most interesting 20% of all events can be investigated in more detail.

The topology of cosmic muon events in ATLAS is significantly different from collision events. They arrive at random times and do not originate from the center of the detector. In contrast, they cross all subdetectors in the upper and lower hemisphere from top to bottom. Their trajectories are distributed over the full detector volume. In order to handle the reconstruction of cosmic muons with the standard algorithms which have been developed for collision data, several modifications had to be implemented.

To account for the arbitrary distance of cosmic events to the detector origin, track reconstruction algorithms for the ID and MS have to abandon the requirement of a vertex at the detector center [25]. The standard algorithms assume the events to arrive synchronously with the LHC readout clock which normally indicates a bunch crossing of the proton beams. All detection times refer to this signal, e.g. drift times in the TRT. To contain the resolution of the subdetector systems, the offset of the muon arrival time with respect to the bunch clock is measured first from the signal of the MS trigger channels [26]. Then, all drift times are corrected for this offset and the right coefficients for the energy reconstruction in the Calorimeters are selected [24] (see sec. 4.3.1).

The reconstruction algorithms which are implemented to find muons and electrons in ATLAS will be presented in the following, focussing on the differences which occur due to the special topology of cosmic events. In addition, the standard cut selection implemented in ATLAS to identify electrons will be explained in detail. Finally, the cosmic data sample which is used for the analysis of cosmic events in this thesis will briefly be explained.

4.1 Track reconstruction

Muon and electrons as charged particles leave track hits in the different ID subsystems and the Muon Spectrometer, respectively. These hits are combined by a χ^2 fit to a track which provides a momentum measurement for the particle. Each track candidate is described by five parameters which are obtained from the fit [23]:

- ϕ_0 the angle of the track direction in the x-y plane at the perigee[4]
- θ_0 the angle at the perigee with respect to the z-axis
- z_0 the longitudinal impact parameter, the distance of the perigee from the origin in z direction
- d_0 the transverse impact parameter, the distance from the origin in the transverse plane[5]
- q/p the particle's charge divided by its absolute momentum value which is a measure for the curvature of the trajectory inside the magnetic field.

A sketch of these parameters can be seen in fig. 4.1.

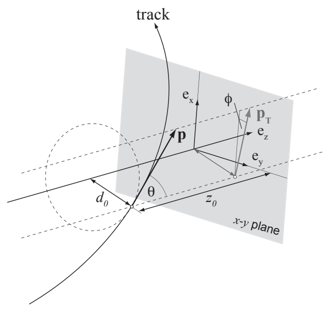

Figure 4.1: The five parameters of a track at its perigee [27].

To adjust the track reconstruction algorithms to the special topology of cosmic events which cross the detector with arbitrary distances to the primary vertex, a special software called *CTB (Cosmics + Test Beam) tracking* has been developed [28]. It allows track finding algorithms to start anywhere in the ID or MS respectively without the constraint of a primary vertex.

The cosmic track reconstruction in the Inner Detector evolves in the following steps [28], [29]: First, the Pixel and SCT clusters and the TRT straws gained from the ATLAS raw data are converted to positions in space and drift radii respectively by using detector geometry information and calibration constants. These are then considered as track hits. Next, pattern recognition algorithms are implemented in order to build the track candidates from the track hits. The track hits are grouped together and the right combination is obtained by a fit which yield a first rough estimation of the track parameters. These algorithms can either start in the silicon detectors or the TRT. In order to reduce the number of fake tracks, the candidates have to satisfy in addition several quality criteria. For example, the number of hits needs to be consistent with the number of detector modules. The subsequent dedicated track fitting algorithm uses the χ^2 method to determine the best track parameters. The quadratic sum of all residuals over the error of the measurement is minimized assuming a Gaussian distribution for these. Residuals denote the distance of the measured hit in each module and the fitted track position extrapolated to this module[6].

To incorporate material effects inside the detector, two deflection angles can be included as additional parameters in the fit which account for the change in direction of the tracks due

[4]The perigee denotes the point of closest approach of the track to the z axis.

[5]The sign of this variable is defined to be positive if the track direction is clockwise with respect to the origin.

[6]The extrapolation is performed by the Runge Kutta extrapolator which numerically propagates the particle trajectories inside a magnetic field in which they follow a helicital path [27].

to multiple scattering [28]. For electron tracks a special bremsstrahlung correction has to be included as the probability that they lose energy in the ID through radiation is very high. Therefore, an additional term is added to the track fitting function which applies a weight to each hit residual dependent on the probability that bremsstrahlung has been emitted in the material in front of the respective module.

A track in cosmic data found by this algorithm stretches over both hemispheres of the ID and is by convention pointing downwards, thus the ϕ direction at every track space point is negative.

4.2 Muon reconstruction

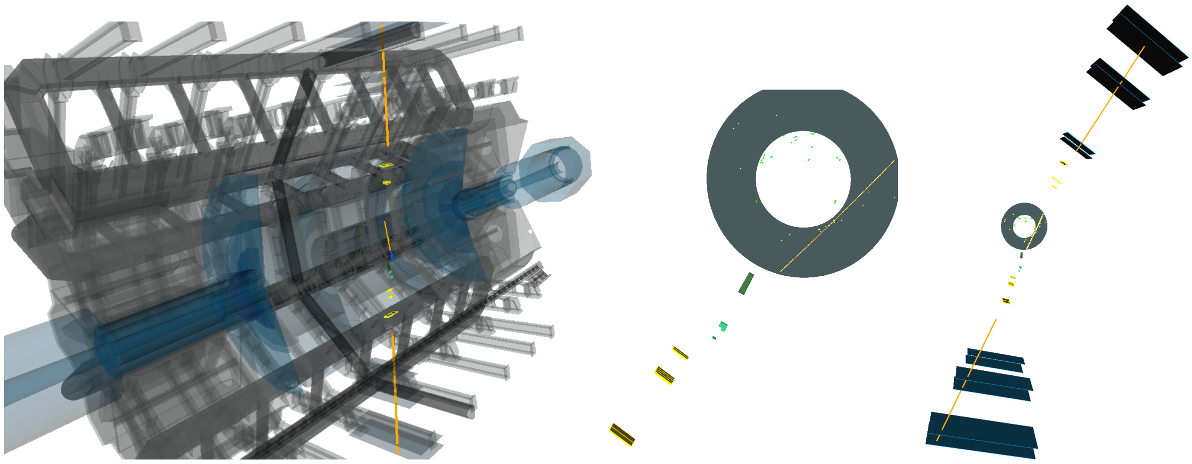

Figure 4.2: Typical cosmic muon events crossing the ATLAS detector which emit bremsstrahlung in the lower hemisphere of the EM. Left: Cosmic muon embedded in the detector system. Middle: Zoomed view of cosmic muon event. Right: Full view of the same event. The full view shows the splitting of the event into one incoming ($\phi > 0$) and one outgoing ($\phi < 0$) muon candidate in the two hemispheres of the MS as orange tracks which cross three muon chambers each (blue rect.). The ID muon track (orange) can be seen in the center inside the projection of the TRT barrel (grey) including the track hits. The yellow and light green squares show the muon's energy deposition in the HCal and EM. Also the reconstructed EM cluster is depicted at $\phi < 0$ (dark green).

In general, three algorithms are to be distinguished for a reconstruction of muons [31], [32]: First to be mentioned is the standalone 'Muonboy' algorithm which is most efficient for muon momenta above 100 GeV. It includes only the tracking information in the Muon Spectrometer. The pattern recognition and track fitting algorithms find hits in different muon stations which are combined to the muon candidate. Finally, the MS track is extrapolated to the beam line in the detector center.

The combined 'Staco' muon reconstruction pairs the standalone track in the MS with an ID track which lies nearby the extrapolated MS track. The combination of both track parameter measurements compensates the lower resolution in the MS due to energy losses and scattering in the Calorimetry at muon momenta below 100 GeV.

The third algorithm, developed for low momentum muons, is the tagging algorithm 'MuTag'. It makes use of muon track segments which cannot be combined to tracks by Muonboy or Staco in the MS. An ID track is extrapolated to the MS where nearby muon track segments are searched for and associated to it.

Muons lose typically around 3 GeV on a path between Inner Detector and Muon Spectrometer due to their interaction with the in-between material via radiation, ionization or multiple scattering. This has to be taken into account for the muon reconstruction when extrapolating tracks to the other region. Based on exact simulations of the material, corrections to the muon momentum and direction are calculated and applied. The muon candidates found by the three different algorithms are stored in the STACOMuonCollection which is also used in this analysis.

Due to the different topology of cosmic events in contrast to collision data, several peculiarities occur for the muon reconstruction. A cosmic muon crossing the full ATLAS detector from above leaves track hits and energy depositions in both detector hemispheres. Therefore, for each cosmic muon two muon candidates are reconstructed in the MS: One in the top hemisphere ($\phi > 0$) which is the incoming muon, and one in the bottom hemisphere ($\phi < 0$) which is the outgoing muon. In the cosmic data reprocessing of December 2008 (see sec. 4.5), the upper muon is assumed to point from inside out during reconstruction, like it would be the case for collision events originating from the center of the detector. Thus, its charge and its direction have to be inverted ($\phi \to \phi - \pi$, $\eta \to -\eta$) to correspond to the true cosmic muon direction and to be able to compare the incoming with the outgoing candidate. As a consequence of this, the MS muon candidate and the ID track cannot be matched to each other as they are pointing in opposite directions. Thus, the combined and tagged algorithms fail, and most muon candidates in cosmic data are found by the standalone algorithm.

A typical cosmic muon signature in real data consists therefore of two separate standalone candidates in both MS hemispheres ($\phi > 0$ and $\phi < 0$), energy depositions in both Calorimeter hemispheres and a track in the ID pointing downwards. The two muon candidates have an opposite charge. The event displays of typical cosmic muons in ATLAS can be seen in fig. 4.2.

In the cosmic Monte Carlo, in contrast, which was adjusted to improved cosmic data reprocessings (see sec. 5.1), the track direction and curvature inversion was already done during the reconstruction. Thus, the two muon candidates are stored with the same charge and both pointing downwards.

The angular distribution of cosmic muon candidates reconstructed in the MS in the cosmic data sample is illustrated in fig. 4.3. The azimuthal angular distribution of the muon candidates confirms that most tracks cross the detector vertically and leave one reconstructed candidate in the upper hemisphere of the MS ($\phi > 0$) and one in the lower hemisphere ($\phi < 0$). The asymmetry of both angular distributions can be ascribed to the ATLAS access shafts which influence the cosmic ray flux in the x-z plane (see sec. 2).

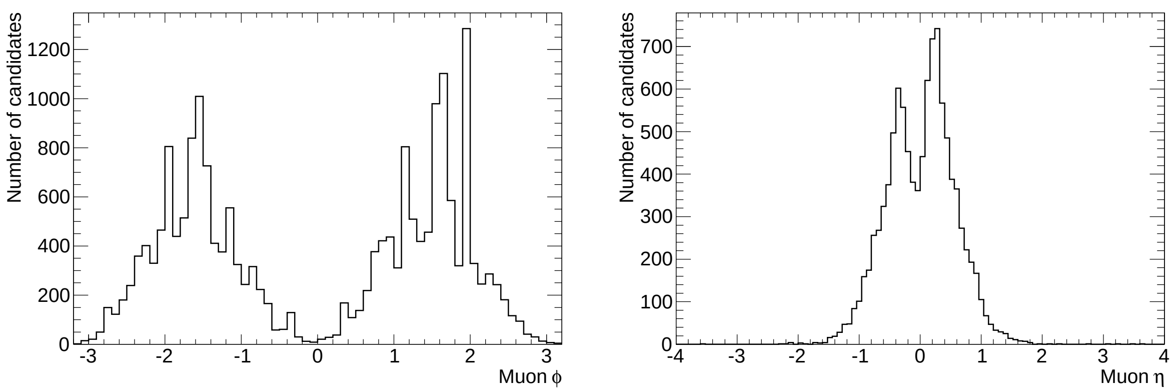

Figure 4.3: Left: Distribution of the ϕ direction of the muon candidates in the MS shown for the incoming and outgoing candidates of the investigated cosmic data sample. Right: Distribution of the η direction of all incoming muon candidates in the investigated cosmic data sample.

4.3 Electron reconstruction

To reconstruct electron candidates[7] in the ATLAS detector information from the Inner Detector and the Electromagnetic Calorimeter is used. Electrons leave a track in the ID and an electromagnetic shower in the Calorimeter, which is reconstructed as a *cluster* (see next section). Two algorithms are applied to find electrons in ATLAS [33], [18].

The default reconstruction algorithm is the cluster-based algorithm called *egamma*, it starts from the shower in the Calorimeter. A cluster is searched for by the *sliding-window* algorithm (see next section) first. If a cluster with $E_T > 3$ GeV is found, an ID track in the neighbouring area is searched for and matched to it. The track is required to have a similar momentum value compared to the cluster energy (E/p <10) and a rough position matching $\Delta\eta \times \Delta\phi < 0.05 \times 0.1$ between the cluster position and the track extrapolated to the Calorimeter[8]. In cosmic ray data, many tracks only cross the TRT which provides no accurate η measurement. In this case only a $\Delta\phi$ position matching is done.

The second, track-based, algorithm, called *softe*, uses an ID track as seed. It has especially been developed for low-energy electrons. Several quality criteria are applied to the track: The transverse momentum must be larger than 2 GeV, it is required to have at least 7 silicon hits including 2 Pixel hits, a transverse impact parameter < 1 mm and a fraction of transition radiation hits in the TRT > 0.05 (see sec. 3.2). If such a track is found, it is extrapolated to the second layer of the EM and a cluster is built around this position with topological clustering (see next section).

The electrons found by these two algorithms are stored in a container called *ElectronAOD-Collection*. If an electron is found by both algorithms, it is stored as the same object. For cosmic data, the *softe* algorithm is in most cases not successful, as the electron tracks cannot fulfil the track quality cuts due to the fact that they do not originate from the center of the detector. So most of the electron candidates are found with the *egamma* algorithm.

If electron tracks are found to originate from a secondary vertex, this event is usually regarded as photon conversion and stored as a photon candidate. For cosmic data, a vertex finding algorithm was not implemented, thus also candidates resulting from photon conversion are stored as electron candidates.

4.3.1 Building and calibration of Calorimeter clusters

A cluster is a group of neighbouring cells in longitudinal and lateral direction in the Calorimeters in which a traversing particle deposited energy in form of a shower. It contains the information on the total sum of energy deposited in these cells. The clusters of electrons and photons are reconstructed exclusively in the EM.

To build the clusters for these particles, two different algorithms are used [12], [34]. The one implemented in the standard electron/photon reconstruction (see previous section) is the *Sliding Window Algorithm* which consists of three steps. First, a grid of towers is built in the η - ϕ plane of the EM which all have the same size in $\Delta\eta \times \Delta\phi$ (0.025×0.025). The energy depositions of all cells within one tower in all EM layers are summed. Next, a quadratic window of $5{\times}5$ towers is moved across the whole Calorimeter area in steps of $\Delta\eta$ and $\Delta\phi$. If the sum of the transverse energy within this window passes the threshold $E_T^{\mathrm{thres}} = 3$ GeV, a precluster is

[7]In this thesis the notation 'electron' will always refer to candidates of both charges as a common term, so it always includes electrons and positrons, unless the positrons are explicitly mentioned.

[8]A looser matching is required in ϕ direction as the electron track is curved in this plane due to the solenoid field.

Type	Window size in $\Delta\eta \times \Delta\phi$ (units of 0.025)
Precluster	5×5
Electron	3×7
Photon	3×5

Table 4.1: Window sizes for different clusterization steps and particle types in the barrel of the EM

found. The size of the window and the threshold have been optimized to find clusters efficiently and to minimize the amount of fake clusters produced by noise[9]. The η and ϕ position of the precluster is determined as the energy-weighted mean of the barycenters of the included cells. If two preclusters overlap within the core 2×2 tower window, only the one with the largest energy is kept.

As a last step, the final particle-specific EM cluster for electrons and photons is built around the precluster[10]. The size is chosen to maximize on the one hand the contained energy for a good resolution and to minimize on the other hand contributions from noisy cells at the margin of the cluster. For electrons, the cluster has a size of 3 × 7 cells in $\Delta\eta \times \Delta\phi$ (segmentation 0.025). It has a large extension in the ϕ direction since electron tracks are curved by the magnetic field and their shower thus covers a larger area and may include additionally emitted bremsstrahlung photons from the ID. The photon in contrast is not deflected in the ID, therefore its cluster is narrower. The different cluster sizes are listed in tab. 4.1.

The second cluster-finding algorithm, *topological clustering*, is only used rarely for electron/photon reconstruction. A variable number of cells with a significant energy deposition is grouped together to form a cluster. The algorithm starts with the search for cells which overcome a high signal-to-noise threshold in the whole EM. Subsequently, the neighbouring cells around this seed are added to the cluster if their energy significance is larger than a lower signal-to-noise threshold.

Sliding-window clusters are preferably used for electrons and photons, as their rectangular shape makes them on the one hand compatible with the Calorimeter towers of the trigger (compare sec. 3.3). On the other hand, they provide a uniform cluster shape for all candidates. This facilitates a comparison of the individual lateral and longitudinal shower shapes which is essential for electron and photon identification (see next section).

If a cluster has been found, a calibration must be implemented to provide accurate energy and position measurements in the EM with a high resolution. The reconstructed position, as the energy-weighted barycenter of the cluster in each layer, is biased due to the finite extension of the single cells and has to be corrected for the exact impact position of the particle inside the cell. Also, other modulations due to geometry have to be accounted for. Subsequently the energy measurement of the cluster has to be corrected for energy losses outside the Calorimeter. These losses can occur in the Inner Detector and the solenoid due to bremsstrahlung of electrons and behind the Calorimeter. The variables describing the different energy losses are correlated with the measurable energies deposited inside the cluster layers and depend on the η position. The exact coherence can be gained by special simulations (*calibration hits*) where energy deposits in active and in passive or dead materials are recorded [35]. The corrected energy is then a sum of the energy lost in front of the Calorimeters which can by measured by the fraction of energy deposited in the presampler, the energy deposited inside and outside the cluster in the EM and

[9]Noise in the Calorimeter cells is produced by the readout electronics. In proton collision events ‘Pile up’ effects from underlying events additionally contribute to the noise. For cosmic events with a much smaller event rate this effect is negligible.

[10]This step is therefore performed after a particle hypothesis during the *egamma* reconstruction has been made.

the energy deposited behind it [18].

One important aspect to mention for cosmic events is their lack of *projectivity*. This refers to the difference of the track direction and the cluster position. More exactly, it describes the angular difference between the particle's flight direction at the impact point in the Calorimeter and the vector pointing from the detector origin to this impact point. This is illustrated in fig. 4.4. For tracks originating from the detector center, this angle is approximately zero and they are referred to as *projective* particles. For cosmic tracks with an arbitrary origin this angle is often different from zero, these tracks are therefore *non-projective*. In this case, also the direction of the shower development is different from the orientation of the Calorimeter cells which makes them fail the cluster reconstruction algorithms more easily.

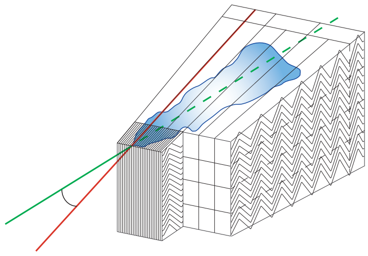

Figure 4.4: Illustration of a non-projective particle. The angle between the particle's track direction at the Calorimeter surface (green) and the vector from the detector origin to this impact point (red) is sketched.

4.4 Electron identification

The reconstruction of electrons is not immune against background processes in which electron-similar objects are produced. Thus, often a high fraction of fake electrons is contained among the reconstructed candidates. The main source of fake electrons in cosmic data is bremsstrahlung of muons in which the EM cluster resulting from the photon shower is matched to the muon ID track. In collision data, further sources like pions or jets contribute, in addition. In order to separate the true electrons from background, a set of numerous identification cuts is commonly applied in the analysis of ATLAS data, called *IsEM*. This cut selection makes use of characteristic properties of electrons such as the lateral and longitudinal shower extensions in the Electromagnetic Calorimeter and different track quality and matching criteria. The different discriminating variables are explained in the following.

Information from the Calorimeters

Due to the fine granularity of the second and first EM layer in which electrons deposit more than 40% of their energy each, several shower characteristics are evaluated and cut on in these layers. The cuts account for the fact that an electron shower starts early in the EM and has a small lateral extension. Especially the first layer has a fine granularity in η and thus provides detailed information of the shower structure. In addition, the energy deposition in the Hadronic Calorimeter is analysed and used as a discriminative variable. Electrons usually deposit only a negligible fraction of their energy in the HCal as their shower is usually completely contained in the EM. In contrast, muons deposit only a small fraction of their energy in the EM through bremsstrahlung and can leave a much larger energy fraction also in the HCal.

It should be noted that the lateral shower extension is exclusively evaluated in the η direction, because in the ϕ direction the shower is enlarged due to the curvature of the electron track and bremsstrahlung emitted by electrons. The cut variables in detail are [18], [33]:

- **Hadronic leakage** This is the fraction of the total transverse cluster energy of the electron deposited in the first layer of the HCal. Electrons leave usually less than 2% of their energy here.
- **Second layer of Electromagnetic Calorimeter**
  - **Reta** A measure for the lateral shower extension in the η direction. The variable R_η, is determined as the energy sum deposited in a window of 3×7 cells in $\Delta\eta \times \Delta\phi$ over the energy deposition in a window of 7×7 cells (For the exact cell extensions see sec. 3.2). As electrons should have a small lateral shower extension, this ratio should be close to one.
  - **Weta2** The lateral shower width in a window of 3×5 cells is calculated from the sum of the individual η cell positions with respect to the impact point of the electron, weighted by the deposited energy in the respective cell:

$$\omega_{\eta^2} = \sqrt{\left(\frac{\sum E_{\text{cell}} \cdot \eta_{\text{cell}}^2}{\sum E_{\text{cell}}}\right) - \left(\frac{\sum E_{\text{cell}} \cdot \eta_{\text{cell}}}{\sum E_{\text{cell}}}\right)^2} \tag{4.1}$$

- **First layer of Electromagnetic Calorimeter**
  - **F1** Fraction of energy deposited in first EM layer which is mostly larger than 40% for electrons.
  - **Rmax2** A variable which helps to detect substructures and multiple maxima in the shower which occur in the case of pion decays and also multiple muon bremsstrahlung photons. $R_{\text{max2}} = E_{\text{max2}}\,[\text{GeV}]\,/(1 + 9 \cdot 10^{-3} E_T\,[\text{GeV}])$, E_{max2} denotes the energy of the strip with the second largest energy deposit and E_T is the total transverse cluster energy. For electrons which usually feature only one shower maximum, this value should be relatively small.
  - **DeltaE2** This variable also describes the substructure of the shower. The difference between the energy of the strip with the second largest energy deposit - in a window of $\Delta\eta \times \Delta\phi$ =0.125 × 0.2 around the strip with the maximum energy deposit - and the strip with the minimum energy in between the two maxima is determined $\Delta E_2 = E_{\text{max2}} - E_{\text{min}}$. This value should also be rather small for electrons.
  - **Wtot** The total shower width is calculated in a window of $\Delta\eta \times \Delta\phi = 0.0625 \times\ 0.2$, corresponding to 40 strips of the first layer. It is defined as the energy weighted sum of the strips around the strip with the maximal energy deposit:

$$\omega_{\text{tot}} = \sqrt{\frac{\sum E_i \cdot (i - i_{\text{max}})^2}{\sum E_i}} \tag{4.2}$$

    E_i is the deposited energy in the strip with the number i, i_{max} is the number of the strip with the largest energy. For electrons the total shower width should be small.
  - **Fside** This variable refers to the shower shape in the shower core region,

$$F_{\text{side}} = \frac{E(\pm 3) - E(\pm 1)}{E(\pm 1)} \tag{4.3}$$

    where $E(\pm n)$ is the energy deposited in $\pm n$ strips around the highest energy strip.

– **Weta1** The core shower width in η direction is defined as the sum over the energy weighted strip numbers of the three strips around the strip with the maximum energy:

$$\omega_1 = \sqrt{\frac{\sum E_i \cdot (i - i_{\text{max}})^2}{\sum E_i}} \tag{4.4}$$

Inner Detector information and combination of cluster and track

The precise track information from the Inner Detector is used to discriminate between signal and background as well. Especially, an accurate comparison of position and energy associated to cluster and track can reduce the background to a large extent since muon bremsstrahlung events often feature only a weak matching of these variables. The discriminating variables are listed here:

- **Track quality cuts**
  - **Silicon hits** At least 9 precision hits (Pixel and SCT).
  - **Pixel hits** At least 2 hits in the pixel layers.
  - **Transverse impact parameter** A small $|d_0| < 0.1$ cm is required.
  - **TRT hits** At least about 20 TRT hits, depending on the η direction of the particle.
- **Track match between track and cluster** An exact spatial matching in η and ϕ is required for electron track and cluster.
  - **Delta Eta** $\Delta\eta = |\eta_{\text{clus,Lay1}} - \eta_{\text{ID}}|$, the difference in η between the first layer cluster position (which has the finest segmentation) and the track extrapolated to the first EM layer
  - **Delta Phi** $\Delta\phi = |\phi_{\text{clus,Lay2}} - \phi_{\text{ID}}|$, the difference in the ϕ position of the cluster in the second layer (finest ϕ granularity) and the track extrapolated to this layer
- **E/p Energy over momentum matching** The ratio of the energy measured in EM and momentum measured from track curvature in the ID, this should be around one for electrons, see detailed description below.
- **HT-TRT ratio** The ratio of high to low-threshold hits in the TRT. The high threshold hits are caused by transition radiation which is emitted by the traversing particle, and can be used to distinguish between the different kinds of particle tracks. See detailed description below.

The two most important variables for discriminating between fake candidates produced by muon bremsstrahlung and real electrons especially in cosmic data are E/p and the HT-TRT ratio.

E/p is the ratio of energy measured from the Calorimeter cluster and the momentum which is determined from the curvature of the track due to the magnetic field in the ID[11]. For electrons this variable should have a value around one since they deposit nearly their total energy in the EM due to their high bremsstrahlung-emission probability in matter. In addition, their mass is negligible at the investigated energy scale, thus momentum and energy are equivalent. For muons in contrast, the ratio of energy and momentum is expected to have a very small value

[11] The momentum can be determined as $p/\,[\text{GeV/c}] = 0.3 \cdot B \cdot \rho/\,[\text{Tm}]$, with track curvature radius ρ.

since the probability of losing energy through bremsstrahlung is much smaller for muons with energies below several hundred GeV. As a consequence, they deposit only a small fraction of their total energy in the EM through bremsstrahlung and the reconstructed cluster energy has a much smaller value than the momentum measured from the muon ID track. The E/p distribution is compared for all reconstructed electrons matching a truth electron and the candidates without a truth match which are thus background events in fig. 4.6 (left, see sec. 5.1 and 8). The described difference in the distribution is clearly visible.

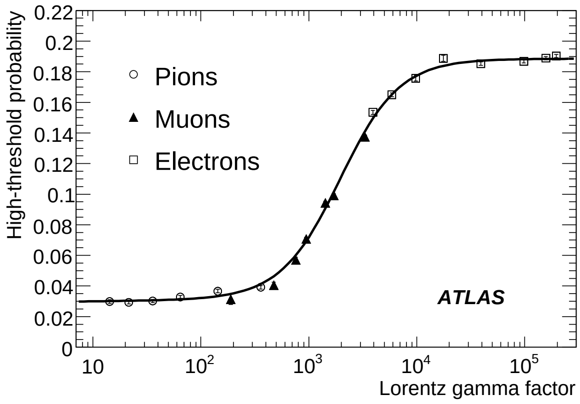

Figure 4.5: Average probability for a high threshold hit in the TRT barrel produced by transition radiation of electrons, pions and muons dependent on the particles' Lorentz γ factor measured in the combined test-beam [18].

The high-threshold hits in the TRT are produced by transition radiation of particles at the interface of media with different dielectric constants (see explanation in sec. 3.2). The **ratio of high to low-threshold TRT hits (HT-TRT ratio)** is the fraction of these produced transition radiation hits with respect to the total number of ordinary hits in the TRT produced likewise by the ionizing particles. It is therefore a measure for the particle-specific amount of emitted transition radiation. The probability of transition radiation depends linearly on the particle's Lorentz factor $\gamma = E/m$ and the detection capability of ATLAS starts rising for $\gamma \approx 1000$. The dependency of the high-threshold hit probability on the Lorentz factor is shown in fig. 4.5. Electrons produce a high rate of detectable transition radiation already above an energy of 500 MeV, while muons need to have an energy larger than 100 GeV to emit a significant fraction of TR photons. Thus, a high HT-TRT ratio is expected for electrons in the examined energy range, while for the background of muon bremsstrahlung the ratio should be lower on average, at least at not too high energies. The distribution is compared in the cosmic Monte Carlo sample for electron candidates with and without a truth-electron match (fig. 4.6, right). Also in this case the difference between signal and background events is obvious. The explained variables therefore provide important tools to separate the real electrons from the background of muon bremsstrahlung.

The electron identification cuts are often grouped into three cut sets: loose, medium and tight. The loose set contains the cuts on hadronic leakage and the shower shape in the second EM layer, to reach a first moderate rejection of background. The cut set for a medium electron contains, in addition, the track quality variables - except for the number of TRT hits - and the information of the first EM layer which provides a finer η resolution and increases the rejection of background. The tight selection additionally includes the track matching criteria, the E/p ratio and the TRT information with the HT-TRT cut. It provides the highest background rejection

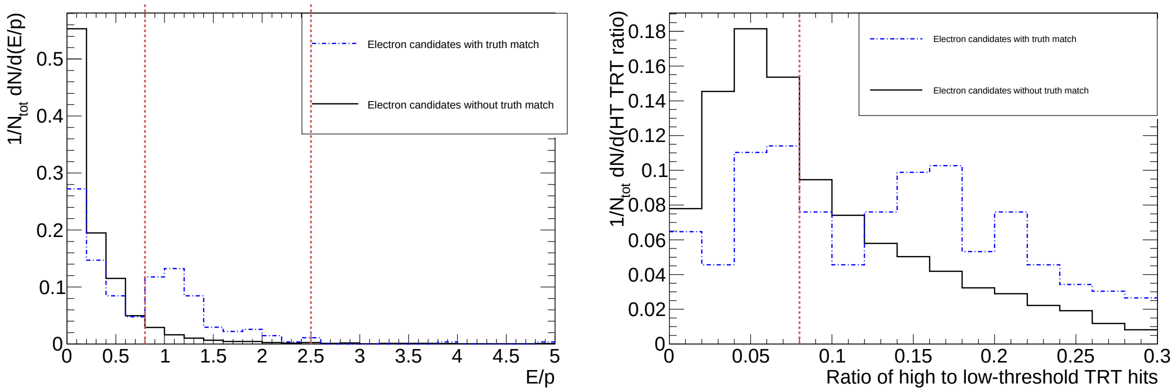

Figure 4.6: Comparison of E/p distribution (left) and the ratio of high to low-threshold hits in the TRT (right) for electron candidates matching a truth electron (blue dashed line) and candidates without a matching truth electron (black solid line) for events of the cosmic Monte Carlo sample. The red lines indicate typical cuts on this variable for events with a small E_T and η value.

and therefore the highest purity of an electron sample. The cuts have been developed and optimized for collision data. For electrons in cosmic data with a different topology not all cuts can be applied when reasonable statistics should be maintained. The modified cut sets which are applied to cosmic data, as well as the individual cut thresholds, are explained in sec. 7.1.2.

4.5 Cosmic data sample used for analysis

The cosmic data events which are studied in this thesis were recorded in autumn 2008 with the ATLAS detector. A total of 216 million events were recorded during the cosmic runs in September and October 2008 [24]. A first reprocessing of the data, the rerunning of reconstruction algorithms with improved alignment and calibration constants, was performed in December 2008[12]. Only runs with sufficiently large statistics (>500k events) were included in the reprocessing in which no subdetector was flagged to be in bad condition. For the analysis presented in this thesis, the cosmic data of this reprocessing is used. Only events are included which have been recorded during the time when toroid and solenoid have been turned on at nominal current to ensure a correct momentum measurement in the Inner Detector and the Muon Spectrometer.

Furthermore, only the trigger stream *IDCosmic* is investigated. In this stream the events are required to be found by any level-1 trigger and to have at least one Inner Detector track reconstructed by the level-2 trigger track algorithms. The events in this data sample are distributed over the whole volume of the ID, they do not necessarily cross the center of the detector or even the Pixel or SCT subsystems. This is the most appropriate trigger stream for an analysis of electrons with sufficiently large statistics (see sec. 4.3). All available larger runs of this type are included for the analysis [38], amounting in total to 3539264 events.

To obtain a handy data set for the analysis, of the 3539264 *IDCosmic* events only the ones contained in the *DPD_EGAMTAUCOMM* stream are used for a closer investigation. This stream contains all events which have at least one offline reconstructed τ, photon or electron candidate. In order to reduce the size of the studied data set even more, these events have additionally been skimmed to remove the large fraction of events which contain only τ candidates and which are of no interest for the analysis. Finally 31862 events remain for the study, of which 10611 contain at least one electron candidate.

[12]The reprocessing was done with ATHENA release 14.5.0.5.

5 Generation and simulation of cosmic events in ATLAS

For the production of Monte Carlo events in ATLAS, a simulation chain of several steps is implemented [24]: First, the events are generated, in this case the cosmic muons, and their four momenta are calculated. The single cosmic muons are simulated at the ground level with an energy and angular distribution based on the expected cosmic ray muon flux at the surface (compare sec. 2). Their production vertex is required to be within a 600m $\times$ 600m square above the ATLAS detector. They are filtered have an incident angle smaller than 70 degrees and an energy above 10 GeV at the surface [39]. Only events which point to the volume of the ATLAS envelope are kept [26].

These cosmic muons have to be propagated through the rock above the detector which is done by the GEANT4 toolkit [23]. Therefore, the geometrical description of the ATLAS cavern, the ca. 80 m rock overburden and the two large access shafts is included to simulate the muon trajectory which is influenced by energy loss processes like bremsstrahlung, ionization or decays. The angular distribution of the muons reaching the ATLAS pit is thus influenced by the shafts which especially allow low-energy muons to enter the detector without being disturbed by the interaction with the rocks. Muons which do not reach the ATLAS detector are discarded. For the remaining muons the interaction with the ATLAS detector material on their way through all subsystems is simulated. Here, it is accounted for the influence of the magnetic fields, radiative and ionization energy loss processes, decays in flight and subsequent reactions in the material like photon conversions.

As a next step the detector response including electronics is simulated [40]. For example, for the TRT the charge carriers produced by an ionizing particle are simulated, their drift to the anode wire and the following response of the electronics. This step is called digitization. This output has the same form as the real data digits and the simulated data can now be passed through the reconstruction algorithms in the same way as real data, and it is also stored as ESD or skimmed down to DPDs. A simulation of the trigger is not implemented in the Monte Carlo samples used for this analysis.

5.1 Cosmic Monte Carlo sample used for analysis

For a comparison of the obtained results from the real cosmic data recorded by ATLAS, a sample of simulated cosmic events is used with a similar detector geometry also containing the full event information in ESD format. The reconstruction algorithms applied to the simulated data were identical with the ones used for cosmic data in an updated reprocessing of spring 2009[13]. For this thesis, only events of a simulation with solenoid and toroid field switched on are studied in which cosmic muons cross the Inner Detector volume since this complies best with the real data sample containing L2 trigger track candidates in the ID. This Monte Carlo sample consists in total of 9780293 cosmic events. It has been skimmed down to Commissioning DPDs in the same way as the data sample: Only events which contain at least one electron candidate have been kept. This reduces the sample to 9125 events.

[13]For this reprocessing ATHENA release 14.5.2 has been used

6 Theoretical expectation for electron production from cosmic rays in ATLAS

Most cosmic muons which traverse the ATLAS detector are minimum ionizing particles, i.e. they deposit only a small fraction of their energy in the detector through ionization and excitation of atoms. In rarer cases, especially for muons with higher energies, the interaction with the detector material or decay can lead to the emission or production, respectively, of electrons with larger energies in the Inner Detector which can reach the EM and be reconstructed by the standard ATLAS algorithms as electron candidates (see section 4.3).

The more numerous low-energy electrons (<500 MeV) which can be produced during muon interactions are bent too strongly by the magnetic solenoid field, so that they do not reach the Calorimeter and are not detectable as electrons in ATLAS.

High-energy electrons can be produced by three main processes: muon decay in flight, ionization and conversion of a bremsstrahlung photon (see fig. 6.1). In the following sections, they will be described in detail. Also, analytical order-of-magnitude calculations on the probability of the processes to occur will be made. In addition, muon bremsstrahlung as a source of background will be analysed.

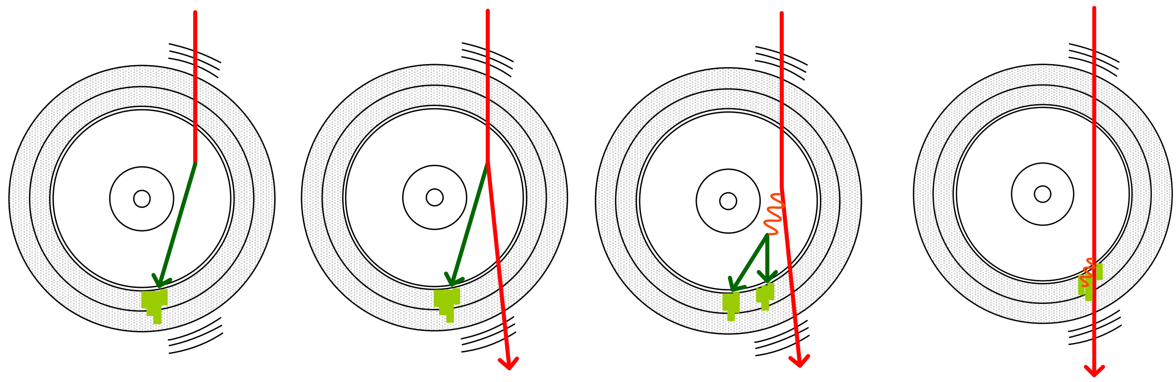

Figure 6.1: Left: A sketch of the signatures of the three possible electron production processes in the ATLAS detector. Shown is the schematic profile of the ATLAS detector, the ID, Calorimeters (shaded) and MS. The muon track is shown in red, the electron track in green, the electron shower in light green and photons are depicted as sinusoidal orange lines. The curvature of the charged particles due to the magnetic fields is not displayed; Electron production processes from left to right: Muon decay in flight, delta electron emission, photon conversion. Right: Background process muon bremsstrahlung (fake electrons).

6.1 Calculation of material properties and average quantities

In order to calculate probabilities for different electron production processes in cosmic data, several overall quantities of the material and the incoming cosmic muons have to be estimated first, which will be inserted in the calculations.

An estimate of the path length has to be made on which cosmic muons can produce or knock off detectable electrons. As explained in sec. 4.3 it is essential for electrons to have an ID track. This means the muon interaction processes have to take place within the ID volume. The effective ID path length of the muons is extracted from the cosmic ray data sample (see description in sec. 4.5).

First the mean total path length of cosmic muon tracks in the ID is estimated. Most of the cosmic tracks only pass the TRT which provides no accurate information on the η direction of the tracks. Thus, only the mean path length in the transverse plane is determined from all tracks (ca. 24000 events). The cosmic tracks are evaluated only at three space points in the ID, for which track parameters are provided (see sec. 4.1). From these, the highest and lowest track point in y direction are determined and extrapolated to the outer volume of the sensitive transverse plane of the TRT barrel (Its radius is 106.6 cm.)[14]. From these positions the transverse path length is calculated for each cosmic track: $d_\perp = \sqrt{(y_t - y_b)^2 + (x_t - x_b)^2}$. The variables y_t, x_t denote the intersection point with the barrel border at the top half extrapolated from the highest track point in y, and y_b, x_b denote the intersection point at the bottom half extrapolated from the lowest track point. The distribution for all 24000 cosmic tracks is shown in fig. 6.2.

The mean of this distribution is $\bar{d}_\perp = 174.5 \pm 41.5$ cm[15].

As a next step, the mean polar angle of the cosmic muon tracks is calculated. This information can only be gained from tracks which have at least one silicon hit (ca. 7800 events). The polar angle distribution, projected on values between 0 and $\pi/2$ is shown in fig. 6.2. The mean value is $|\bar{\theta}| = 1.16 \pm 0.27$rad.

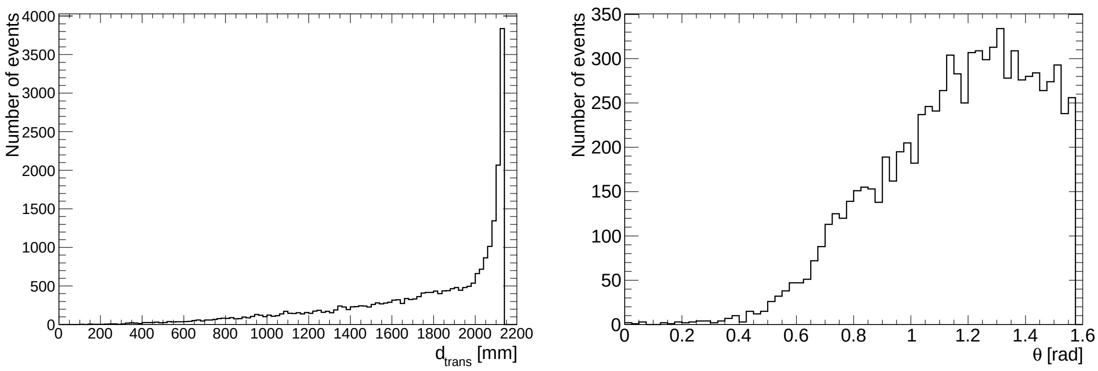

Figure 6.2: Left: Transverse path length distribution calculated for all cosmic muon tracks in the cosmic data sample. Right: Distribution of the polar angle $|\theta|$ for muon tracks in cosmic data with at least one silicon hit

As a simple approximation the total mean path length of cosmic muons in the ID can therefore be calculated as:

$$\bar{d} = \frac{\bar{d}_\perp}{\sin|\bar{\theta}|} \tag{6.1}$$

In addition, it needs to be accounted for the fact that the produced electron has to cross a minimal path in the detector to be reconstructed. A measure for that is obtained from the average number of TRT hits per path length. In cosmic data the average number of TRT hits for all electron candidates is $\bar{N}_{\mathrm{TRT}} \approx 70 \pm 30$. Divided by the mean path length, this yields the approximate number of hits per path length. For the electron identification it is required that

[14]The tracks are approximated as straight lines here, not taking into account the deflection by the magnetic field.

[15]The stated uncertainty is the standard deviation σ of the distribution. The error on the mean is usually calculated as $\frac{\sigma}{\sqrt{N}}$. But to account for the uncertainty which occurs due to the simplified assumption of one single path length for all cosmic tracks, the standard deviation is chosen instead as a conservative estimate of the systematic uncertainty on the mean value in this case. This applies also to all other uncertainties given in this chapter, unless stated otherwise. Statistical uncertainties are here and in the following calculations neglected as they are much smaller than the systematic errors.

an electron has at least $\bar{N}_{\mathrm{TRT}}^{\mathrm{el}} = 20$ TRT hits. The obtained minimal track length of electrons is therefore subtracted from the mean total track length of cosmic muons (eq. 6.1). This yields finally an 'effective' track length for cosmic muons in the ID, on which electrons can be produced:

$$\bar{d}_{\mathrm{corr}} = \bar{d}(1 - \frac{\bar{N}_{\mathrm{TRT}}^{\mathrm{el}}}{\bar{N}_{\mathrm{TRT}}}) \tag{6.2}$$

The results for the total and effective mean path length can be found in table 6.1.

	Calculated values
d [cm]	190.3 ± 50.4
d_{corr} [cm]	135.9 ± 42.9
p_{μ}^{low} [GeV/c]	44.5 ± 24.8
p_{μ}^{high} [GeV/c]	200 ± 150
T_{min}[GeV]	3.27 ± 0.50

Table 6.1: Mean/minimal quantities of incoming muon and produced electron estimated from cosmic data: Total path length, effective path length of muon tracks, mean muon momentum truncated at two different values (see text) and minimal electron energy for reconstruction

For a calculation of the cross section for different electron production processes an estimate for the mean energy/momentum of the incoming muon needs to be obtained which is estimated from the momentum spectrum of cosmic data [16]. The spectrum is shown in fig. 6.3.

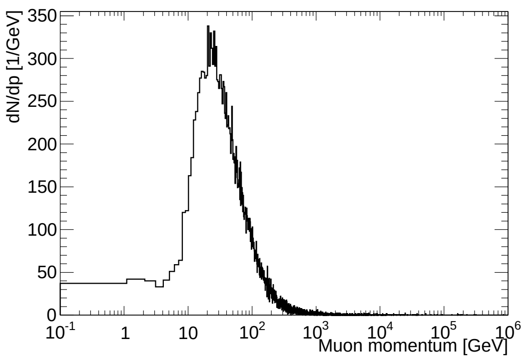

Figure 6.3: Distribution of muon momentum for all muon candidates with $\phi > 0$ in cosmic data.

The spectrum has a large range and several outliers at very high energies. To obtain a reasonable average value, the spectrum needs to be truncated. As will be explained later, the momentum range where muons contribute dominantly to the cross section is different for the particular electron production processes. Therefore, two means truncated at two different values are calculated. The variable $\bar{p}_{\mu}^{\mathrm{low}}$ is the average momentum for $p_{\mu} < 100$ GeV. The variable $\bar{p}_{\mu}^{\mathrm{high}}$ is the truncated mean for $p_{\mu} < 10$ TeV. The results are listed in table 6.1 including the uncertainty which is assumed to be the standard deviation of the corresponding distribution.

Another quantity which needs to be determined is the minimal kinetic energy required for electrons in order to be reconstructed by the standard algorithms. The transverse energy $E_T^{\mathrm{thres}} =$ 3 GeV is the threshold of the *sliding-window* algorithm for an electron cluster reconstruction (see sec. 4.3). This value does not take into account the energy losses of the electron before, after and

[16]Energy and momentum of the muon are equivalent in this high relativistic case.

outside of the Calorimeter reconstruction window. The average minimal total kinetic energy of the electron is then[17]:

$$T_{\min} = \frac{E_T^{\mathrm{thres}}}{\sin|\bar{\theta}|} \tag{6.3}$$

The result is given in table 6.1. The uncertainty on this value is composed of the standard deviation of the mean θ angle in cosmic data (see above) and an estimated relative error of 10% on the threshold transverse energy which accounts for the energy losses outside the Calorimeter.

For a calculation of the number of produced electrons, also the properties of the material crossed by the cosmic muon in the ID need to be known.

The ATLAS ID consists of numerous materials, e.g. xenon gas in the TRT straw tubes, silicon in the precision tracker parts or carbon used for cables. From this mixture of materials with different properties, mean quantities for density ρ, radiation length X_0, nucleus charge Z and the atomic mass A can be obtained dependent on the η position. From [41] an estimate of these quantities based on the material distribution in ATLAS is provided for $\eta = 0$ and $\eta = 1$ for particles crossing the distance from R = 0 cm at the detector origin to R = 100 cm in the ID. These average values have been calculated as the sum of all involved material quantities weighted by the length l_i of the ith material that is seen by the traversing particle.

$$\rho = \frac{\sum \rho_i l_i}{\sum l_i} \tag{6.4}$$

$$A = \frac{\sum \rho_i l_i}{\sum n_a l_i} N_A \tag{6.5}$$

$$Z = \frac{\sum n_e l_i}{\sum n_a l_i} \tag{6.6}$$

$$X_0 = \frac{\sum l_i}{\sum l_i / X_{0_i}} \tag{6.7}$$

The variable n_e denotes here the electron density, n_a the atomic density of the materials and N_A is the Avogadro constant. This estimation is transferred to the cosmic tracks, neglecting the fact that cosmic tracks do not originate from the center and have different trajectories in the Inner Detector. To obtain an estimation of the average material quantities for the cosmic tracks' mean η position[18], the values from [41] are linearly extrapolated to this position.

The resulting values for the material properties are listed in table 6.2. The indicated errors given consist of the two main systematic uncertainties - the uncertainty which occurs by simply assuming one average η for all tracks, and the uncertainty from the linear extrapolation of the mean material quantities. The latter is estimated as the mean deviation of the calculated average material values at $\eta = 0.42$ from the given $\eta = 0$ and $\eta = 1$ cases. An estimation of the error on the provided values from [41] is not included.

Finally, to gain an estimate of the average total number of electrons produced via different processes in the ID barrel, the total number of cosmic muon events in this volume needs to be determined from cosmic data used for this analysis. In total 3539264 events with at least one high-level trigger track candidate in the ID are investigated. Only a small fraction of these events containing the electron and photon candidates is used for further analysis (see sec. 4.5). In total 10611 electron candidates can be found in this data sample. After applying a cut to reduce the investigated tracks basically to the ID barrel (see sec. 7.1), 10421 candidates remain.

[17] The electron mass is neglected.

[18] The average η is determined from the mean θ angle as $\eta = 0.42 \pm 0.29$.

	Extrapol. material properties
Z	5.40 ± 0.62
A[g/mol]	10.65 ± 1.27
$\rho\left[\frac{g}{cm^3}\right]$	0.125 ± 0.022
X_0 [cm]	259.3 ± 72.1

Table 6.2: Average material properties (nucleus charge, atomic mass, density and radiation length) at $\eta = 0.42$ calculated for the Inner Detector

The fraction of tracks in the ID barrel compared to the total number of ID tracks is 98%[19]. Transferred on the total number of cosmic events this yields the average total number of cosmic events in the ID barrel for which the expected number of electrons can be calculated.

6.2 Muon Decay

One process, which can lead to the emission of high energy electrons in the Inner Detector, is a decay of the cosmic muon in flight. The muon decays into an electron and the respective two neutrinos (see eq. 2.1). A sketch of the process in ATLAS is shown in figure 6.1 (left). The detector sees one incoming muon which enters the upper muon system, the upper Calorimetry and the Inner Detector. Here it decays to an electron which is typically emitted under a very small angle due to the high momentum of the muon. The electron also leaves a track in the Inner Calorimeter and showers in the lower hemisphere in the EM. Thus, the signature of this process according to the reconstruction of cosmic events in ATLAS (sec. 4.2) should be one incoming muon ($\phi > 0$), one track in the Inner Detector - the kink is too small to distinguish the two consecutive individual tracks - and one cluster in the Electromagnetic Calorimeter. The matching cluster and ID track form the electron candidate. There should be no outgoing muon candidate at ($\phi < 0$).

To calculate analytically the number of electrons produced by decay per incoming muon, the decay law can be used (e.g. [42]). The number of muons which have not decayed after a path length d_{in} before entering the ATLAS ID and the path length d_{out} after leaving it is therefore:

$$N(d_{\text{in/out}}) = N(0)e^{-\frac{d_{\text{in/out}}}{\Lambda}} \tag{6.8}$$

The variable N(0) denotes the initial number of muons in the atmosphere, and Λ is the decay length in the laboratory system. From this equation the number of muons can be calculated which did not decay during the crossing of the ID can be calculated depending on the number of muons $N(d_{\text{in}})$ entering the ID:

$$N(d) = N(d_{\text{in}})e^{-\frac{d}{\Lambda}} \tag{6.9}$$

In this case $d = d_{\text{out}} - d_{\text{in}}$. The decay length can be expressed via the muon's proper time τ in its rest frame $\Lambda = vT = \beta c\gamma \cdot \tau$, with $\beta\gamma = \frac{p_\mu}{m_\mu c}$, the muon momentum p_μ and mass m_μ. The number of electrons produced in a decay of the cosmic muon inside the Inner Detector per cosmic muon is therefore:

$$N_{e_{\text{dec}}}(d) = 1 - \frac{N(d)}{N(d_{\text{in}})} = 1 - e^{-\frac{d \cdot m_\mu}{p_\mu \cdot \tau}} \tag{6.10}$$

In order to calculate the number of electrons for this process expected in the ATLAS ID, the average quantities of cosmic muons received from data are used for momentum and path

[19] The error on this value is neglected for the calculations.

length (see table 6.1): The effective mean path length of the cosmic muons in the ID $d = d_{\text{corr}}$ is inserted, and the average cosmic muon momentum truncated at 100 GeV, $p_\mu = p_\mu^{\text{low}}$. This truncated mean is used here because the contribution of high-energy muons to the number of electrons produced in decays is very small since their lifetime is much larger than the time they need to cross the ID. With $\tau = 2.2 \cdot 10^{-6}$s and $m_\mu = 105.6$ MeV/c^2 the resulting number of electrons produced in decays per cosmic muon is obtained:

$$N_{e_{\text{dec}}} = (4.9 \pm 3.1) \cdot 10^{-6} \tag{6.11}$$

Only the uncertainties on the effective path length and the mean muon momentum contribute significantly to the error on this value and have been considered (tab. 6.1). Transferred on the number of events crossing the Inner Detector barrel, this yields an expectation of 17 ± 11 electrons from muon decays in cosmic data.

As explained above, the boost of the electron in the decay in the investigated energy range is very large, thus its angle with respect to the incoming muon is very small. If the neutrinos are emitted collinearly in the muon rest frame, the electron carries a maximal transverse momentum of 0.5 m_μ with respect to the muon flight direction. Since the minimal total electron energy is estimated to have a value of 3.27 GeV (see table 6.1), this yields a maximal angle of 0.02 rad between the initial muon and the boosted electron.

The obtained result for the expected number of electrons from decay in the ATLAS ID is compared to the truth electrons of the full cosmic Monte Carlo data (see sec. 5.1). Decay electrons are identified in the Monte Carlo truth by the particle identity of their mother particle and its additional decay products. All electrons which originate from a muon and are accompanied by neutrinos are defined as electrons from muon decays.

In total, there are 503 decay electrons produced inside the ID in the Monte Carlo truth data for the full electron energy range. Considering the total number of MC events (9780293), this yields $5.1 \cdot 10^{-5}$ electrons from decay per traversing muon. This value is one order of magnitude larger than the expectations from the analytical calculation (eq. 6.11). This can be explained by the fact that mostly electrons with low energies are contained among these truth candidates which are most likely produced by muons with lower energies as muon and electron energy are correlated to a certain extent (see e.g. [43]). The insertion of a single value for the muon momentum averaged over a range up to 100 GeV for the analytical calculation underestimates this low energy contribution. However, the minimal required energy of the electron in ATLAS for a reconstruction is 3.27 GeV (see sec 4.3). If in the MC truth data only electrons with high energies above 3.27 GeV are considered, indeed only 89 decay events remain in the MC sample which corresponds to 9.1 $\cdot 10^{-6}$ electrons per trespassing muon. This value is much closer to the expectation from the calculation. A direct comparison between the two values can of course not be made as the calculation does not include any restrictions on the electron energy. Nevertheless, the insertion of the truncated mean of 44.52 GeV for the muon energy biases the calculation towards electrons in the GeV region as already explained. In addition, the truth data includes all decay electrons produced in the ID and does not account for the fact that the electrons have to fly a certain distance to be reconstructed (sec. 6.1). Thus, the number of reconstructable truth events reduces even more and approaches the analytical estimation.

One can therefore conclude that the order-of-magnitude estimation on the number of high energy electrons from decay estimated by a rough analytical calculation is consistent with the MC truth data, although the latter contains a much more accurate simulation of the muon momentum spectrum and individual path lengths of the cosmic tracks.

6.3 Delta electrons

Cosmic muons traversing the ATLAS detector lose energy through interaction with the material. If their energy is below 100 GeV, they lose energy mainly by ionization and excitation of atoms according to the Bethe-Bloch formula [13], [44] as minimum ionizing particles. During these interactions it might happen that a high-energy delta electron is knocked off which has an energy of several GeV. A sketch of this process is illustrated in fig. 6.1 (second from left). The incoming muon crosses the upper MS and Calorimetry and leaves a track in the Inner Detector. Here it knocks off an electron which leaves a second track in the ID and a shower in the lower hemisphere of the EM. The muon leaves the detector again traversing the lower Calorimetry and MS, as well.

High energy delta electrons are typically emitted in the forward direction with respect to the path of the muon (see below), and thus the two tracks in the ID are close-by. The signature for this process can be summarized as: two reconstructed muon candidates, one incoming at $\phi > 0$ and one outgoing at $\phi < 0$, and two close-by ID tracks, one of which is the electron with a matching cluster at $\phi < 0$.

The spectrum of the delta electron's kinetic energy can be derived from the kinematics in a collision of a highly relativistic muon and a target electron at rest [13]. The kinetic energy T is dependent on the electron angle θ with respect to the incoming muon direction:

$$T(\theta) = \frac{2\gamma^2\beta^2 m_e c^2 \cos^2\theta}{\gamma^2(1-\beta^2\cos^2\theta) + \frac{m_e^2}{M_\mu^2} + 2\gamma\frac{m_e}{M_\mu}} \tag{6.12}$$

The variables M_μ and m_e denote muon and electron mass and γ, β the relativistic factors of the muon. In the high relativistic limit ($\gamma \gg 1$, $\beta \approx 1$) this reduces to:

$$T(\theta) = \frac{2m_e c^2}{\tan^2\theta} \tag{6.13}$$

For electrons with high kinetic energies as required for the studies of cosmic data, the emission angle is thus relatively small with respect to the incoming muon as can also be seen in figure 6.4. The insertion of the minimal required electron energy $T = 3.27$ GeV yields a maximal angle of 0.02 rad.

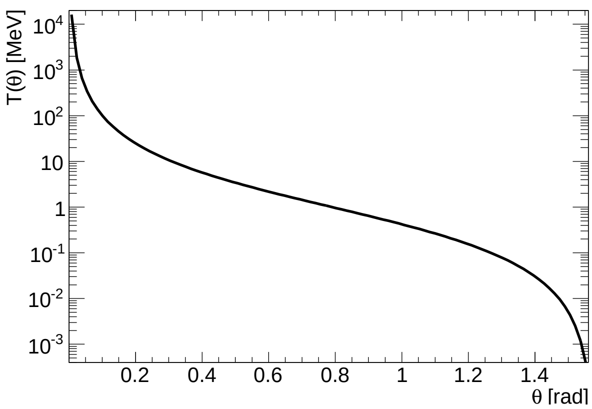

Figure 6.4: The kinetic energy $T(\theta)$ of delta electrons dependent on the emission angle θ with respect to the flight direction of the muon in the high relativistic limit.

The cross section for the production of a delta electron can be derived from the Rutherford scattering formula assuming that the muon is scattered through a Coulomb interaction with a single electron of the atomic shell, and that it has an energy which is large compared to the binding energy of the atom.

The four-momentum transfer is proportional the electron kinetic energy, inserted into the formula this yields the following cross section [45]:

$$\frac{d\sigma}{dT} = \frac{2\pi z^2 \alpha^2 \hbar^2 c^2}{\beta^2 m_e c^2} \frac{1}{T^2} \tag{6.14}$$

The variable z denotes the charge of the incoming particle which is one in the case of muons and α is the fine structure constant. An additional term accounting for the spin dependency of the cross section is neglected here, since it can be assumed to have an order-of-magnitude of one over a large energy range[46].

The differential number of delta electrons per path length and per kinetic energy can be obtained via the electron density in the material:

$$\frac{d^2 N}{dx dT} = n_e \frac{d\sigma}{dT} \tag{6.15}$$

The electron density is $n_e = \frac{\rho}{A} N_A Z$, with N_A the Avogadro constant, A the atomic mass, Z the nucleus charge and ρ the density of the material.

Integrating over the energy range and the path length, one finally obtains the number of delta electrons produced per traversing muon [13]:

$$N_{e_{\mathrm{del}}} = \frac{1}{2} \frac{\rho}{A} Z \frac{1}{\beta^2} K \left(\frac{1}{T_{\mathrm{min}}} - \frac{1}{T_{\mathrm{max}}} \right) \cdot d \tag{6.16}$$

Here, $K = 4\pi N_A r_e^2 m_e c^2 = 0.307 \frac{\mathrm{MeV}}{\mathrm{g}} \mathrm{cm}^3$ with r_e denoting the classical electron radius and d denoting the path length. The maximal kinetic energy of the electron is reached in the case for $\theta \to 0$ (see eq. 6.13). In the relativistic high-energy limit this is simply the muon energy:

$$T_{\mathrm{max}}(\theta \to 0, \gamma \to \infty) = \gamma M_\mu c^2 = E_\mu \tag{6.17}$$

The minimal kinetic electron energy is limited by the mean excitation energy of different atoms. In the high relativistic limit it is negligibly small [13].

For an estimation of the number of delta electrons emitted during muon interactions inside the Inner Detector of ATLAS, the calculated mean and minimal values for muon and electron energy and the ID material (see tab. 6.1 and 6.2) are inserted in eq. 6.16. For the path length d the effective mean path length of muons in the ATLAS ID detector d_{corr} is assumed. The mean material properties calculated for the ID are used. As the minimal kinetic energy of the electron T_{min} the minimal energy limit for the cluster reconstruction is assumed. As maximum kinetic energy of the electron T_{max} the average muon momentum $p_\mu^{\mathrm{low}} c$ truncated at 100 GeV is chosen since muons with higher momenta contribute only weakly to the number of knocked-on delta electrons. For this relativistic energy β is approximately one.

The result of this calculation yields the expected number of delta electrons ejected per cosmic muon which crosses the ID:

$$N_{e_{\mathrm{del}}} = (3.7 \pm 1.6) \cdot 10^{-4} \tag{6.18}$$

The uncertainty of this value is dominated by the largest systematic uncertainties. These arise from the averaging over the material properties and the assumption of an average effective path length for muons and of a minimal and maximal energy for electrons (see table 6.1 and 6.2). Transferred to the total number of cosmic muons crossing the ID barrel, this yields an expected total number of 1301 ± 562 delta electrons in the cosmic data sample.

The result of this analytical calculation and the associated energy distribution of delta electrons are compared to the delta electron spectrum in the truth data of the cosmic Monte Carlo sample.

To obtain the number of high-energy electrons in the Monte Carlo truth all delta electrons with energies above 3.27 GeV are extracted. They are identified via the particle identity of their mother particle and the other decay products. Truth electrons which originate from a muon and are not accompanied by neutrinos are declared to be delta electrons from ionization processes. In the total MC sample these are 2928 events. With respect to total number of Monte Carlo events (9780293) this yields a number of $3.0 \cdot 10^{-4}$ delta electrons per cosmic muon traversing the Inner Detector. This number shows a very good agreement with the number obtained from the analytical estimation (see eq. 6.18) within the errors, although for the Monte Carlo simulation much more accurate descriptions of path length and material properties are included. The good agreement of the results reveals that the much coarser theoretical calculation based on simple average values nevertheless gives a reliable estimation of the order-of-magnitude expectation for this process.

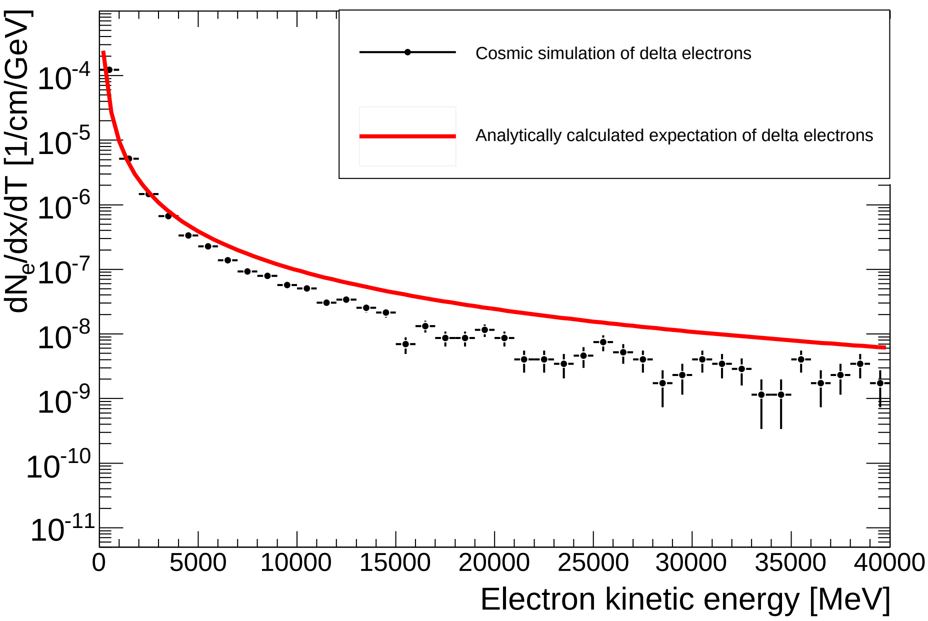

Figure 6.5: Absolute fraction of delta electrons from muon ionization processes per path length and energy. Shown is the analytical calculation for the expected number of electrons as a red curve and the energy spectrum of truth delta electrons in the cosmic Monte Carlo sample per traversing muon as black dots. The latter is normalized by the mean cosmic track path length in MC data and the total number of cosmic events in the sample. (No additional scaling or normalization is done.)

In fig. 6.5 the differential number of delta electrons per path length and energy expected per cosmic muon dependent on the electron energy is compared for the analytical estimation and the Monte Carlo truth electrons. The distribution of the truth energy of all truth delta electrons in the cosmic MC sample is normalized by the total number of events in the sample (9780293) and the estimated total mean path length determined from all tracks of the Monte Carlo sample (d = 177.3 ± 54.5cm). The mean path length has been estimated in the same way as described for the real data sample (sec. 6.1). The distribution obtained from the analytical calculation of the differential number of expected delta electrons is shown per path length and energy according to eq. 6.15. Again, a good agreement between the rough analytical calculation and the spectrum of the MC truth electrons can be seen. In the low-energy range both distributions coincide, while towards higher energies the analytically calculated curve indicates a slightly higher number of electrons than the number found in the Monte Carlo sample by up to about a factor of two at 40 GeV. This could be a result of the omitted spin dependent term in the calculations since it postulates a slightly stronger decrease of the number of delta electrons at very high electron energies [46]. Of course, also the Monte Carlo simulation of these very unusual and rare processes where a high-energy delta electron is emitted might not be accurate, as the state of experimental verification is not clear. Obviously, the probability for the emittance of a high-energy delta electron according to equation 6.13 in forward direction is several orders of magnitude smaller than the probability that a low-energy delta electron is knocked off with an angle close to $\pi/2$ with respect to the muon flight direction.

All in all, the two different estimations obtained for the expected number of delta electrons from cosmic muons in the ATLAS ID - the analytical calculation and the extraction of the cosmic MC truth information - show a very good agreement, and they provide therefore a reliable prediction on the number of electrons which can be expected in cosmic data.

6.4 Conversion of bremsstrahlung photons

Towards larger energies muons increasingly lose energy through bremsstrahlung in matter under the influence of the Coulomb field of a nucleus in addition to ionization [13],[44]. These emitted bremsstrahlung photons can in turn convert to an electron-positron pair near an atomic nucleus, if they carry a sufficiently large momentum. If the pair is produced in the Inner Detector and carries also a large fraction of the initial muon energy, it can be reconstructed as electron candidates in ATLAS.

A sketch of the process can be seen in fig. 6.1 (third from left). The incoming muon passing the upper MS and Calorimeters traverses the ID and emits a bremsstrahlung photon there. The photon does not leave a track in the ID itself but it turns into an electron-positron pair which leave two additional ID tracks and two matching clusters in the lower EM. Also in this case, the clusters and tracks should be very close-by (see below). The muon continues its path and traverses the lower Calorimeters and MS. The signature for this process is thus two muons, one incoming and one outgoing at $\phi > 0$ and $\phi < 0$, three tracks in the ID and 2 electron candidates. In most cases only one electron/positron of the pair is reconstructed. If the second electron/positron has a too low momentum, it is bent too much in its trajectory by the solenoid field in the ID to be reconstructed. If both have a high momentum, their tracks lie very close to each other and their energy depositions in the Calorimeter overlap which leads to the reconstruction of only one electron candidate. These events have then the same signature as a delta electron and can only be distinguished if the reconstructed candidate has a positive charge since delta electrons always have a negative charge.

For an estimate of the number of electron-positron pairs which should occur in cosmic ray data, first the number of bremsstrahlung photons produced by the cosmic muons in the ID needs to be known. This number has then to be multiplied by the number of converted photons which is thus the total number of electron-positron pairs.

The differential cross section for muon bremsstrahlung can be calculated in the Born approximation depending on the photon energy E_γ and the muon energy E_μ [47], [48]:

$$\frac{d\sigma_\gamma}{dE_\gamma} = \alpha \cdot Z(Z+1)\left(2r_0\frac{m_e}{m_\mu}\right)^2\left(\frac{4}{3}\frac{1}{E_\gamma} - \frac{4}{3}\frac{1}{E_\mu} + \frac{E_\gamma}{E_\mu^2}\right) \cdot \log\frac{C\cdot(1+D\cdot\frac{E_\gamma}{E_\mu - E_\gamma})}{1+B\cdot\frac{E_\gamma}{E_\mu-E_\gamma}} \tag{6.19}$$

$$C = 182.7\frac{1}{1.54A^{0.27}}\frac{m_\mu}{m_e}Z^{-1/3} \tag{6.20}$$

$$B = \frac{1}{2}182.7\sqrt{e}\frac{m_\mu^2}{E_\mu m_e}Z^{-1/3} \tag{6.21}$$

$$D = \frac{1}{2}(1.54A^{0.27}\sqrt{e} - 2)\frac{m_\mu}{E_\mu} \tag{6.22}$$

The logarithmic factor depending on the nucleus charge Z and the atomic mass A accounts for the influence of atomic and nuclear form factors on the cross section. They include the modification and screening of the Coulomb field due to the electrons in the atomic shell and the finite size of the nucleus. This effect depends on the distance in which the muon interacts with the nucleus and thus on the momentum transfer to the nucleus[20][48]. An additional term in the bremsstrahlung cross section arises from a contribution of the scattering of the muon on electrons in the atomic shell. This contribution is covered by the Z(Z+1) term in the equation which replaces the pure nucleus scattering factor Z^2. This is not the most exact account for this distribution, but it is a simplifying approximation used for the calculations [47].

The number of bremsstrahlung photons produced per path length and energy can be calculated using the density of atoms $n_a = \frac{\rho}{A}N_A$ in the material:

$$\frac{dN_\gamma^2}{dE_\gamma dx} = n_a\frac{d\sigma_\gamma}{dE_\gamma} \tag{6.23}$$

Next, the second process, the conversion of a photon into an electron-positron pair near the Coulomb field of a nucleus, needs to be investigated. This process is dominant for photons at large energies, e.g. in Carbon for energies larger than about 100 MeV [13].

The cross section for the production of a conversion e^+/e^- pair is related to the bremsstrahlung process. It is also calculated in Born approximation depending on the energy E_e of one candidate of the e^+/e^- pair[21] [49], [13]:

$$\frac{d\sigma_e}{dE_e} = \frac{A}{\rho X_0 N_A}\frac{1}{E_\gamma}(1 - \frac{4}{3}\frac{E_e}{E_\gamma} + \frac{4}{3}\frac{E_e^2}{E_\gamma^2}) \tag{6.24}$$

This cross section also depends on the energy of the bremsstrahlung photons E_γ. In order to obtain the number of electron-positron pairs produced by muons through bremsstrahlung with a subsequent conversion, the expected numbers for both processes have to be combined. The number of e^+/e^- pairs per electron and photon energy and path length can then be calculated from the conversion cross section, the atomic density n_a and the differential number of photons per energy and path length:

[20] For the more familiar electron bremsstrahlung only atomic form factors influence the cross section, due to their much smaller mass and therefore in general much smaller momentum transfers to the nucleus.

[21] The energy of the second candidate of the pair is thus $E_\gamma - E_e$ if the rest mass of the electrons is neglected.

$$\frac{d^4N_e}{dE_e dx dE_\gamma dx} = n_a \frac{d\sigma_e(E_\gamma)}{dE_e} \frac{dN_\gamma}{dE_\gamma dx} \tag{6.25}$$

The total expected number of e^+/e^- pairs after a path length d can be calculated as a double integral over the photon energy and the energy of one candidate of the pair:

$$\begin{aligned} N_{e_{\mathrm{conv}}} &= d^2 \frac{N_A^2}{A^2} \rho^2 \int_{E_\gamma^{min}}^{E_\gamma^{max}} \int_{E_e^{min}}^{E_\gamma} \frac{d\sigma_\gamma}{dE_\gamma} \frac{d\sigma_e}{dE_e} dE_e dE_\gamma \\ &= d^2 \frac{N_A}{X_0 A} \rho \cdot \alpha \cdot Z(Z+1) \left(2r_0 \frac{m_e}{m_\mu}\right)^2 \int_{E_\gamma^{min}}^{E_\gamma^{max}} \int_{E_e^{min}}^{E_\gamma} \left(\frac{4}{3}\frac{1}{E_\gamma} - \frac{4}{3}\frac{1}{E_\mu} + \frac{E_\gamma}{E_\mu^2}\right) \cdot \\ &\quad \log\left(\frac{C \cdot (1 + D \cdot \frac{E_\gamma}{E_\mu - E_\gamma})}{1 + B \cdot \frac{E_\gamma}{E_\mu - E_\gamma}}\right) \frac{1}{E_\gamma} (1 - \frac{4}{3}\frac{E_e}{E_\gamma} + \frac{4}{3}\frac{E_e^2}{E_\gamma^2}) dE_e dE_\gamma \end{aligned} \tag{6.26}$$

The variables B, C and D are the ones from eq. 6.20-6.22. It should be noted that for both processes a simplified integration over the full path length d of the muons in the ID is performed. The effect that the photons effectively see only a smaller path length on which they can create an electron-positron-pair is neglected. A second simplifying approximation is the assumption of a mean muon energy for this calculation instead of an integration over the full cosmic muon spectrum.

To calculate an average number of expected e^+/e^- pairs produced via this process by cosmic muons in the ATLAS Inner Detector barrel, the average quantities for material and muons calculated in sec. 6.1 are used. The effective mean path length $d = d_{\mathrm{corr}}$ of the cosmic muons is inserted (table 6.1) and the average material quantities A, Z, ρ and X_0 (table 6.2).

The truncated mean $p_\mu^{\mathrm{high}} c$ for muon momenta < 10 TeV of table 6.1 is used as an average muon energy, since bremsstrahlung becomes only dominant for muon energies above several hundred GeV [13]. The integration boundaries are given by the minimal photon energy and energy of one candidate of the e^+/e^- pair, $E_\gamma^{\min} = E_e^{\min} = 3.27$ GeV which is the threshold for the electron cluster reconstruction in ATLAS. The maximal photon energy used for the integration is $E_\gamma^{\max} = 199.9$ GeV which is the average muon energy $p_\mu^{\mathrm{high}} c$ less its rest mass. After a numerical integration with the help of the software *Mathematica* over the photon and electron energy of one of the pair, the average expected number of electron-positron pairs with at least one high energy candidate originating from bremsstrahlung photon conversions is gained which are produced in the ID per traversing muon:

$$N_{e_{\mathrm{conv}}} = (1.9 \pm 1.6) \cdot 10^{-5} \tag{6.27}$$

The uncertainty on this value is composed of the main systematic uncertainties on the averaged quantities used for the calculation according to tab. 6.1 and 6.2[22]. The total number of conversion pairs with at least one high energy electron of the pair expected for all muons crossing the ID barrel in cosmic data is then 65 ± 57.

The average emission angle of the photon with respect to the incoming muon direction is approximately $\theta_\gamma = \frac{m_\mu c^2}{E_\mu}$, while the angle between the initial photon and one of the produced electrons/positrons is $\theta_e = \frac{m_e c^2}{E_e}$. For energies of several GeV the particles are therefore very close-by. Inserting as an example the mean muon energy and the minimal electron/positron

[22]The error made by inserting the full effective path length of muons for the bremsstrahlung and the conversion process as explained above is neglected here.

energy, this yields a typical angle of 0.001 rad between incoming muon and electron or positron of the e^+/e^- pair.

The results from these analytical calculations have also been compared to the truth events contained in the Cosmic Monte Carlo sample. All electron candidates which have a photon mother that in turn orginates from a muon are flagged as electrons or positrons from bremsstrahlung photons. They occur exclusively as pairs in the truth data, as expected. The number of pairs in which at least one of them has an energy above 3.27 GeV is 784 in the whole data set. This yields $8.0 \cdot 10^{-5}$ produced pairs in the ID per trespassing muon with respect to the total number of cosmic events in the data sample.

This number agrees in order of magnitude with the result received from the analytical calculation (eq. 6.27). Nevertheless, it is by a factor four higher. This can partially be attributed to the fact that the truth conversion pairs in the MC sample are distributed over the full ID volume which does not take into account that the electron/positron candidates have to cross a certain path in the ID to leave a reconstructable trajectory. Inserting the full path length from table 6.1 in eq. 6.26 doubles the expected number of conversion pairs. This reduces the difference between the conversion pairs of the Monte Carlo truth and the analytically calculated number to a factor of two. These remaining discrepancies might come from the approximation of mean material quantities for the whole detector material. The atomic mass A and the nucleus charge Z have a large influence on the nuclear and atomic form factors. This might lead to different results in comparison to the Monte Carlo simulations of conversion processes which use a more accurate description of the individual material components and the respective form factors. Of course, also the MC simulation of these rare high-energy conversion processes might not be totally accurate.

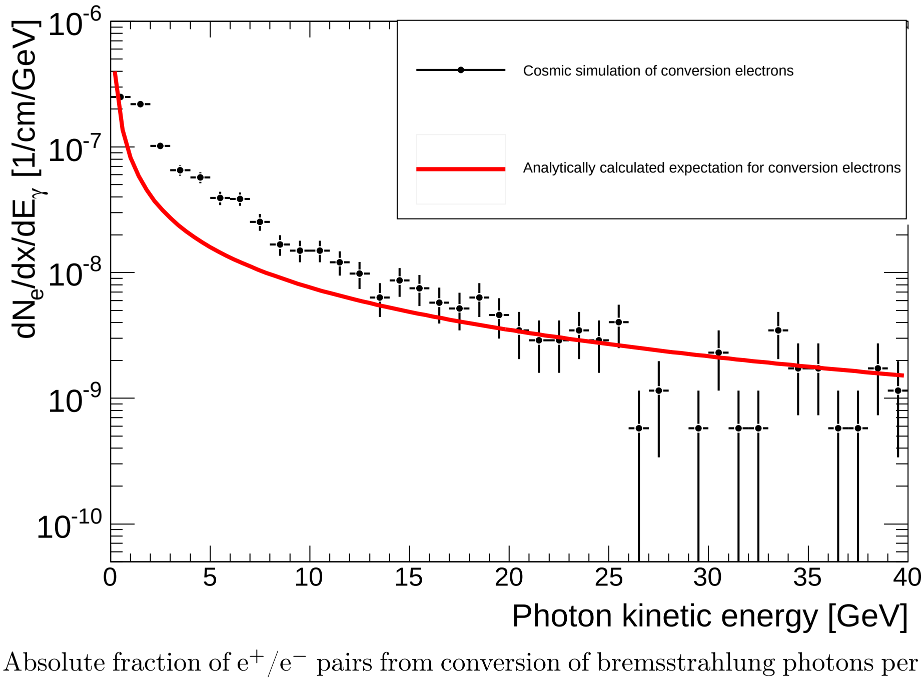

Figure 6.6: Absolute fraction of e^+/e^- pairs from conversion of bremsstrahlung photons per path length and photon energy expected per traversing cosmic muon in the ID versus the photon energy. Displayed is the analytical calculation of the differential number of conversion pairs as a red curve. The spectrum of truth conversion electron/positron pairs in the cosmic Monte Carlo sample is displayed as black dots which is normalized to the total average path length and the total number of cosmic events contained in the cosmic MC sample. (Besides this no scaling or normalization is done.)

In fig. 6.6 the differential number of conversion pairs per path length and photon energy is compared for the analytical estimation and the Monte Carlo truth electrons dependent on the bremsstrahlung photon energy.

For each truth conversion pair in the cosmic MC sample the sum of the positron and electron truth energy is extracted and displayed which is thus the energy of the bremsstrahlung photon. The number of conversion pairs is normalized by the total number of cosmic muon events contained in the MC sample and by the mean total path length estimated for the Monte Carlo data sample (d= 177.3 ± 54.5 cm).

To display the analytical estimation of the fractional number of conversion pairs, the differential number of bremsstrahlung photons is calculated from eq. 6.19 and 6.23. This number is then multiplied by the conversion probability in the ID for an individual photon which is the integral of the differential cross section for conversion over the energy of one pair candidate times the atomic density and the path length of cosmics in the ID (see eq. 6.24 and 6.25)[23].

The distributions show a relatively good agreement in order of magnitude. In the lower energy region a larger difference can be observed between them. This discrepancy can also be ascribed to the different methods which are implemented to describe the number of conversion events, as discussed above.

In spite of the observed differences, the analytical calculation of the number of expected conversion pairs with at least one high-energy candidate produced in the ID by cosmic rays agrees in order-of-magnitude with the electron/positron pair number extracted from the truth information of the Monte Carlo sample. It thus gives an estimation on what can be expected in real cosmic data.

6.5 Background process: Muon bremsstrahlung

One important background process which leads to the reconstruction of fake electrons in ATLAS, needs to be considered for cosmic data. As discussed in the previous subsection, the fraction of muon energy losses by radiation increase for high muon energies and becomes the dominant process above several 100 GeV. Bremsstrahlung photons which are emitted in the Inner Detector or in the Electromagnetic Calorimeter at $\phi < 0$ deposit their energy also in a shower in the lower hemisphere of the EM. The photon as a neutral particle does not leave a track in the ID, but since the average angle between the incident muon and the photon is given by $\theta = \frac{m_\mu c^2}{E_\mu}$, the photon is often emitted in forward direction with respect to the muon's trajectory, and photon and muon lie very close-by (compare sec. 6.4). Therefore, if a cluster produced by a bremsstrahlung photon with high energy is found by with the *sliding-window* algorithm, it can by mistake be matched to the close-by muon track and fake an electron candidate.

A sketch of this process is shown in fig. 6.1 (right). The muon track crosses the upper MS and Calorimetry and subsequently the Inner Detector. Here, it radiates a photon which showers in the EM at $\phi < 0$, while the muon continues its path trespassing also the lower Calorimetry and MS. The signature for this process is therefore (see sec. 4.3) two muon candidates, one at $\phi > 0$, one at $\phi < 0$, one ID track and a faked electron candidate with a cluster in the lower EM. This signature can be clearly distinguished from the real electron production processes by the number of tracks in the ID and the number of muon candidates. Nevertheless, through mistakes in the reconstruction the signature may be indistinguishable from the real processes. For instance, it might happen that for these muon bremsstrahlung processes an additional second track is by mistake reconstructed which leads to an event with the same signature as the process of delta

[23]This roughly halves the number of bremsstrahlung photons.

electron production. If the lower muon candidate is not reconstructed, a muon bremsstrahlung event with one track in the ID is indistinguishable from a muon decay electron.

The expected number of bremsstrahlung photons emitted by cosmic muons in the ID can be analytically calculated by eq. 6.19-6.23, as well. It is approximately by a factor two higher than the expected number of conversion pairs resulting from bremsstrahlung photons (see sec. 6.4) if the same material and particle quantities are assumed. Nevertheless, bremsstrahlung can also be emitted by the muon inside the EM to form an electromagnetic shower. Since in the Calorimeters a much larger amount of material is contained than in the ID, the probability for a photon emission is much higher for cosmic muons, and thus the total number of bremsstrahlung photons will be much higher than calculated by eq. 6.19-6.23. Therefore, a quite large background of fake electron candidates by muon bremsstrahlung can be expected for the cosmic data.

6.6 Summary of processes

Three different sources of high-energy electrons in cosmic muon events have been identified: Muon decay in flight, delta electron emission in ionization processes and conversion of photons radiated by muons. In addition, muon bremsstrahlung has been revealed to be a source of background producing fake electron candidates. The discussion and investigation of the different electron production and background processes clarified that they have principally different signatures inside the ATLAS detector, on the basis of which they can be distinguished.

Furthermore, analytical order-of-magnitude calculations of the expected numbers for each of these processes also revealed large differences, in agreement with the investigation of truth electrons in the cosmic Monte Carlo sample. A summary of these calculations can be found in table 6.3.

Process	Expect. No. of e per μ	Total expected No. of e	No. of e per μ, MCTruth
Delta el.	$(3.7\pm 1.6)\cdot 10^{-4}$	1301 ± 562	$3.0 \cdot 10^{-4}$
Photon conv.	$(1.9\pm 1.6)\cdot 10^{-5}$	65 ± 57	$8.0 \cdot 10^{-5}$
Decay	$(4.9\pm 3.1)\cdot 10^{-6}$	17 ± 11	$9.1 \cdot 10^{-6}$

Table 6.3: Calculated number of expected electrons in the ATLAS ID barrel in cosmic data produced via different processes and numbers of MC truth electrons

It is obvious that mainly delta electrons with high energies are expected to occur and be detected in ATLAS, as this production process is the most probable one. Therefore, efforts in finding electrons in data and distinguishing them from the muon bremsstrahlung background process will concentrate on this kind of electrons. These calculations are of course only rough estimations of the expected electron numbers. Nevertheless, the quite nice agreement with the cosmic Monte Carlo truth makes them reliable in the order-of-magnitude that can be expected in cosmic data.

7 Search for high-energy electrons in ATLAS cosmic ray data

In this chapter a method will be described to isolate a sample of high-energy electrons from cosmic ray data. The basis for this analysis is the data sample described in sec. 4.5. The study will focus on finding delta electrons from ionization processes, as this is expected to be the main source of electrons in ATLAS. For a separation of real electrons from the main background of muon-bremsstrahlung photons, first the different detector signatures of these processes will be exploited to form two subsamples of data primarily containing events of either background or signal. In addition, the identification tools given by ATLAS will be utilized to finally isolate the real electrons which make use of characteristic electron properties based on the combined information from ID track and EM cluster. First the choice of cuts for the subsamples will be motivated, then the identification cut selection will be described in its modifications for the special cosmic data topology and the results of this analysis will be presented. The extracted candidates will be investigated further concerning the shapes of their shower in the Calorimeter and other special properties. For the analysis ATHENA release 15.0.0 is used.

7.1 Isolation of delta electrons from a real cosmic data sample

As a starting point for the analysis to find the electrons in the cosmic-ray data sample, all electron candidates of the container *ElectronAODCollection* are considered (10611). These are all candidates reconstructed by the cluster-based algorithm (*egamma*) or the track-based algorithm (*softe*) (see sec. 4.3). Due to the special filtering of the input data sample, only cosmic muon events with at least one high-level trigger track candidate in the ID are included (see sec. 4.5). An initial cut is applied to the electron tracks to reduce the analysis mainly to the ID barrel part of the detector. Here the electron reconstruction is expected to be most efficient for tracks crossing the detector from upside down because the straw tubes of the TRT are situated transverse to the particle's trajectory. In the end-caps the straws are arranged radially in the detector, they are thus parallel to the cosmic-ray trajectories and no accurate track reconstruction is possible. The longitudinal impact parameter of the electron candidate tracks is required to be $|z_0| < 1000$ mm. After this cut, 10421 electron candidates remain, thus a fraction of 0.98. This shows that the electron-reconstruction efficiency in the ID end-caps is at a low level as expected, although the cosmic muon flux is large due to the access shafts which are located above.

Investigation of basic properties of the electron candidates in cosmic data

In table 7.1 the percentage of all electron candidates found by either the cluster-based or the track-based algorithm or both of them is listed.

	egamma	softe	both
Candidates	99.1%	0.7%	0.2%

Table 7.1: Fraction of electron candidates found by the two different reconstruction algorithms

As expected (see sec. 4.3), the electrons from cosmic events are nearly exclusively found by the *egamma* algorithm. This is a consequence of the fact that for the *softe* algorithm the track quality criteria cannot be fulfilled by the majority of cosmic tracks, e.g. a minimum number of silicon hits or a small transverse impact parameter. The majority of electron candidates originating from cosmic muons in most cases only have few or no silicon hits and cross the Inner Detector at arbitrary distances with respect to the center.

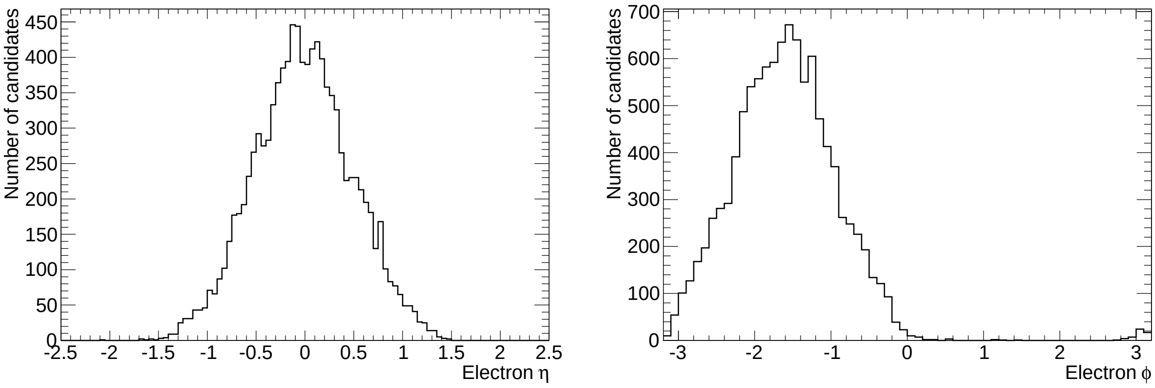

Figure 7.1: η (left) and ϕ (right) distribution of all electron candidates in cosmic data.

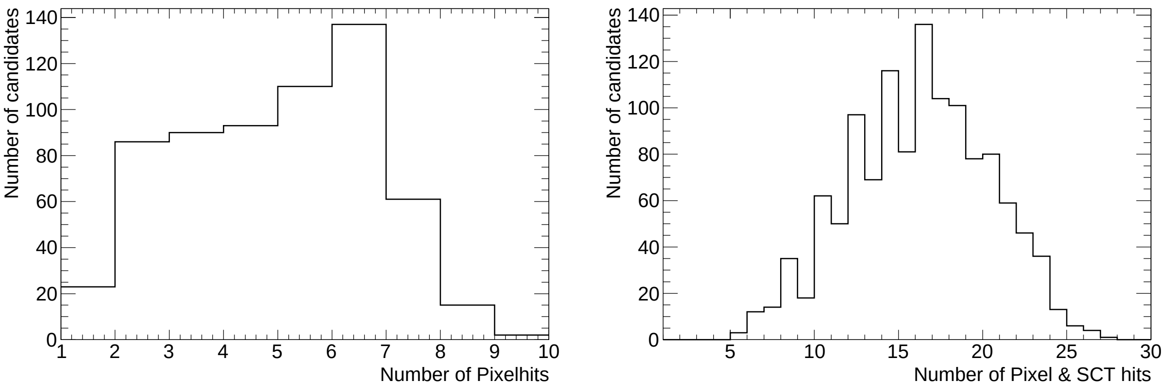

Figure 7.2: Left: Number of Pixel hits of all electron candidates, not included in the figure are 9200 events with no Pixel hits. Right: Number of Pixel and SCT hits of all electron candidates, not displayed are 9804 events with no Pixel and SCT hits.

In fig. 7.1 the η and ϕ distributions of the electron candidates are illustrated which are evaluated at the cluster position in the EM. Most candidates have a small η value and are situated therefore in the EM barrel part. One can see that nearly all electrons have a negative ϕ, symmetrically distributed around $\pi/2$. This shows that most electrons produced by cosmic muons cross the detector vertically heading towards the lower hemisphere of the Calorimeter. For the background process of muon bremsstrahlung, one would also expect a large fraction of candidates with a positive ϕ as bremsstrahlung photons can also be emitted by the cosmic muons while crossing the upper hemisphere of the EM and be matched to the muon ID track. Unfortunately, a bug occurred during the electron reconstruction in cosmic data: The ID track was not extrapolated towards the top half and no matching was done to clusters located there. For this analysis the bug is of no relevance as the real electrons are expected to point downwards and all candidates with a $\phi > 0$ can be excluded.

In fig. 7.2 and fig. 7.3 (left) the number of TRT, Pixel and SCT hits of all electron candidates is shown. As expected only a small fraction of the events produced hits in the silicon part of the ID. The large fraction of events with no Pixel or SCT hits is not included in the figures. It can be noticed that the number of SCT/Pixel hits is even in most cases. This results from the fact that tracks in cosmic data often cross each layer twice, in the upper and lower hemisphere. On average an electron candidate has about 70 TRT hits, a number which is nearly twice as much as

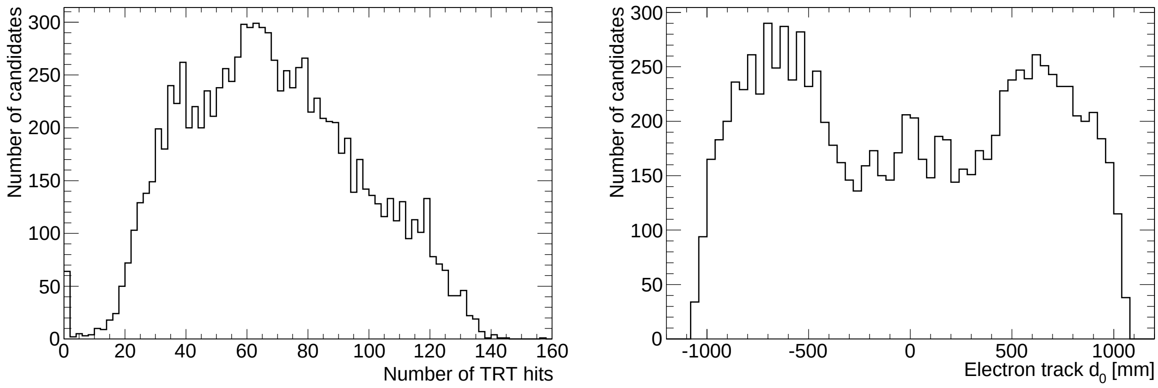

Figure 7.3: Left: Number of TRT hits of all electron candidates. Right: Distribution of their transverse impact parameter d_0.

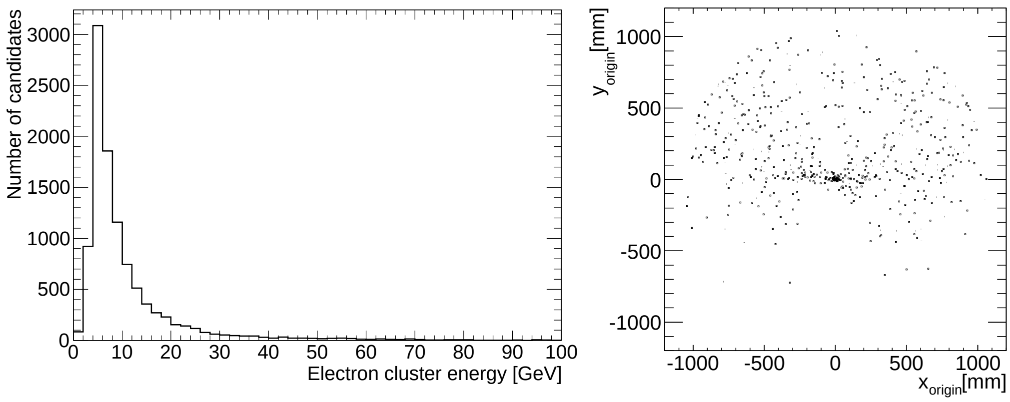

Figure 7.4: Left: Electron cluster energy of all electron candidates. Right: The approximate origin of the electron track in the ID transverse plane is displayed for all events with at least two ID tracks.

expected for electrons from collisions. For electron candidates which have produced only hits in the TRT barrel, no information on the z component or η respectively can be obtained from the track, due to the shape of the straw tubes. The information can only be gained from the cluster position. In fig. 7.3 (right) the distribution of the electron tracks' transverse impact parameter d_0 is shown, one can see that it is distributed over the whole radial extension of the TRT in contrast to collision data. Less tracks are reconstructed in the transition region between TRT and the silicon detectors.

In fig. 7.4 (left) the cluster energy distribution can be seen for all electron candidates. Most candidates feature energies above ca. 3 GeV which is the threshold for the reconstruction with the *egamma* algorithm. In fig. 7.4 (right) the coordinates in the transverse plane of the approximate electron origin are investigated for all events with at least two ID tracks. The exact starting point of an ID track is not available from the data information, the set of track parameters in only available at three space points in the ID for each track, the perigee and two arbitrary points. The space point with the highest y coordinate of the track with the shortest pathlength in the ID is therefore chosen as approximation for the electron origin. The figure reveals that the electron candidates originate nearly exclusively from the upper two thirds of the ID in the transverse plane as they have to cross a certain distance in the ID to be reconstructed.

7.1.1 Creation of a signal and a background sample

To isolate delta electrons from ionization processes which are the predicted main source of electrons in cosmic data, the special signature of this process is used as a first step. Its signature in the detector features, besides the electron shower, two tracks in the ID and two muon candidates in the upper and lower half of the detector. In contrast, an event with a fake electron candidate produced by muon bremsstrahlung in most cases consists of one track in the ID and two muon candidates. The different constellation frequencies of muon and track numbers in the data sample are investigated in fig. 7.5.

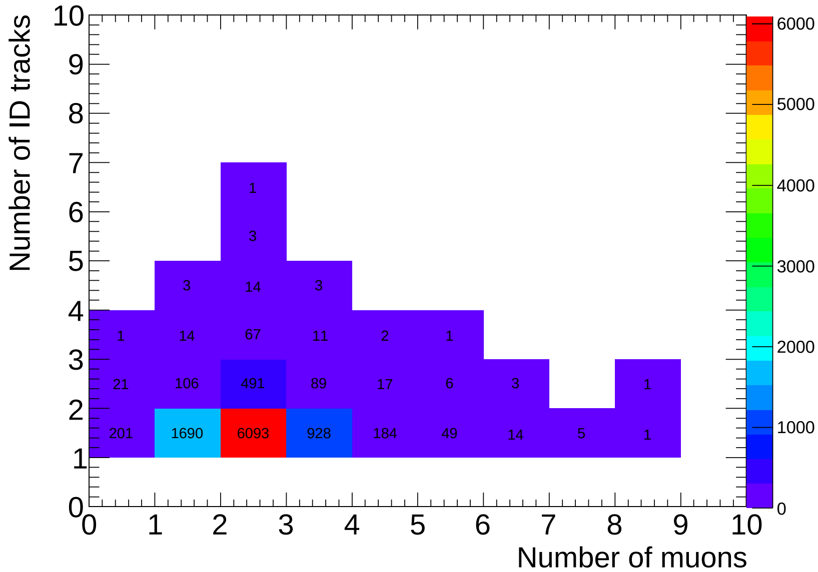

Figure 7.5: Number of reconstructed tracks versus number of muon candidates for all events with exactly one electron candidate

The largest number of events features one ID track and two muon candidates. This is the expected signature of the muon bremsstrahlung background which has obviously the largest contribution to the electron candidates. The number of events with two ID tracks and two muon candidates is more than one order of magnitude smaller, but still a large number of events has exactly this signature expected for the signal delta electrons. Also a large fraction of events with only one reconstructed muon candidate exists. These are most probably events where one muon was not reconstructed in the MS. Also, a small amount of electrons from muon decays in flight might be contained in the events with one track and one muon candidate. The investigation of this event signature in order to find electrons from decay is presented in appendix A.

In order to separate the events with the delta electron signature from the large muon bremsstrahlung background, two subsamples of the initial cosmic data sample are formed. One subsample only contains candidates which fulfil the following cuts:

- two or more ID tracks
- one electron candidate in the bottom half of the detector (with $\phi < 0$)

- one or more muon candidates; if the number of muons is $\geq$2, of the two candidates with the highest momentum one is required to be in the top half ($\phi > 0$) of the detector and the second one in the bottom half ($\phi < 0$) and both are required to have opposite charge.

After these cuts, a significant fraction of events in this sample are expected contain electrons from ionization processes, therefore it will be referred to as *signal* or *ionization sample.* Also several events with electrons from bremsstrahlung-photon conversions might be contained where the second candidate of the produced pair was not reconstructed. In addition, this sample probably also consists of a fraction of fake electron candidates produced by bremsstrahlung-photons which did not convert and where an additional second fake track has been reconstructed. Several electron identification cuts need to be applied to reject this background which will be explained in the next section.

The second subsample is required to contain mainly background events, fake electron candidates produced by muon bremsstrahlung where a photon showered in the EM and the resulting cluster is matched to the muon track. The events in this control *background* or *bremsstrahlung sample* are required to have:

- exactly one ID track
- one electron candidate in the bottom half of the detector (with $\phi < 0$)
- one or more muon candidates

Events with more than one electron candidate are neglected, as none of these events survive all the cuts (see next section), and they are therefore most probably incorrectly reconstructed background events.

The samples are restricted to electron candidates in the bottom half of the detector ($\phi < 0$) as this is the expected direction of real electron candidates produced in the ID. Concerning the background events, this restriction in addition excludes the detector area where the bug in the electron reconstruction occurred and affected the statistics as explained above in this section.

The events which do not fit in one of the categories defined above are neglected for the analysis because a clear signal or background classification cannot be made.

7.1.2 Cut selection for the identification of electrons

In order to isolate the real electrons and to reject the background of muon bremsstrahlung in the two subsamples, the identification cut selection *IsEM* commonly used in ATLAS is applied which makes use of the typical properties of electron track and shower shapes. The cuts are explained in detail in sec. 4.4. They are divided into three categories: loose, medium and tight. In this order the cut sets increase in the number of applied cuts and at the same time in rejection of background. Since this cut selection was developed and optimized for collision events, several modifications have to be made in order to apply it to the cosmic data samples. No change of the cuts themselves is made but several cuts are omitted and the placement within the three categories is changed in some cases. The cuts vary slightly with η and the transverse energy E_T because the length of the trajectories in the ID and the granularity of the EM layers varies slightly with η and the cluster reconstruction and calibration is η and energy dependent.

In the following the exact loose, medium and tight cut selections applied to the electron candidates in the two subsamples in cosmic data are listed. In addition, the explicit cut thresholds for $|\eta| < 0.8$ and $E_T < 7.5$ GeV are indicated - unless stated otherwise - since this is the range in which the largest fraction of electron candidates can be found (see plots 7.4 and 7.1). The full list of applied cut thresholds for all η and E_T regions can be found in [54].

The loose electron identification cuts make use of the electron shower properties in the second layer of the EM and the information from the Hadronic Calorimeter. As the Calorimeters can provide detailed information on the shower shape only for $|\eta| < 2.47$, all candidates with an $|\eta|$ larger than this value are cut away. The loose cuts applied to the cosmic data samples are the same as in the standard selection for collision data:

- Hadronic leakage ($\frac{E_{\mathrm{T}}^{had}}{E_{\mathrm{T}}} < 0.025$)
- Ratio of energy deposited within a window of 3x7 cells over a window 7x7 cells in the 2nd EM sampling (Reta= $e237/e277 > 0.750$, with $e277 > 0$)
- Lateral shower width (Weta2 < 0.0150)

The second applied cut selection are the medium cuts. Of this cut set, several cuts need to be omitted due to the special topology of cosmic data and some are moved from the standard tight to the medium set. The medium cuts make use of the fine granularity η information of the first EM layer to account for the small shower width of electrons and the early start of the shower, in contrast to bremsstrahlung photons for instance which are emitted by the muon at a later point in the EM. Further cuts of the standard selection on the number of track hits in the Pixel or SCT detector and a restriction of the transverse impact parameter cannot be applied to electron candidates from cosmic data due to their different topology: Many events only cross the TRT at an arbitrary distance with respect to the detector origin and have no silicon hits, as explained and shown above in this section. Applying these cuts would reduce the statistics of the signal candidate sample too much. Instead, the cut on the number of TRT hits part of the standard tight selection is applied already in the medium cut set. In addition a good match of cluster and track is required in the ϕ direction. This should further reduce the background of bremsstrahlung photons loosely matched to the muon track during reconstruction. The same cut in η direction cannot be applied to the electrons from cosmic data, as the majority of the tracks in the sample have TRT-only hits which provide only axial track-hit information. In summary, the applied medium cuts modified for the cosmic events are besides the loose cuts:

- Fraction of total cluster energy deposited in first EM sampling (F1 > 0.005[24])
- Fraction of energy in the strip with the second largest energy deposition (Rmax2 < 0.25)
- Energy difference between strip with the second largest energy deposition and the strip with minimal energy in between the two strips with the highest energy deposition (DeltaE2 < 0.15 GeV)
- Total shower width in first EM sampling (Wtot< 4.00)
- Difference of energy summed over $\pm$ 3 strips and ± 1 strips around maximum divided by energy in ± 1 strips (Fside < 0.6)
- Lateral core shower width in three strips around the maximum (Weta1 < 0.80)
- Number of TRT hits (The minimal requirement for $\eta < 0.1$ is at least 19 hits)

[24] This cut is only applied here to ensure that a minimal fraction of energy has been deposited in the first EM layer.

- Difference between track ϕ extrapolated to EM and cluster ϕ position ($\Delta\phi < 0.02$)

For the final tight selection applied to the cosmic data samples, the two most important variables for a separation of the real electrons and the background of muon bremsstrahlung are included additionally to the medium cuts: The matching of cluster energy and track momentum which is expected to be approximately one for the real electrons and much smaller for the fake bremsstrahlung events and the fraction of transition radiation hits in the TRT which should be large for electrons and small for muon bremsstrahlung events of not too high energies. These cuts are explained in detail in sec. 4.4. The tight electron identification cut set applied to the cosmic data samples is therefore:

- Ratio of cluster energy over track momentum ($0.8 < E/p < 2.5$)
- Ratio of high to low-threshold TRT hits (The minimal cut value for $\eta < 0.1$ is HT-TRT ratio > 0.08, for $\eta < 0.625$ it is HT-TRT ratio > 0.085)

7.1.3 Results from data

The resulting numbers of events for the total data sample after the separation into a signal (ionization) and background (bremsstrahlung) sample and after the application of the individual cuts and the cut sets (loose, modified medium and modified tight), can be seen in table 7.2.

Cut Set	Single Cuts	Ion. sample	Brem. sample	All
All cand.		**608**	**8903**	**10421**
	Had. leak.	324	4236	4977
	Reta	301	4112	4804
Loose	Weta2	**266**	**3743**	**4348**
	F1	266	3743	4348
	Rmax2	236	3596	4153
	DeltaE2	234	3595	4150
	Wtot	179	2665	3092
	Fside	119	2199	2528
	Weta1	119	2198	2527
	TRT hits	118	2192	2519
Mod. Medium	$\Delta\phi$	**81**	**1147**	**1326**
	E/p	44	46	103
Mod. Tight	HT-TRT ratio	**34**	**13**	**54**

Table 7.2: Event numbers after application of modified IsEM cuts for all electron candidates before and after separation into two subsamples

The number of all reconstructed electron candidates in the bremsstrahlung sample initially is more than one order of magnitude larger than the number of candidates which are contained in the ionization sample. The application of all identification cuts reduces the number of events in the one-track bremsstrahlung sample to a very large extent, about 3 orders of magnitude. At the end of 8903 only 13 events remain (0.1%). For the ionization sample in contrast a much larger fraction of events remain after the modified tight cuts - 34 of 608 initially reconstructed candidates (5.6%). The hypothesis that the two-track ionization sample primarily contains the real electron candidates in contrast to the one-track sample which consists nearly exclusively

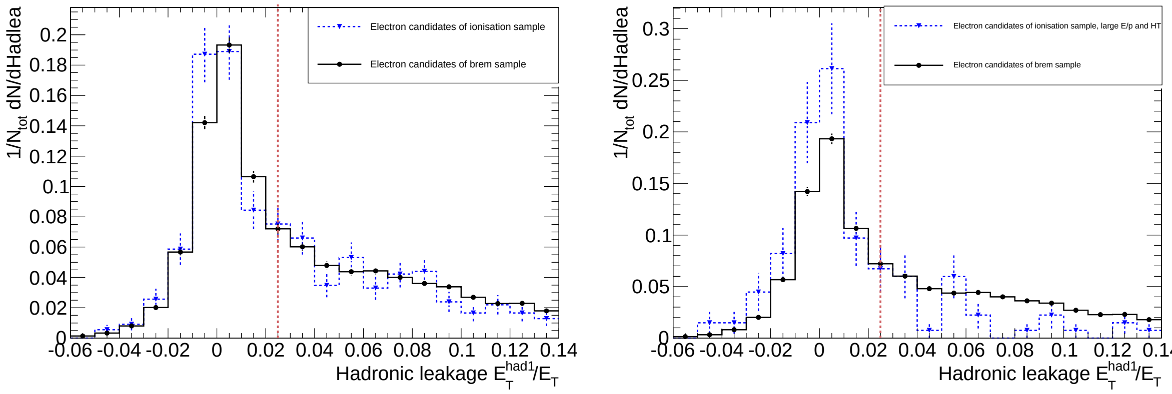

Figure 7.6: Left: Distribution of the hadronic leakage compared for the ionization (blue dashed line) and bremsstrahlung (black solid line) sample. The red line indicates a typical cut applied to events with a small η and E_T value. Right: The same distribution shown for events with E/p>0.8 and HT-TRT ratio>0.08 in the ionization sample and for all events in the bremsstrahlung sample.

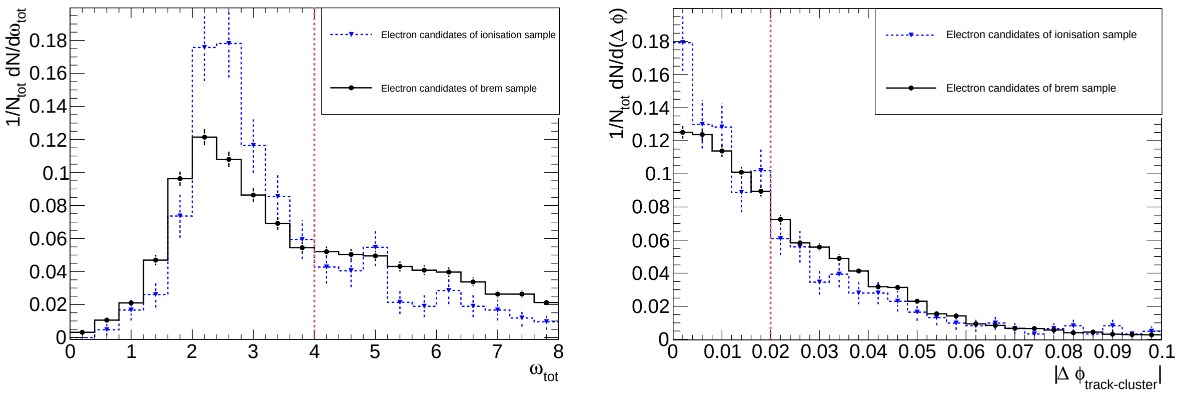

Figure 7.7: Distribution of the total shower width Wtot in the first EM layer in units of Calorimeter strips (left) and the absolute difference in ϕ between the electron cluster position and the track direction extrapolated to the EM (right). Comparison of the ionization (blue dashed line) and bremsstrahlung (black solid line) sample. The red line indicates a typical cut applied to events with a small η and E_T value.

of background, is therefore strengthened. The 34 candidates which remain after all cuts are regarded as the final electron candidates. The primary production process for these electrons is ionization which leads exactly to the signature in the detecor which is selected for the final candidates.

Among the final candidates there are 30 electrons and four positrons. In ionization processes only negatively charged electron candidates can occur. The positrons therefore originate either from a conversion of a bremsstrahlung photon in which the negatively charged partner of the positron has not been reconstructed, they could be a background event produced by muon bremsstrahlung where an additional second track was accidentally reconstructed or the charge of the electron could be mismeasured. A clear assignment to one of these event categories cannot be made with the given information for these events, see also discussion of the individual event displays for the positron candidates in appendix B.

The comparison of the number of events after the individual cuts reveals that some cuts reduce the number of events more strongly than others which have only little influence. The requirement on a minimal fraction of energy left in the first sampling of the EM is fulfilled by all loose electron candidates and the numbers are not reduced by this cut.

The distribution of the hadronic leakage variable which halves the number of events of both samples is shown in fig. 7.6 (left) for all events of the bremsstrahlung sample and the ionization sample. It can be noticed that numerous candidates of both samples deposited a large fraction of energy inside the first layer of the HCal. This is untypical for real electrons, they deposit nearly their entire energy in the EM. This means that in the bremsstrahlung and ionization sample there is still a large fraction of background events from muon bremsstrahlung which is reduced by this cut. For the ionization sample a small excess of events can be observed in comparison to the bremsstrahlung sample at lower values of the hadronic leakage. To strengthen the assumption that this might come from real electrons in this sample the same distribution is shown in the case of the ionization sample only for events with a large E/p (>0.8) and HT-TRT ratio (>0.08), consistent with the modified tight cuts, in fig. 7.6 (right). Indeed, a larger fraction of these events accumulate at small values of hadronic leakage in comparison to the bremsstrahlung sample as expected.

The distribution of the total shower width in the first EM layer (wtot) and the difference in ϕ between the cluster position and the extrapolated track have been investigated for both subsamples in fig. 7.7. Also in this case, an excess of events of the ionization sample in comparison to the background sample can be observed at lower values which is expected for the real electron candidates with a small shower width and an good matching between track and cluster.

The observed numbers of events after the individual cuts in table 7.2 indicate that two variables dominantly contribute to the discrimination between signal and background candidates:

- The ratio of high to low-threshold hits in the Transition Radiation Tracker (HT-TRT ratio)
- The ratio of the EM cluster energy over the track momentum (E/p)

They reduce the number of events after the modified medium cuts strongly in the bremsstrahlung sample, while for the ionization sample a much smaller fraction of events does not pass the cuts. In order to confirm the isolation of real electrons after the application of all cuts, the distributions for these two variables are investigated in detail comparing the two subsamples with electron candidates of cosmic data.

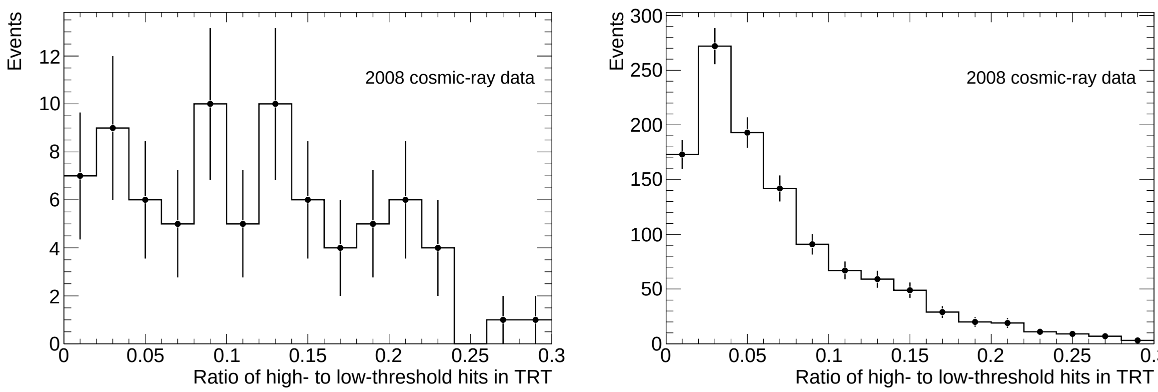

Figure 7.8: The distribution of the ratio of high to low-threshold TRT hits for all events which survived the modified medium cuts for the ionization sample (left) and the bremsstrahlung sample (right).

The distribution of the ratio of high to low-threshold TRT hits for the 81 events of the ionization sample which remain after the modified medium cuts can be seen in fig. 7.8 (left).

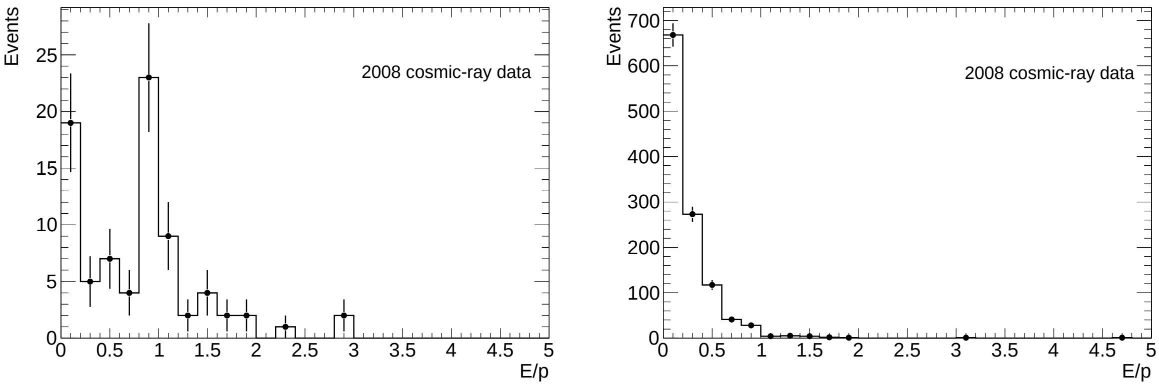

Figure 7.9: The distribution of the ratio of Calorimeter cluster energy and track momentum for all events which survived the modified medium cuts, for the ionization sample (left) and the bremsstrahlung sample (right).

The energy over momentum distribution for the same events can be seen in fig. 7.9 (left). In comparison the same distributions can be seen for the 1147 events which remain in the muon bremsstrahlung sample after the modified medium cuts in fig. 7.8 (right) and 7.9 (right). The difference in the distributions for the two subsamples can clearly be seen: In the background sample there is no rise at higher values in the case of both of these variables, most events have a rather small E/p and HT-TRT ratio value, as expected (see section 4.4). In contrast to that, in the signal sample a clear accumulation of events around one can be seen in the E/p distribution which is expected for real electrons. Also in the distribution of the ratio of high to low-threshold hits in the TRT there is a large fraction of events with higher values in the case of the ionization sample. Nevertheless, muons with energies above 100 GeV might also produce tracks with a large fraction of transition radiation hits. Therefore, the two-dimensional distribution of these variables is studied as well. The distribution of the high to low-threshold TRT hits versus the energy over momentum is shown for both samples in fig. 7.10 and fig. 7.11. In the bremsstrahlung sample most of the events lie below the cut thresholds and only a small fraction of events survive the modified tight cuts which is expected for background events. In contrast, in the ionization sample a large fraction of the events passes the tight cuts. This signal is therefore a clear evidence that real electrons are extracted by these cuts.

It should be noted that several events of the bremsstrahlung sample have a high HT-TRT ratio but a low E/p value. These are probably high-energy muons which emitted transition radiation. To prove this, the incoming muon momentum spectrum of all modified medium events in the bremsstrahlung sample with $E/p < 0.8$ is compared for events with HT-TRT ratio < 0.08 and HT-TRT ratio > 0.08. This is depicted in fig. 7.12. As expected, the events with a high HT-TRT ratio have a larger tail towards muon momenta above 100 GeV, while the events with low HT-TRT ratio feature in comparison much lower muon momenta.

As observed in the bremsstrahlung sample which is assumed to contain only background events, several (13) candidates also survive the tight cuts. This means, the electron candidates of the ionization sample which remain after the modified tight cuts are also not purely real electrons but a small fraction of background events is most likely still contained. A description of a method to estimate the remaining number of background events will be explained in sec. 7.2. In the next section the 34 final electron and positron candidates which remain in the ionization sample after all cuts, are investigated in detail.

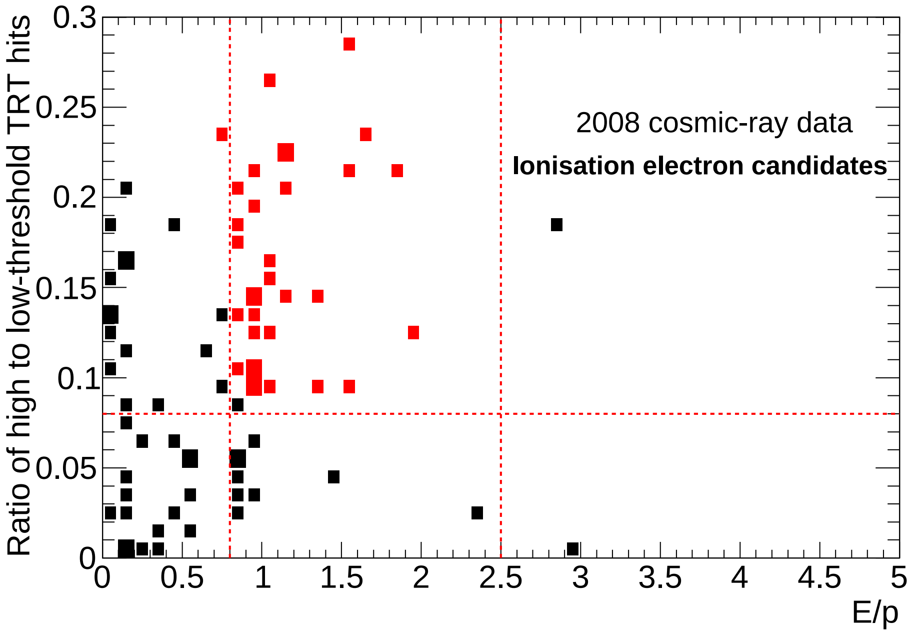

Figure 7.10: Two-dimensional distribution of the ratio of high to low-threshold TRT hits vs. E/p for the ionization sample. The black boxes show all electron candidates which survived the modified medium cuts. The red boxes mark the electron candidates which in addition survived the modified tight cuts. The orange lines show the cuts applied to most of the events at $\eta \approx 0$ and $E_T < 7.5$ GeV, $0.8 <$ E/p < 2.5 and HT-TRT ratio > 0.08. Since these cuts vary slightly with η and the transverse energy, a few events lie at the borders of this nominal region and are attributed to the other category. Two outliers at high HT-TRT ratio (1 in signal, 1 in background region), and one outlier at high E/p are not included.

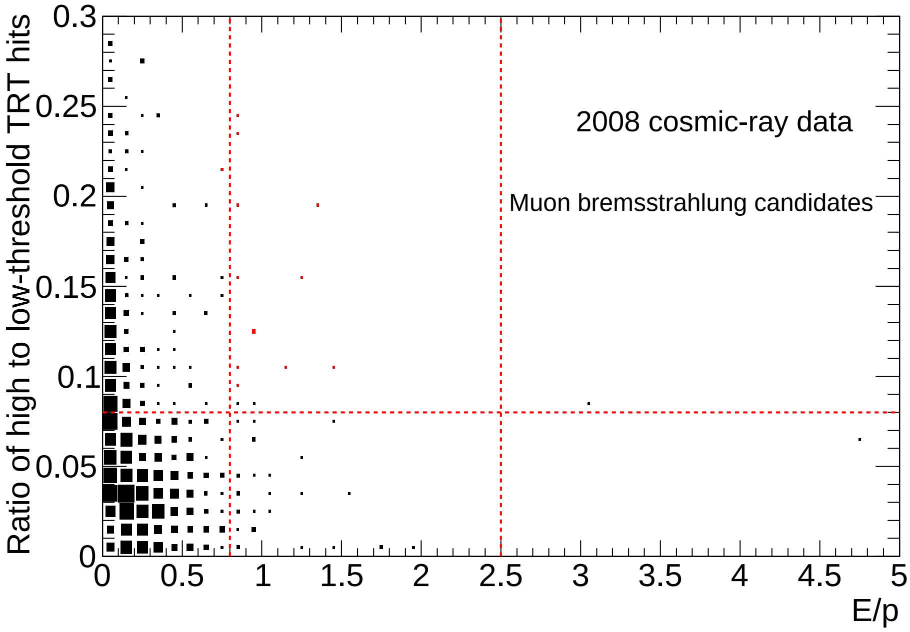

Figure 7.11: Same distribution as in fig. 7.10 shown for the bremsstrahlung sample.(A few outliers at a high HT-TRT ratio and 2 outliers at a high E/p value are not included.)

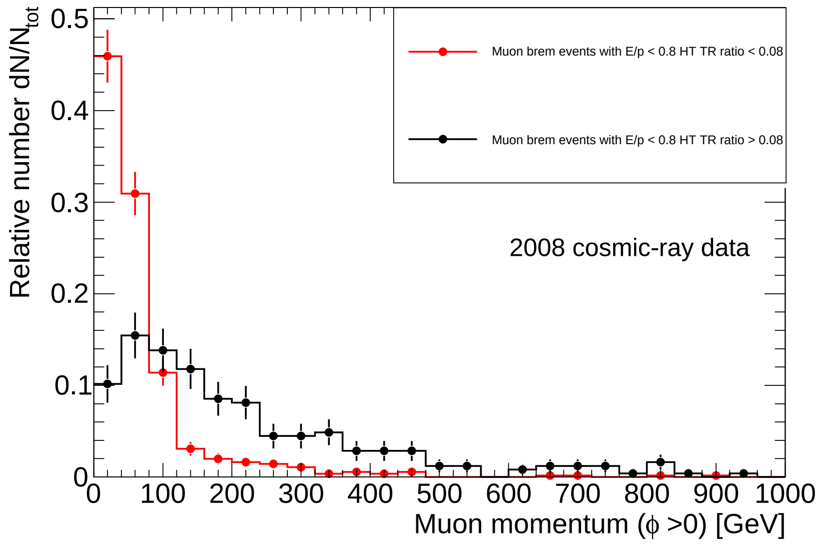

Figure 7.12: The distribution of the momentum of the incoming muon candidate ($\phi > 0$) is shown for all events of the bremsstrahlung sample after the modified medium cuts with $E/p < 0.8$, for HT-TRT ratio < 0.08 in red and for HT-TRT ratio > 0.08 in black.

Investigation of final candidate properties

In fig. 7.13 (left) the spectrum of the electron cluster energy is shown for all 34 final electron and positron candidates which remain after the identification cuts. It can be seen that the distribution peaks at around 5 GeV. This can be explained by the fact that the cluster-finding algorithm for electron reconstruction has a decreasing efficiency for electrons just above the threshold of $E_T > 3$ GeV [55]. The decrease of the distribution at higher energies is a consequence of the decreasing probability for knock-on (and conversion) electrons with higher energies (see sec. 6). Three events, which are not displayed in the distribution, have energies above 50 GeV which is very unlikely for electrons produced by these processes. This means that these events rather are background events of muon bremsstrahlung or the reconstruction of the electron energy has been erroneous. In fig. 7.13 (right) the $|\eta|$ distribution for the final electron candidates is investigated. It can be seen that most of the events have an absolute η value smaller than one. This means that all clusters lie within the EM barrel.

Also the momentum spectrum of the reconstructed muons with the highest momentum is investigated for all final electron events featuring at least two reconstructed muon candidates (25 events). In fig. 7.14 the spectrum is illustrated for the incoming muon ($\phi > 0$, left) and outgoing muon ($\phi < 0$, right). Most muons have a momentum smaller than 50 GeV. The rest of events contains only one muon candidate where either the upper or lower candidate of the cosmic muon has not been reconstructed.

In fig. 7.15 (left) the difference of the incoming and outgoing muon momenta is plotted versus the electron cluster energy for all final candidates with two reconstructed muon candidates. The outliers with higher and negative momentum differences indicate that the reconstruction of cosmic muon candidates is not correct in all cases. This might result from their different topology in comparison with collision data for which the reconstruction algorithms are optimized. In most other cases nevertheless the difference in momentum for the muons roughly agrees with the electron energy which shows the balance of the energy or momentum values in the detector

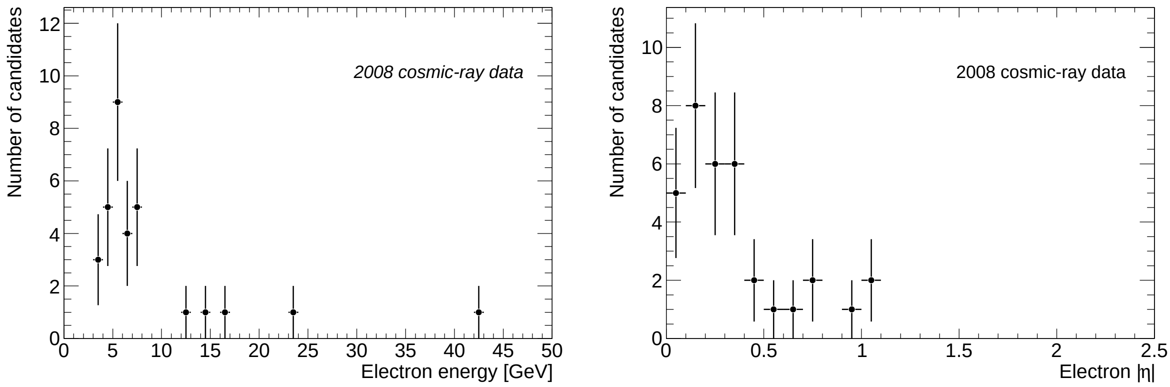

Figure 7.13: Left: The cluster energy spectrum for all 34 final candidates which remain after the modified tight cuts. Three events have energies above 50 GeV and are not shown here. Right: Distribution of the absolute value of η for all final electron candidates.

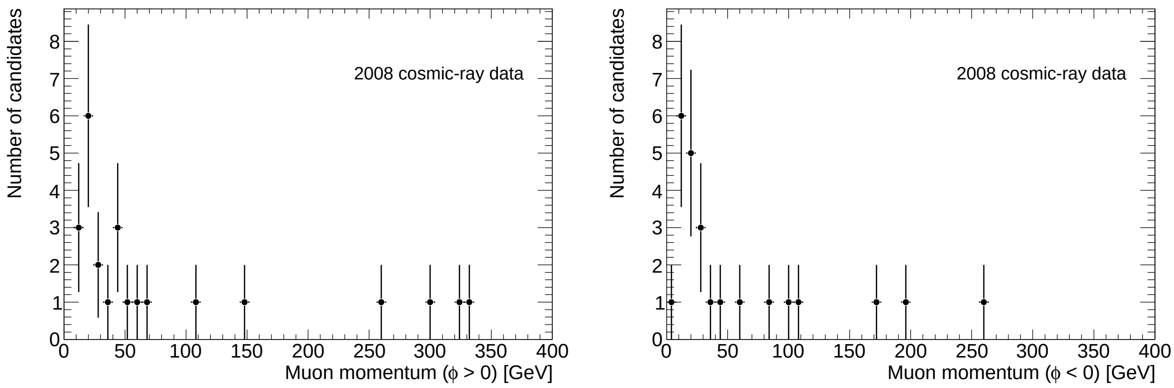

Figure 7.14: Left: Momentum spectrum of the incoming muon (ϕ >0). Right: Momentum of the outgoing muon (ϕ <0). Shown are all 25 final electron events which feature two muon candidates. (One outlier in each case is not included.)

and proves again that the assumption of the event topology is reasonable. In addition, the energy balance of the difference of the incoming muon momentum ($\phi < 0$), the momentum of the outgoing muon ($\phi < 0$) and the electron cluster energy is investigated dependent on the incoming muon momentum ($\phi > 0$) in fig. 7.15 (right). This balance is expected to be zero on average if the muons lose energy in the ID by creating an electron, and all other energy losses in the detector can be neglected. This applies to most events especially in the lower muon momentum region.

In fig. 7.16 the approximate origin of the electron ID track is investigated for all final candidates in the same way as described at the beginning of this section. As expected most electron candidates originate from the upper two thirds of the ID, since they have to cross a minimal distance in the ID to be reconstructed.

The delta (or conversion) electrons are in most cases emitted in forward direction, and muon and electron track should be very close-by in the Inner Detector (see sec. 6). Therefore, the angular distance of the two reconstructed ID tracks is investigated for the electron events of the ionization sample. As most tracks of cosmic data feature no silicon hits and provide only azimuthal angular information, only the $\Delta\phi$ between the two highest p_T ID tracks can be de-

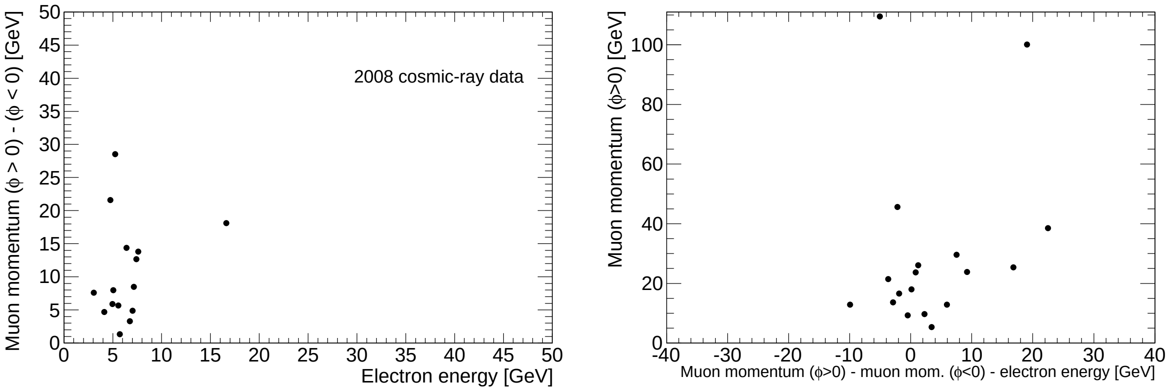

Figure 7.15: Left: Zoomed view of the momentum difference between the incoming and outgoing muon vs. the electron cluster energy. Several high energy events are in the histogram's overflow and several are in the underflow with a negative muon momentum difference. Right: Energy balance of the final electron events with two muon candidates. Shown is the momentum of the incoming muon ($\phi > 0$) vs. the difference of incoming and outgoing muon candidates minus the electron cluster energy.

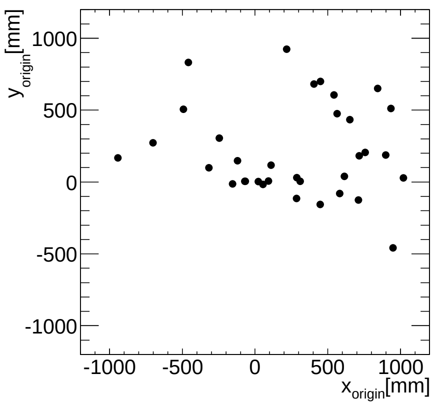

Figure 7.16: The approximate origin of electron track in ID transverse plane of all final candidates.

termined for all events. Since the electron production point cannot be exactly determined from data, the ϕ direction of the electron ID track is evaluated at the available track space point with the largest y coordinate. The ϕ direction of the second ID track is extracted at the track point with the minimal distance to the initial point of the other track. The difference in ϕ of the track directions at these points is shown in fig. 7.17 for the final electron candidates and in comparison also for all candidates in the ionization sample. Of course this is only an approximation of the true angle between the two ID tracks at the electron production point because the track direction changes permanently due to the deflection inside the magnetic field.

As a comparison both ID tracks have also been extrapolated to their entrance point to the first EM layer in the lower detector hemisphere, and the difference in their ϕ direction has been determined at this point. The $\Delta\phi$ is on average larger at this point since the tracks have already been bent in their trajectories by the solenoid field, as can be seen in fig. 7.18. These plots show that after the modified tight cut selection nearly exclusively events with a smaller angular difference between the muon and electron ID track remain, as it is excepted for delta (or conversion) electrons (or positrons).

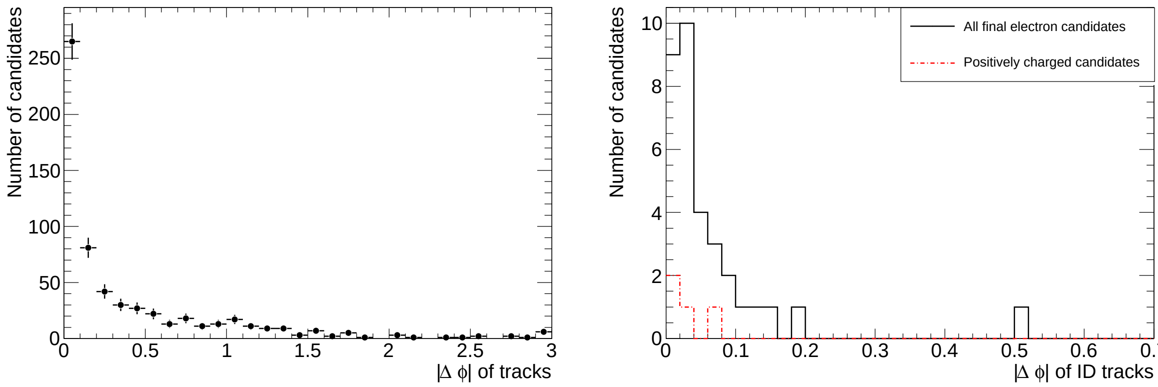

Figure 7.17: The absolute value of the difference in ϕ of the two highest p_T tracks in the ID is displayed. The ϕ directions are evaluated at the track space points closest to the electron origin. Left: The distribution for all electron candidates in the ionization sample. Right: The distribution for the final electron candidates, the four positively charged candidates among them are marked in red. One outlier in the overflow is not included.

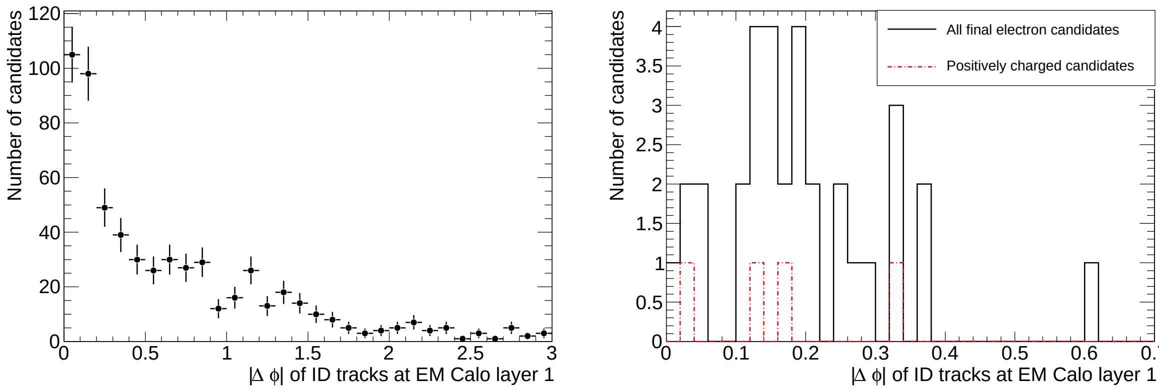

Figure 7.18: The absolute value of the difference in ϕ of the two highest p_T tracks in the ID calculated at the point at which the tracks enter the first EM layer. Left: The distribution for all candidates in the ionization sample. Right: The distribution for the final electron candidates, positively charged candidates among them are marked in red. One outlier in the overflow is not included (same event as in fig. 7.17).

To get a visual impression of the delta electron events, they are investigated by using the event display software *Vp1*. An example for an electron candidate produced in an ionization process by a cosmic muon is shown in fig. 7.19, including a zoomed view.

The full view shows clearly the incoming and outgoing muon tracks in orange, at the top measured in three muon stations, in the middle in the Inner Detector and at the bottom in two muon stations. The electron track and cluster and EM cells with energy depositions can be seen in green. The zoomed plot shows the Inner Detector, and the hits in TRT, SCT and Pixel detector are displayed as blue and green dots for both tracks. The red dots in the TRT indicate the high threshold hits caused by transition radiation. It can clearly be seen that the electron has produced much more of these high threshold hits.

In light green the energy deposited in the cells of the presampler, first and second EM layer by the electron is visible, and in dark green the reconstructed electron cluster built from the cells

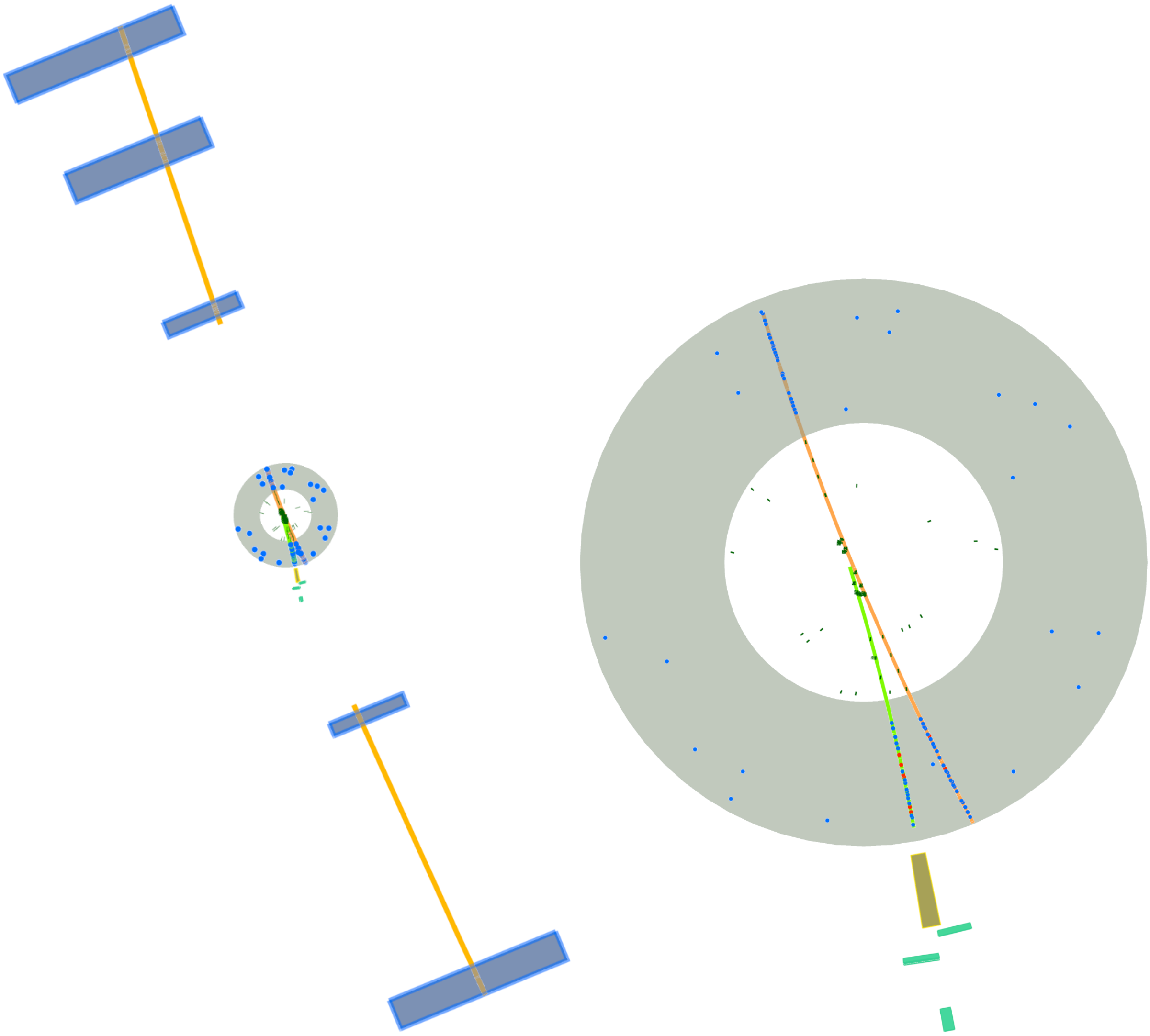

Figure 7.19: Event display of a typical delta electron event (run 90275, event 375468) in full (left) and zoomed (right) view. The track of the muon in orange and the electron track and matched cluster and reconstructed cells in green can be seen clearly. (Details see text).

can be seen[25]. Threshold cuts have been applied to the cell energies and track hits in order to have a clear display of the event.

Since the exact classification of the modified tight positron candidates is disputable, the individual investigation of all four event displays can be found in Appendix B. A short investigation of the level-1 trigger functionality for the final electron and bremsstrahlung candidates is provided in appendix C.

The investigations of the final candidate properties confirm that real electrons mainly from ionization have been isolated by the cut selection and that the assumptions about the event topology are reasonable.

[25] Only the position of the cluster's barycenter is relevant for cosmic events since the direction of the cluster is assumed to point to the detector origin by the reconstruction algorithms (see sec. 4.3.1).

7.2 Background estimation

Since the sample of the final electron candidates is not expected to consist purely of signal events, an estimation of the number of remaining background events needs to be done. Given the small statistics of the sample, a method needs to be implemented which nevertheless yields a reasonable result. Best suited for this is a binned maximum likelihood fit performed on the background region of the two-dimensional HT-TRT ratio vs. E/p distribution.

The probability that a particular set of data, in this case the number of observed events in each bin $N_1, N_2, ...N_N$, results from the value a of one (or more) unknown parameters is given by the likelihood function. This is the product of the individual probabilities for each observation $L(N_1, N_2, ...N_N; a) = \prod P(N_i; a)$, [56]. The principle of maximum likelihood is a method to estimate the values of the unknown parameters that maximize the likelihood function. In this case these parameters are part of a function which describes the expected number of events in each bin. The maximization of the likelihood function is the most adequate method to estimate the parameters in the case of small statistics in which also empty bins need to be included for the estimation. The probability density for each bin is then described by a Poisson distribution.

The two-dimensional E/p and HT-TRT ratio distribution for the modified medium and tight events of the ionization and bremsstrahlung sample (see fig. 7.10 and 7.11) is the basis for the estimation of the background distribution among the final electron candidates. Two different background categories need to be distinguished here. The bremsstrahlung sample consists of events with only one ID track which are all assumed to be background events. The ionization sample consisting of events with at least two ID tracks contains on the one hand the signal electron events which survive the modified tight cuts. On the other hand, it contains the events which do not survive the cuts which are also assumed to be background from muon-bremsstrahlung with a wrongly reconstructed second track. The one-track and two-track background are in the following assumed to have the same shape. In order to find a suitable fit parametrization for the shape of the background in the two samples, the bremsstrahlung sample with larger statistics is used. The fit with this parametrization is then performed on the ionization sample. Since no exact signal peak for the HT-TRT ratio distribution can be found and the expected width for the E/p peak is not known, no fit on the shape of the signal electron events is done. Instead the background in this ionization sample is fitted excluding a rectangular signal region in which most of the modified tight electrons and positrons lie. The borders of this region (lines in fig. 7.10) are the tight cuts for the bulk of electron candidates 0.8 < E/p <2.5 and HT-TRT ratio > 0.08. As explained in sec. 7.1.2 these cuts vary slightly with η and the transverse energy. As a consequence a few events lie at the borders of this nominal region and are attributed to the other category, e.g. a signal event lies in the background region or vice versa. To account for this a three or four dimensional fit would be most accurate. Since the influence of this is rather small, the effect is neglected here. The number of background events among the final modified tight electron candidates is obtained by evaluating and integrating the fitted background function over the signal region in the ionization sample.

The E/p background distribution is parametrized by an exponential function $f(x) = e^{-a_1 \cdot x}$ with x=E/p, while the HT-TRT ratio distribution is described by $f(y) = y \cdot e^{-a_2 \cdot y}$ with y denoting the HT-TRT ratio. The complete two-dimensional background function is the product of the two one-dimensional functions with an additional global normalization parameter a_0:

$$f(x, y) = a_0 \cdot a_1 \cdot (a_2)^2 \cdot e^{-a_1 \cdot x} \cdot y \cdot e^{-a_2 \cdot y} \tag{7.1}$$

In total the number of parameters is therefore three. The normalization of the fit-function

has been chosen in a way that the integral of the fit function is independent of a_1 and a_2 which reduces the correlations between the parameters. Several attempts have been made to increase the number fit parameters in order to get a more accurate approximation of the E/p and HT-TRT ratio distribution. No reasonable fit result could be obtained. Therefore, the number of fit parameters is kept at three.
The number of expected events per bin is calculated as:

$$N_{\text{exp}}(\text{bin}) = f(x_i, y_i) \cdot binw_x \cdot binw_y \tag{7.2}$$

The variable $binw_x = 0.1$ is the bin width of the E/p variable and $binw_y = 0.01$ denoted the bin width of the HT-TRT ratio. The variables x_i and y_i represent the values of the respective variable at the ith bin center. By this approach it is assumed that the function is constant over the total bin width. As the bin width is small this adds only a negligible contribution to the error on the fit. The likelihood function which needs to be maximized, is therefore given by the product of the Poisson probabilities for the individual bins.

$$L(a_0, a_1, a_2) = \prod_{\text{bins}} \frac{(N_{\text{exp}}\,(\text{bin}))^{N_{\text{obs}}(\text{bin})}}{N_{\text{obs}}\,(\text{bin})!} \cdot e^{-N_{\text{exp}}(bin)} \tag{7.3}$$

Here N_{obs} denotes the number of observed events per bin in the two-dimensional histogram and N_{exp} denotes the estimated number of events in this bin obtained from the resulting fit function. As a tool for the determination of the fit result, the Minuit interface of the ROOT software is used. With it the negative value of the logarithmic likelihood function is minimized.

The function is verified to be appropriate for the background description by minimizing the negative logarithmic likelihood function for the bremsstrahlung background-only sample.

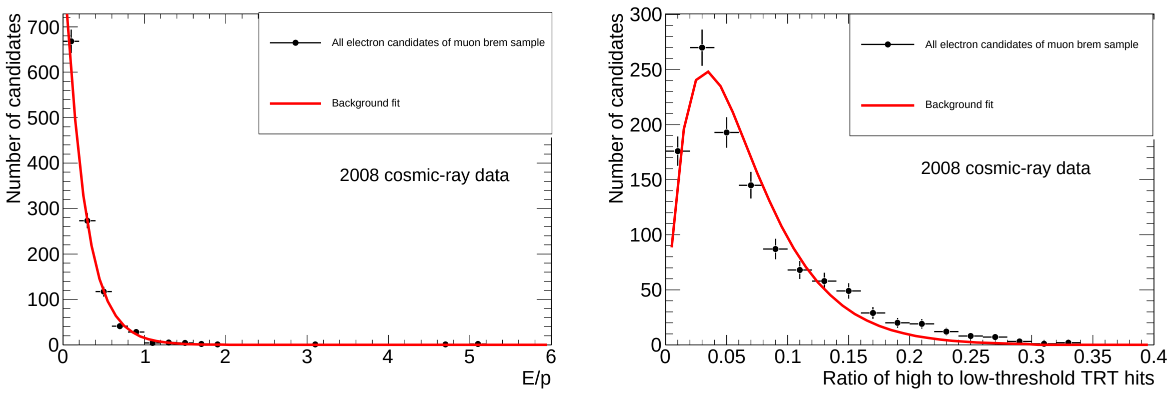

Figure 7.20: Distribution of the E/p (left) and HT-TRT ratio (right) distribution of the events in the bremsstrahlung sample after the modified medium cuts. The red curve shows the respective projection of the two-dimensional binned maximum likelihood background fit which was performed on this sample for E/p $<$ 5 and HT-TRT ratio $<$ 0.2.

The projection of the obtained fit function to the two distributions, E/p and HT-TRT ratio can be seen in fig. 7.20 together with the distribution of the modified medium events of the bremsstrahlung sample. One can see that the fit-function and the respective distribution agree fairly well.

The background function is now fitted to the two-dimensional distribution of HT-TRT ratio vs. E/p for the ionization sample excluding the signal region (0.8 $<$ E/p $<$ 2.5 and 0.08 $<$ HT-TRT ratio). The signal modified tight events outside this region are excluded individually from the fit. All other histogram bins outside the signal region are considered. The upper borders of the histogram used for the fit have been chosen to include all modified medium events. The negative value of the logarithmic likelihood function is then minimized by using Minuit. The result for the fit parameters of the background events in the ionization sample is:

$$\begin{aligned} a_0 &= 54.29 \pm 11.60 \\ a_1 &= 1.27 \pm 0.27 \\ a_2 &= 21.87 \pm 3.47 \end{aligned} \tag{7.4}$$

All parameters are dimensionless. The correlation coefficients of these parameters are $c_{01} = -0.155$, $c_{02} = -0.175$ and $c_{12} = 0.133$. The resulting fit function is then evaluated in the signal region and integrated over the whole region to gain the estimation of the number of background events among the final electron and positron candidates. The (statistical) error on the number of background events is calculated by taking into account the errors and correlations of the three fit parameters. As a result it is obtained for the number of background events in the signal region of the ionization sample:

$$N_{\text{backgr}} = 8.3 \pm 3.0 \tag{7.5}$$

In fig. 7.21 and 7.22 the projection of the two-dimensional maximum likelihood fit result can be seen together with the respective distribution of the E/p and HT-TRT ratio. The HT-TRT ratio distribution is shown for the events of the ionization sample after the modified medium cuts, also displayed are the 47 background events on which the fit was performed. The remaining background events in the signal region can be seen as the difference between the fit curve and the distribution of the background events. The E/p distribution is shown for all modified medium events to which in addition the tight-selection cut on the HT-TRT ratio was applied. The area beneath the fit curve inside the signal region therefore depicts the number of background events in this region. It should be noted that for display purposes both projections use a different binning than was used for the fit as explained above.

With this background estimation the number of signal electrons which finally remain in the investigated cosmic data sample is 25.7 candidates after all cuts. This result has a significance of 6.2 σ[26]. The probability that this signal of electrons is only formed by background events is therefore negligibly small and the observation of real electrons among the cosmic data is confirmed.

In order to get an even purer sample of final electron candidates with a higher significance, the binned maximum likelihood fit can also be performed additionally exploiting the charge imbalance of the signal events. In the final electron sample a large surplus of negatively charged candidates is expected and also found in data (30 electrons compared to 4 positrons), as the main source for electrons are ionization processes. The background of muon bremsstrahlung is in contrast nearly evenly distributed concerning the charge of the candidates. Assuming that all real electrons come from ionization and have a negative charge, and all occurring positively charged candidates belong to background, the latter can be removed by a cut on the charge.

[26] The significance is defined as the difference of measured signal and background events over the error on the number of background events: Significance $= \frac{N_{\text{obs}} - N_{\text{backgr}}}{\sigma_{\text{backgr}}}$ [56]. This calculation takes into account the error on the number of background events which follows a Poisson distribution, and the error resulting from the fit itself.

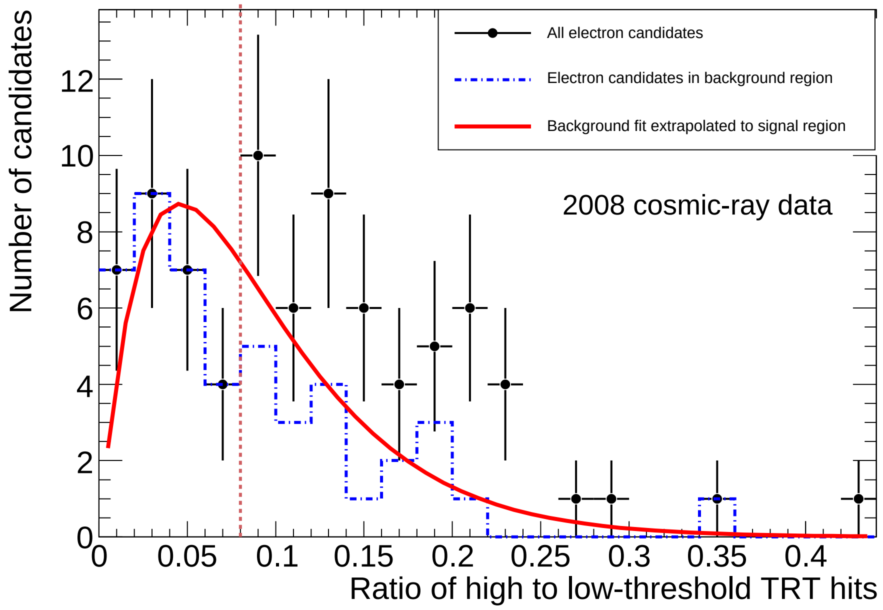

Figure 7.21: Distribution of the HT-TRT ratio for all 81 electron plus positron candidates after the modified medium cuts (black dots). The dashed histogram shows the 47 events in the background region (see text). The red curve shows the projection of the two-dimensional binned maximum likelihood fit. It is renormalized to the reduced number of entries. The orange line indicates the signal cut applied to the bulk of events. The projections have been rebinned, shown is not the binning used for the fit.

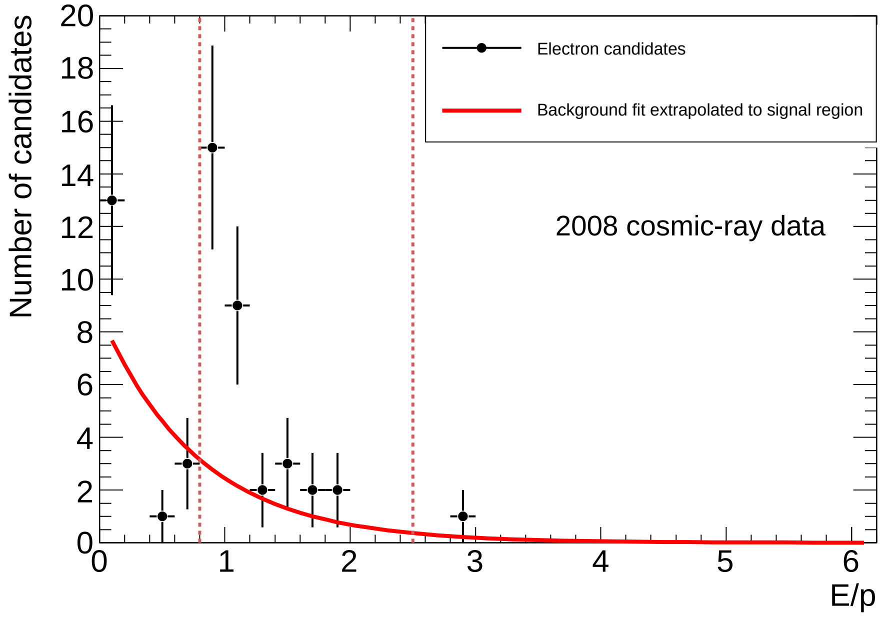

Figure 7.22: Distribution of E/p for all modified medium electron candidates after the additional application of the tight-selection cut on the HT-TRT ratio. The red curve shows the projection of the two-dim. maximum likelihood background fit from which the number of background events under the signal region is estimated. The orange lines represents the main tight cut on E/p. The projections have been rebinned, shown is not the binning used for the fit.

The number of modified medium events in the background region of the ionization sample (fig. 7.10) is then nearly halved from 47 to 28, while in the signal region the number of candidates reduces only from 34 to 30. If the binned maximum likelihood fit is performed on this reduced background region of the ionization sample again in the same way as explained above, and the result is then integrated over the signal region, this yields a number of 4.2 $\pm$ 2.2 background events among the 30 final delta electrons. The significance increases to 8.6 σ.

Nevertheless, as explained in sec. 7.1.3 and in appendix B the four positrons in the final modified tight sample probably originate from conversions. Therefore, no cut on the charge of the electron candidates is performed and all 34 final candidates are kept for further studies. In order to be able to support the obtained result by the maximum likelihood fit on the background fraction among the final signal electrons, the cosmic Monte Carlo data will be examined in sec. 8.

7.3 Data/Monte Carlo comparison of electromagnetic cluster properties

In order to consolidate the isolation of electron candidates from data, the lateral and longitudinal shower profiles of the 34 candidates are investigated. They are then compared to a single particle sample of simulated electrons with a transverse energy of 5 GeV which are produced at the center of the detector and are therefore projective electrons (see sec. 4.3.1). Of these projective events only those with $|\eta| < 0.8$ are considered, to be able to compare them to the electron and positron candidates of the cosmic data which also are required to be in the barrel ID detector (see sec. 7.1).

In total 1408 simulated electrons are considered, to which the same identification cuts have been applied as to the events of the cosmic data. The comparison of the shower shape distribution is shown in fig. 7.23. The first investigated variable is the lateral containment of energy in the cells of the second EM layer (upper left plot). The ratio of energy deposited in a window of 3$\times$3 and of 3$\times$7 cells (one cell has an extension of 0.025 $\times$ 0.025 in $\eta \times \phi$) is shown which has a large value, for both Monte Carlo and real data. This behaviour meets the expectation that electrons tend to have a small lateral shower width. Secondly, the lateral extension of the shower in η direction in the first EM layer is examined (upper right plot). The total shower width (Wtot, see sec. 4.4 for definition) in units of η weighted by the strip energies in the first EM layer is displayed which also is in good agreement for data and MC. The third and fourth variables refer to the longitudinal shape of the electron showers. The fraction of energy deposited in the first EM layer with respect to the total cluster energy (lower left plot) and the fraction of energy deposited in the second EM layer (lower right plot) is studied. The average values should be each above 40% for electrons, as they tend to begin to shower early in the Calorimeter and leave most of their energy in these two layers. Both plots agree well, although the distribution of the energy fraction in the second sampling shows some small discrepancies. In the distribution of the fraction of energy in the first sampling, one event with a fractional energy deposition of only 0.001 inside this layer stands out.

The small discrepancies between Monte Carlo and real data distributions can be explained by the fact, that several real data events differ strongly in their energy values from the simulated electrons which influences the shower shapes (see fig. 7.13). As a consequence the energy distribution of the showers can no longer be compared directly and might differ to a larger extent. In order to support this, the shower shape distribution is shown in fig. 7.24 for only the real data events with an energy smaller than 10 GeV. As expected the agreement between the real and simulated data improves. To study the complete distribution of energy in the whole EM and to investigate the outlier event in the $f1$ (Fraction of energy in first layer) distribution, also the energy fraction left in the Presampler and the third EM layer with respect to the total cluster energy are considered in fig. 7.25. As expected the amount of energy deposited here is

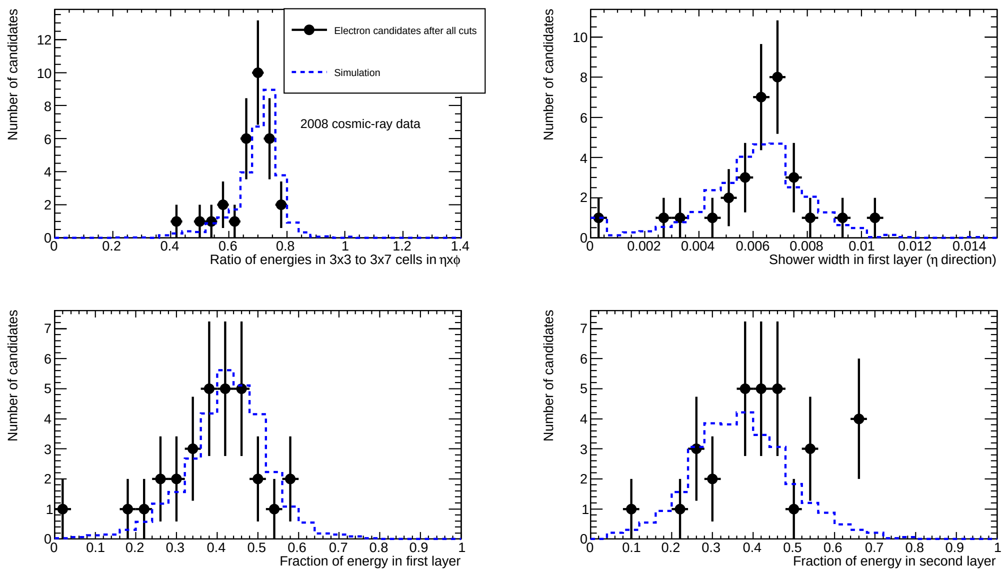

Figure 7.23: Comparison of shower profiles for all 34 final candidates of the cosmic data sample to simulated projective electrons with a transverse energy of 5 GeV and $|\eta| < 0.8$. The black data points indicate the electrons from cosmic data, the blue line marks the simulated electrons. The upper left plot shows the ratio of energies deposited in a window of 3×3 over 3×7 cells ($\eta \times \phi$) in the second EM layer. The upper right plot shows the total shower width in units of η in the first EM layer. The lower plots depict the distribution of the fraction of energy deposited in the first (left) and second (right) EM layer. The Monte Carlo distributions are scaled to the number of data events.

relatively small for nearly all events. Only one outlier event deposited a large fraction of 0.32 of the total energy in the third layer. A closer investigation reveals that this is the same event which left a far too small amount of energy in the first sampling (0.1%) and a quite large fraction of 65% of its energy in the second sampling. This means that for this event the electromagnetic shower developed quite late which is very atypical for a real electron. In addition the energy of this candidate is about 60 GeV which is relatively high for electrons produced via one of the investigated processes. This leads to the conclusion, that this event is rather a photon emitted by a cosmic muon at a later point in the Calorimeter and can therefore be numbered among the background events. As a last step in order to confirm the observation of real electrons, the distribution of energy in the single cells or strips respectively of the first two EM layers which form the reconstructed electron cluster are investigated for the final electron candidates. The distribution of the energy deposition in the strips of the first layer in units of η is shown in fig. 7.26 (left) exemplary for one typical electron candidate. The energy deposition in the 3×7 cells of the second sampling in η and ϕ direction for the same candidate can be seen in fig. 7.26 (right). In both plots the 'hottest' cell or strip of the cluster with the largest energy deposition can be identified easily which is surrounded by a broad distribution of energy in the nearby cells or strips. The same study was done for all candidates yielding similar results. It can therefore be excluded, that these EM clusters have merely been built of single noisy cells or strips.

The lateral and longitudinal distribution of the shower energy in the different EM layers agrees with the expectations for real electrons and confirms that the final sample of 34 candidates consists mainly of real electrons and positrons. The comparison with simulated electrons also shows that Monte Carlo simulations are capable of describing clusters which are created by electrons.

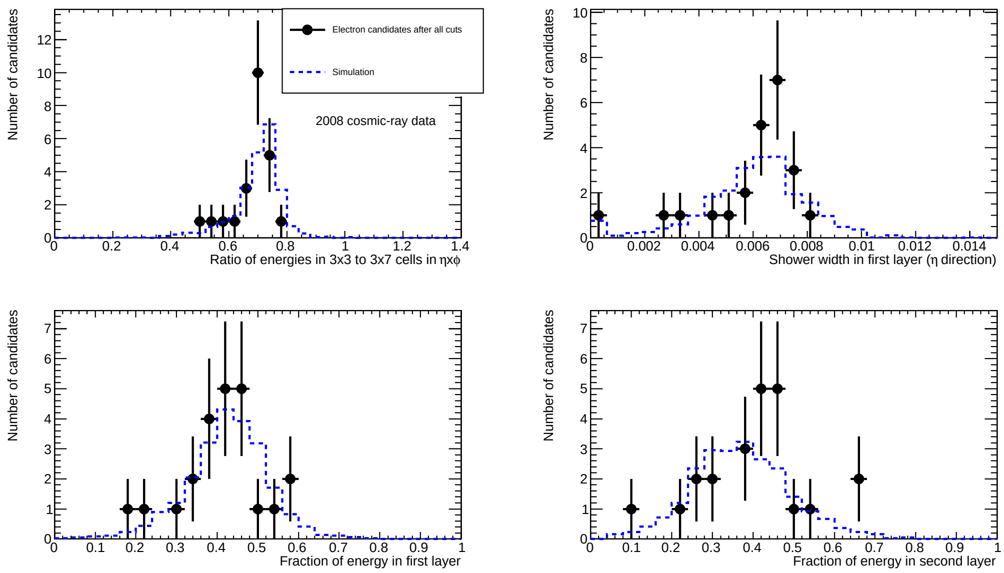

Figure 7.24: Same as previous plot: Comparison of shower profiles for all 34 final candidates (black data points) to simulated projective electrons (dashed blue line) with a transverse energy of 5 GeV and $|\eta| < 0.8$. In these plots only the electron candidates from data with an energy < 10 GeV are shown.

Summary of results

In total, a final sample of 34 electron candidates, 30 electrons and four positrons, has successfully been extracted from cosmic data by making use of the signature of the electron production processes in the detector and the combined information from ID and EM. The background among these candidate is estimated by a two-dimensional binned maximum likelihood fit to be 24%. A signal of 25.7 electron events remain above background with a significance of 6.2 σ. Of the initial 3.5 million cosmic muon events with a high-level trigger track candidate in the ID barrel this yields a number of about $1 \cdot 10^{-5}$ electrons per traversing muon.

The detected electron candidates are mostly delta electrons from muon ionization processes which have been distinguished from background and other processes by their signature in the detector. The properties and topology of the final candidates agrees well with the expectations from theoretical calculations and Monte Carlo truth information.

The reconstruction and cut efficiencies seem to be relatively small for electrons, since of the theoretically expected 1301 ± 562 delta electrons only 25.7 have been found in this sample. Given this small efficiency it cannot be expected that electrons or positrons from the more seldom conversion or decay processes can be extracted with reasonable statistics from this cosmic data sample, for which only 65 ± 57 and 17 ± 11 events respectively have been expected in total from theoretical calculations. Indeed, no clear evidence in data has been found for these processes (see appendix A), although the remaining four positively charged candidates in the final data electron sample might be candidates from a conversion (see appendix B). In order to study the exact cut and reconstruction efficiencies the cosmic Monte Carlo data will be investigated in the next section.

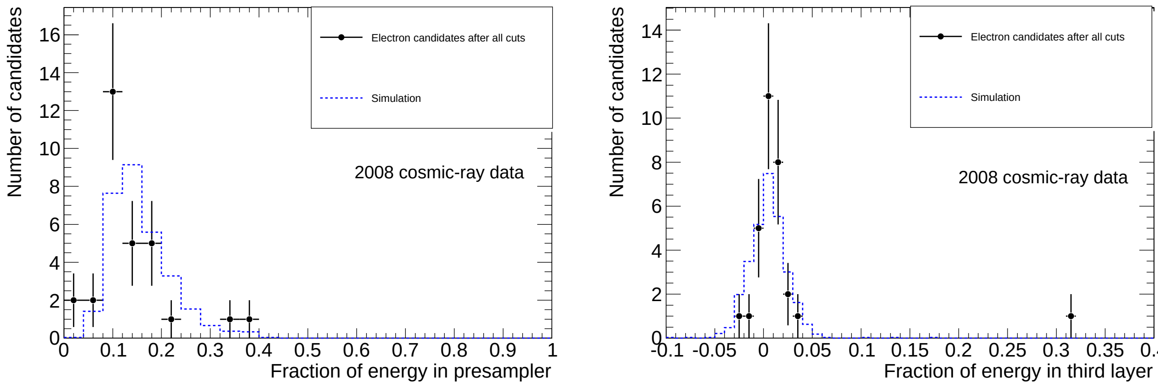

Figure 7.25: Fraction of energy deposited in the Presampler (left) and third EM layer (right) with respect to the total cluster energy. Shown is a comparison of shower profiles for all 34 final candidates (black dots) to simulated projective electrons (dashed blue lines) with a transverse energy of 5 GeV and $|\eta| < 0.8$.

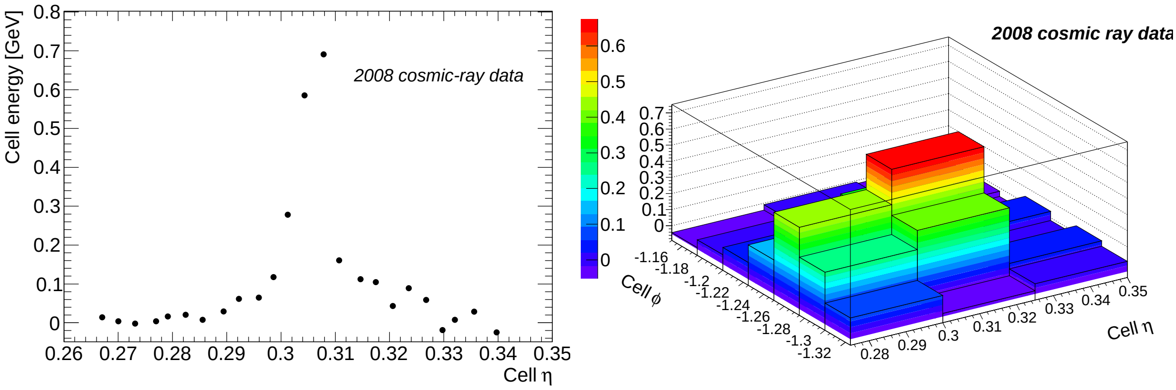

Figure 7.26: Energy deposition in the strips of the first layer along η for one typical electron. Energy deposition in the cells of the second layer (in units of GeV) versus η and ϕ. Shown is the same electron candidate.

8 Comparison of data results to simulated cosmic events

In order to compare the results obtained from cosmic data namely the separation of a clean electron sample from the large background of muon bremsstrahlung, a data set of ca. 10 million simulated cosmic events is investigated (see description of data sample sec. 5.1). This thesis focusses on the analysis of real cosmic data recorded with ATLAS, and a method to isolate electrons has been developed on data-only information since a cosmic Monte Carlo sample at reasonable statistics has not been available in the beginning. The studies of the cosmic Monte Carlo sample are therefore only used to back up the results from data instead of providing a full analysis. Only several aspects will be investigated which help to reproduce and support the data results, for example the information from the Monte Carlo truth. The efficiency of electron reconstruction and identification cuts will be studied in more detail. Possible explanations will be searched for both in simulated and real cosmic data samples to explain why the final electron sample is rather small compared to the theoretical expectation.

8.1 Isolation of delta electrons from a cosmic Monte Carlo sample

In order to isolate electrons from the main source of muon-ionization processes in the Monte Carlo sample, the same methods are implemented as in the real cosmic data sample. Data and Monte Carlo sample cannot be expected to be totally consistent since the data sample is built of events with a high-level trigger track candidate in the ID, while the Monte Carlo sample is set up of simulated cosmic muon events which cross the ID. As the trigger and reconstruction rate for ID tracks is relatively high [59], a comparison can nevertheless be made.

All events of the *ElectronAODCollection* are considered which are candidates reconstructed by the cluster-based or track-based algorithm. In total these are 9125 events. A cut on the longitudinal impact parameter $|z_0| < 1000$mm is performed also here to reduce the analysis to tracks in the ID barrel. This reduced the number of electron candidates to 8061, thus by a factor 0.88. The track reconstruction in the end-caps is inefficient as observed already in real cosmic data. The fraction of events found by the two different reconstruction algorithms can be seen in table 8.1.

	egamma	softe	both
Candidates	96.1%	3.6%	0.4%

Table 8.1: Fraction of electron candidates found by the two different reconstruction algorithms in the cosmic Monte Carlo sample

Most candidates are reconstructed by the *egamma* algorithm is much larger because most electrons resulting from cosmic muons do not cross the center of the detector and cannot fulfil the track quality requirements of the *softe* algorithm.

As a next step, the events in the cosmic Monte Carlo data sample are analogue to real data separated into two subsamples with respect to their signature in the detector to account for the differences between the main signal process of delta electron production and the background of muon bremsstrahlung. The cosmic Monte Carlo samples were adjusted to an updated data reprocessing (see sec. 5.1) in comparison to the real data samples. As a consequence the definition of track signs for the muon candidates are different (see sec. 4.2). The cut selection applied for the creation of the subsamples therefore needs to be adjusted to this. The events in the *ionization (signal)* sample are supposed to contain a large fraction of real electrons from ionization processes. These events are required to feature:

- two or more ID tracks
- one electron candidate in the bottom half of the detector (with $\phi < 0$)
- one or more muon candidates; if the number of muons is ≥ 2, of the two candidates with the highest momentum both are required to point downwards ($\phi < 0$) and have the same charge.

For the *bremsstrahlung (background)* sample which is supposed to consist mainly of background events, the selection does not change:

- exactly one ID track
- one electron candidate in the bottom half of the detector (with $\phi < 0$)
- one or more muon candidates

Further identification cuts are applied on the events of these subsamples, exactly in the same way as explained in sec. 7.1.2. In addition, the number of truth electrons is extracted from the cosmic Monte Carlo data. The matching of a truth to a reconstructed electron candidate is done in the following way: In each event with a truth electrons which originates from a muon (delta electron or decay) or a photon (photon conversion) originating from a muon, the reconstructed candidate with the smallest ΔR to this truth electron is chosen to be the matching candidate.

Results from Monte Carlo sample

The resulting numbers of events after the identification cuts are given in table 8.2. The numbers of reconstructed electrons which match a truth electron after the different cuts are listed in brackets.

	All candidates	Loose	Mod. Medium	Mod. Tight
Total No. of electron candidates	8061 (521)	3945 (300)	1240 (84)	66 (34)
Ionization sample	719 (196)	357 (122)	118 (40)	40 (30)
Bremsstrahlung sample	6739 (287)	3315 (163)	1043 (41)	24 (4)

Table 8.2: Event numbers after the separation in a signal and a background sample and application of the electron identification cuts for cosmic Monte Carlo data. The number of truth electrons matched to the reconstructed candidates is listed in brackets.

The number of events in the bremsstrahlung sample is one order of magnitude larger than in the ionization sample, as it has also been observed for the real data sample. The fraction of all reconstructed candidates matching a truth electron is much larger in the ionization sample (27%) than in the bremsstrahlung sample (4%). The application of the modified tight cuts reduces the number of events in both samples, but for the ionization sample a much larger fraction of events remains after the modified tight cuts (40 of 719) in contrast to the bremsstrahlung sample (24 of 6739). As expected, a much purer sample of final electron candidates remains in the ionization data: 75% of the reconstructed candidates match a truth electron, while in the bremsstrahlung sample only 17% do. The correctly-matched electron candidates in the bremsstrahlung sample with only one track in the ID either overlap with the muon track or have a too small momentum to be reconstructed (see also end of this section).

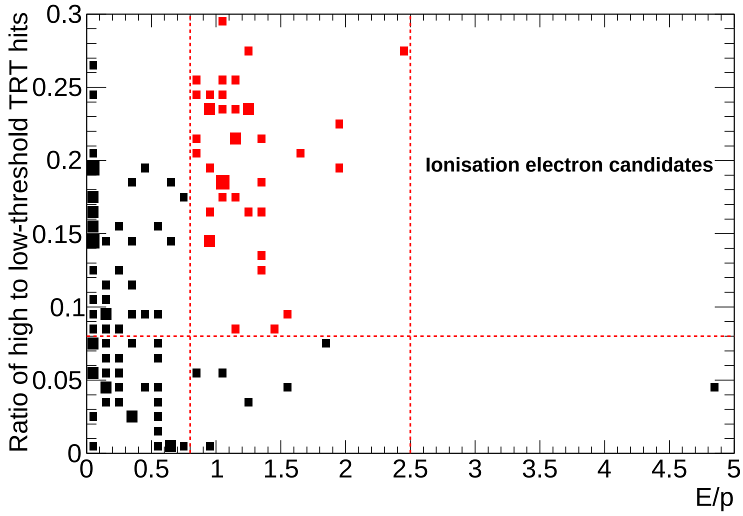

Figure 8.1: Two-dimensional distribution of the ratio of high to low-threshold TRT hits vs. E/p for the ionization sample of Monte Carlo sample. The black boxes show all electron candidates which survived the modified medium cuts. The red boxes mark the electron candidates which in addition survived the modified tight cuts. The orange lines show the cuts applied to most of the events at $\eta \approx 0$ and $E_T < 7.5$GeV: $0.8 < E/p < 2.5$ and HT-TRT ratio > 0.08. One background event with a high HT-TRT ratio and one background event with a high E/p are not included.

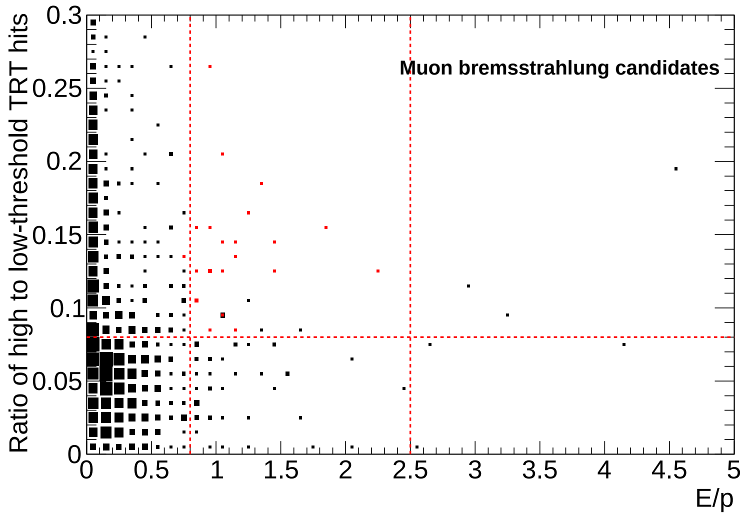

Figure 8.2: Same distribution as above, shown for the bremsstrahlung sample of the Monte Carlo data. Several outliers with a high HT-TRT ratio are not included.

These results are consistent with the ones obtained from real data sample and corroborate the hypothesis that the modified tight selection cuts provide a relatively clean sample of real electrons. The differences which occur can be ascribed to the different configuration of real and Monte Carlo data samples as described above. For instance, the total number of reconstructed electrons is smaller for the cosmic Monte Carlo sample although it contains three times more cosmic events initially. The simulation of the rare cases where high-energy electrons occur might not be entirely accurate, either. This is also a hypothesis to explain the differences between the analytical calculations of electron probabilities and the spectrum of all truth electrons in the whole Monte Carlo sample (sec. 6).

Also for the cosmic Monte Carlo sample, the two most important variables for a discrimination of signal and background events are investigated for the two subsamples: The ratio of cluster energy and track momentum and the ratio of high to low-threshold hits in the TRT. The two-dimensional distribution is shown for the ionization sample in fig. 8.1 and for the bremsstrahlung sample in fig. 8.2 (compare sec. 7.1.2 and plots 7.10 and 7.11). For the bremsstrahlung sample most events do not survive the modified tight cuts while in the ionization sample a large fraction of events have a high E/p and HT-TRT ratio value. This is again consistent with the real data sample in which the events show the same behaviour. The comparison of the E/p and HT-TRT ratio distribution for events with and without a truth match is depicted in fig. 4.6. The candidates with a matching truth electron accumulate around one for E/p and at larger values for the HT-TRT ratio in contrast to the not-matching candidates. This clearly proves that the application of cuts on these variables to extract the real electron events from the data samples is reasonable.

Among the final electron candidates of the Monte Carlo ionization sample, there are two positrons. One matches a truth positron resulting from a conversion process, while the other one does not have a truth match and is therefore a background event. This implies that the four positrons found in the real final electron sample cannot be definitely matched to one of these categories, as it has already been anticipated.

Background estimation

The background estimation performed in the real cosmic data sample should also be backed up by the analysis of the cosmic Monte Carlo sample. The two-dimensional binned maximum likelihood fit described in sec. 7.2 is performed in the same way on the background region of the HT-TRT ratio distribution vs. E/p (fig. 8.1) for the ionization sample in cosmic Monte Carlo data. The signal region, which is excluded for the fit, is consistently with the tight cuts chosen as $0.8 < \mathrm{E/p} < 2.5$ and HT-TRT ratio > 0.08 (indicated by the lines in the figure). The parametrization developed from the real data samples is also in this case chosen for the fit-function. The fit result for the parameters in the ionization sample is:

$$\begin{aligned} a_0 &= 89.3 \pm 14.8 \\ a_1 &= 1.81 \pm 0.33 \\ a_2 &= 18.62 \pm 2.25 \end{aligned} \tag{8.1}$$

The correlations of these parameters are $c_{01} = -0.220$, $c_{02} = -0.140$ and $c_{12} = 0.158$. The projections of the fit curve for the two corresponding variables can be seen in fig. 8.3. The integral of the fit-function over the signal region yields the number of background events:

$$N_{\mathrm{backgr}} = 11.1 \pm 3.9 \tag{8.2}$$

The remaining number of signal electron events is therefore 28.9 and the fraction of background events $(28 \pm 10)\%$ in the final sample. This result can be compared to the background fraction in the final sample which is obtained from the Monte Carlo truth matching. Here, 30 electron candidates match a truth electron out of 40 final candidates (table 8.2).

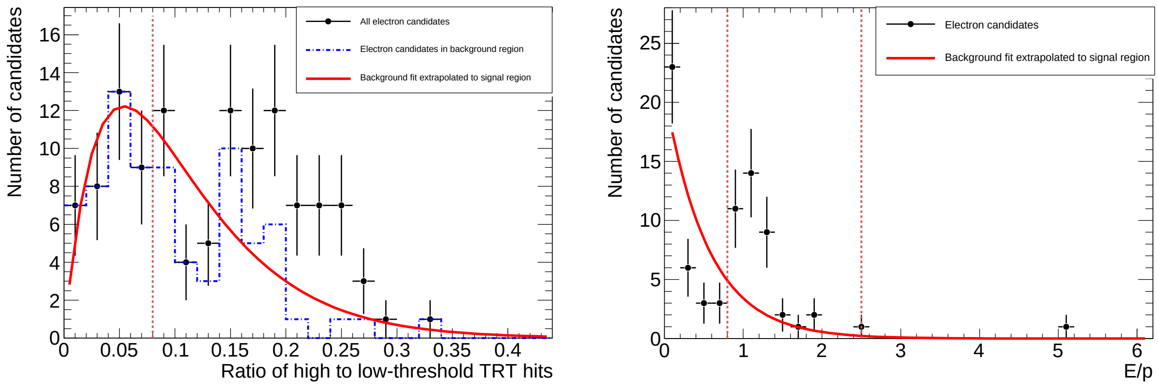

Figure 8.3: Left: Distribution of the HT-TRT ratio for all electron plus positron candidates after the modified medium cuts in the MC sample(black dots). The dashed histogram shows the events in the background region (see text). The red curve shows the projection of the two-dimensional binned maximum likelihood fit. The orange line indicates the signal cut applied to the bulk of events. Right: Distribution of E/p for all modified medium electron candidates after the additional application of the tight-selection cut on the HT-TRT ratio in the MC sample. The red curve shows the projection of the two-dim. maximum likelihood background fit. It is renormalized to the reduced number of entries. The projections have been rebinned, shown is not the binning used for the fit.

This yields 10 ± 2.7 background events[27] in the signal region and thus a fraction of $(25 \pm 7)\%$ which agrees well with the fit result within the error limits. The maximum likelihood fit is therefore a reliable method for the estimation of the background among the final candidates. The results from the Monte Carlo sample are also consistent with the fit result of the real data sample where the fraction of background events among the final candidates has been estimated as $(24 \pm 9)\%$ (sec. 7.2).

Investigation of the final electron candidates

The final 40 electron candidates found in the ionization sample of the cosmic Monte Carlo data are further investigated. The electron cluster energy distribution for all candidates can be seen in fig. 8.4 (left). Similar to the real data sample, the events accumulate at 5 GeV as the cluster-finding algorithm is increasingly inefficient for lower energies [55]. It decreases towards larger energies where the probability for electron production gets smaller. Also the cluster η distribution is shown in fig. 8.4 (right) for all final candidates. It can be noticed that all electron candidates are produced in the central region of the detector.

The distribution of the generation origin of all matching truth electrons in the final sample is displayed in fig. 8.5. It can be noticed that the electrons originate all from the two upper thirds of the detector which shows that they need to cross a certain path length in the detector to be reconstructable as an electron candidate. The azimuthal angular difference of the two highest p_T ID tracks in the ionization sample is studied for the final candidates, as well. The track ϕ directions are evaluated at the space points which lie closest to the approximate origin of the reconstructed electron track (see description in sec. 7.1.3). Since for the large fraction of TRT-only tracks no information on the polar track angle is provided, only the azimuthal track distance can be studied for all candidates.

[27] The error on this number is calculated from the standard deviation of a Binomial distribution $\sqrt{\epsilon(1-\epsilon)N}$, [56], $\epsilon = k/N$. The variable k denotes the number of background events and N the total number of events in the final sample.

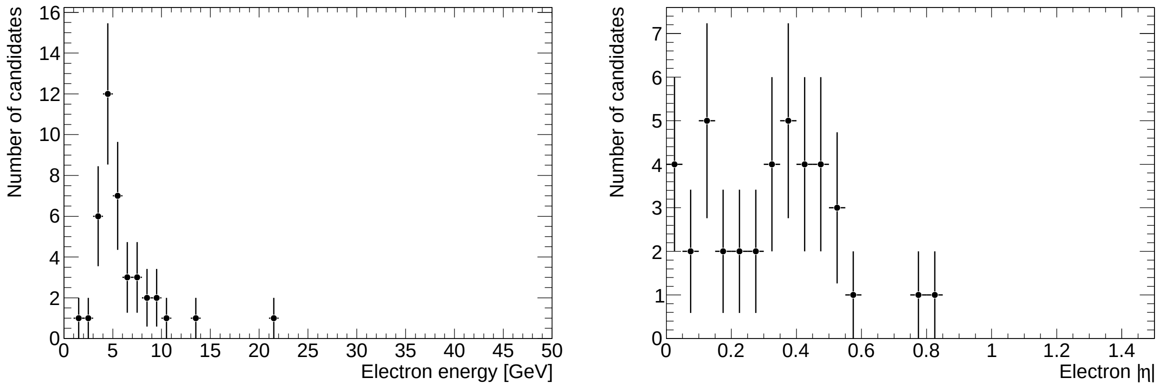

Figure 8.4: Left: Electron cluster energy for all 40 final electron candidates in Monte Carlo sample. Right: Absolute cluster η position of the final electron candidates.

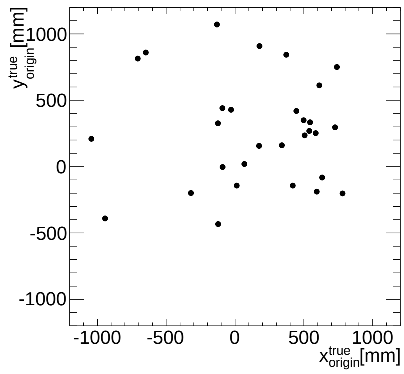

Figure 8.5: True production origin of all 30 matched truth electrons in the final electron sample of the MC data.

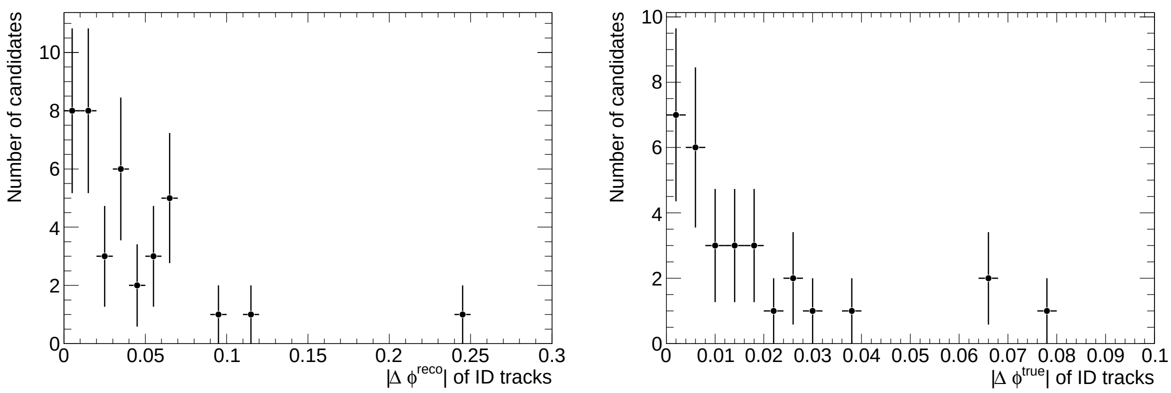

Figure 8.6: Left: Absolute difference in ϕ of the two highest p_T reconstructed ID tracks is displayed for all 40 final electron candidates in the MC sample. The ϕ directions are evaluated at the track space points closest to the approximate electron origin. (Two outliers are not included.) Right: Absolute difference in ϕ of the truth muon and electron evaluated at the truth electron production origin. The plot shows all 30 matched truth electrons of the final electron sample in MC data.

One can see in fig. 8.6 (left) that all events have a very small $\Delta\phi$. In comparison, also the difference in ϕ between the incoming truth muon and the truth electron at its origin is displayed in fig. 8.6 (right). On average, the $\Delta\phi$ calculated for the reconstructed tracks is larger since the angles cannot be evaluated exactly at the origin and the particles have undergone already a deviation by the magnetic field. Both plots are consistent with the anticipation that delta or conversion electrons with high energies are emitted under small angles with respect to the muon flight direction as it has been figured out by the exemplary calculations of the angular differences between muon and electrons in the theory chapter (sec. 6). All examined properties of the final electron sample in cosmic Monte Carlo data agree well with the observations made in real data and prove once again the validity of these results.

Finally, the matching of truth and reconstructed energy is investigated to ensure that the energy reconstruction and calibration is reliable. The distribution of the ratio of truth and reconstructed electron energy is illustrated in fig. 8.7 for both samples separately. In both cases, a peak around one can be observed which complies with the anticipation. The average is slightly larger than one (1.15 in the ionization sample) which shows that the energy calibration is not 100% accurate.

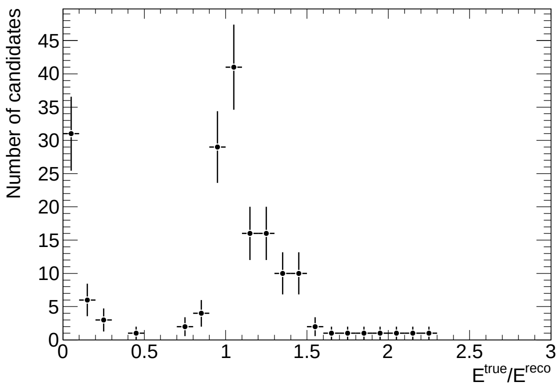

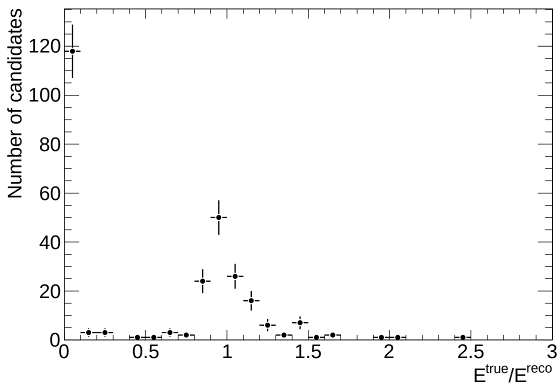

Figure 8.7: Left: The ratio of truth over reconstructed cluster energy of all truth-matching electron candidates in the ionization sample of the MC data. The truncated mean for an energy ratio > 0.3 is $< \frac{E^{\mathrm{truth}}}{E^{\mathrm{reco}}} >= 1.15$ with a standard deviation of 0.26. Right: The ratio of truth over reconstructed energy for all truth-matching candidates in the bremsstrahlung sample of the MC data. The truncated mean for an energy ratio > 0.3 is $< \frac{E^{\mathrm{truth}}}{E^{\mathrm{reco}}} >= 1.04$ with a standard deviation of 0.25.

For a large fraction of events in the bremsstrahlung sample the ratio of the energies is smaller than 0.1 which means the truth energy is very small compared to the reconstructed. In the ionization sample there are also several events with a very low energy ratio, although the fraction is smaller than in the bremsstrahlung sample. To investigate this in more detail, the truth energy versus the difference of truth and reconstructed energy is plotted for the ionization sample in fig. 8.8. One can see that the events which have a small energy ratio in fig. 8.7 (left) correspond indeed to events where the truth energy is below 1 GeV. This value is far below the cluster reconstruction threshold of $\mathrm{E_T}$ = 3GeV. Mostly likely the reconstructed cluster of the electron candidate has not been formed by a delta or conversion electron alone or at all. Instead, a coincidence of an electron production and bremsstrahlung photon emission by the cosmic muon must have occured which led to the conjoint formation of a high-energy shower in the EM. This explains why the fraction of these low-energy truth electrons is much larger for the bremsstrahlung sample with only one track in the ID - the electron track has a too small

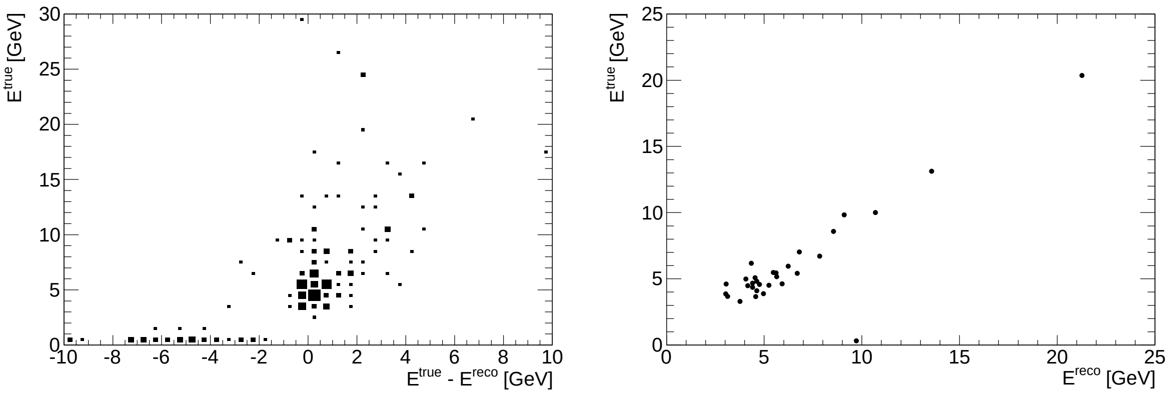

Figure 8.8: Left: The dependency of the difference between truth and reconstructed energy (x-axis) on the truth electron energy (y-axis) displayed for all electron candidates matching a truth electron in the ionization sample of the MC data. The truncated mean of the energy difference for a truth energy larger than 3 GeV is 0.9 GeV with a standard deviation of 1.6 GeV. Right: The distribution of the truth vs. reconstructed energy for all 30 matching final electron candidates in the MC ionization sample.

momentum to be reconstructed with an own track. However, the majority of events in fig. 8.8 (left) with a larger truth energy accumulate around zero indicating that truth and reconstructed energy are roughly consistent. The truncated mean of the energy difference for a truth energy > 3 GeV is 0.9 GeV with a standard deviation of 1.6 GeV which reveals again that the truth energy is slightly underestimated in the calibration.

To confirm that the events with a very small truth energy have not been selected by the identification cuts the truth versus reconstruction energy distribution is shown for the 30 final electron candidates with a truth match in fig. 8.8 (right). The truth and reconstructed energies match well for all candidates except for one. The events with a mismeasured energy are therefore nearly entirely suppressed by the identification cuts and the reconstruction of energy for the final candidates can be regarded as reliable.

8.2 Cut efficiencies

In order to compare the number of isolated electron candidates in the Monte Carlo sample to the theoretical expectation from the whole Monte Carlo truth spectrum and the analytical estimations, and to determine the exact reconstruction and cut efficiencies, the different production processes of the isolated electron candidates with a truth-match in the Monte Carlo sample are extracted.

The matched truth electrons can be distinguished by the particle-ID of the respective mother particle and the other decay products occurring in the event. A truth electron or positron originating from a photon which in turn results from a muon, is flagged as a bremsstrahlung-photon conversion. An electron originating from a muon is flagged as a delta electron unless among the other events a truth electron neutrino is found, in this case the electron originates from a muon decay. Among all truth-matching reconstructed electron candidates in the examined cosmic Monte Carlo sample, the truth electron originates in 451 cases from a muon ionization, in 54 from a photon conversion and 16 candidates originate from a muon decay. The final correctly-matched tight candidates consist of 27 delta electrons and 3 conversion candidates of which one is a positron. No decay electrons are among the final candidates (see also appendix A). In the conversion events always two truth electrons of opposite charge are found conform to the expectation, but only one electron candidate is reconstructed. Thus delta electrons are the largest source of electrons, followed by conversion. This is consistent with the theoretical expectation and the analysis of all truth candidates in sec. 6 and again strengthens the results of the analysis of the real data sample from which the same conclusions have been drawn.

However, the expected total number of high-energy electrons from the analytical estimation and total Monte Carlo truth content is much higher (see sec. 6): 2928 truth delta electrons, 784 electron positron pairs and 89 electrons from muon decays with a total energy > 3.27 GeV are included in the truth of the whole Monte Carlo sample. This means a very large fraction of produced electrons is not reconstructed in ATLAS as it has already been found in data.

The exact efficiencies of the cut selection applied to the electron candidates are investigated in the following for the ionization sample of the cosmic Monte Carlo data, separately for the two largest electron processes - ionization and conversion.

Efficiencies in %	Reconstructed	Loose	Mod. Medium	Mod. Tight
Delta electrons	6.4 ± 0.5	4.0 ± 0.4	1.4 ± 0.2	1.0 ± 0.2
Conversion electrons	4.0 ± 0.8	2.4 ± 0.6	0.7 ± 0.3	0.4 ± 0.3

Table 8.3: Efficiencies of the reconstruction and different cut selections for electron candidates in the MC ionization sample, listed separately for delta electrons and electrons from bremsstrahlung photon conversions

The efficiencies for the reconstruction and different cut selections are calculated as follows: To obtain the delta-electron efficiency, the number of correctly-matched reconstructed electrons contained in the ionization sample and passing the loose/medium/tight selection is divided by the number of all truth electrons which are flagged as delta electrons (see above). To obtain the conversion-electron efficiency, the number of correctly-matched reconstructed electrons and positrons contained in the ionization sample and passing the loose/medium/tight selection is divided by the number of all truth conversion pairs. In both cases it is required that the truth electron's energy is above the cluster reconstruction threshold E>3.27 GeV, see sec. 6.1 and 4.2. The efficiencies are corrected by the ratio of events which have a reconstructed track in the ID barrel and the total number of events in the sample with an ID track. This ratio is 0.88 for the Monte Carlo data (see beginning of this chapter). The efficiency is therefore[28]:

$$\epsilon_{\text{delta/conversions}} = \frac{N_{\text{reco/loose/medium/tight,truth match}}}{N_{\text{truth,E>3.27 GeV, muon/photon mother}}} \times \left(\frac{N_{\text{cosmics traversing ID-barrel}}}{N_{\text{cosmics}}} \right)^{-1} \tag{8.3}$$

The resulting efficiencies are listed in table 8.3. In can be seen that all efficiencies are very small.

To detect possible causes for this, the information from cosmic data and Monte Carlo samples is used. They are listed in the following:

- **Decrease of reconstruction and cut efficiencies for low energy electrons** In general, a decrease of efficiency for the track and cluster reconstruction algorithms and the cut selections for electrons with low energies of only several GeV is predicted from studies of Monte Carlo collision data with high statistics [18]. For instance, the electron reconstruction efficiency is below 45% for electron energies < 6 GeV and it is less than 5% for electron energies < 4 GeV, [55].

[28] The error on the track ratio is neglected for this calculation. The error on the efficiency is based on the standard deviation of a Binomial distribution [56], $\delta\epsilon = \sqrt{\frac{\epsilon(1-\epsilon)}{N}}$

- **Requirement of minimal flight length in the ID** electrons are required to leave a track with at least 20 TRT hits in the ID. Thus, they have to cross a certain distance in the TRT to leave a reconstructable track (see sec. 6.1 and e.g. fig. 7.4 (right)). Therefore, not all high-energy electrons produced in the ID can be reconstructed. From analytical calculations for the number of delta electrons emitted in the ID, the ratio of the expected number of reconstructable electrons and the expected number of all electrons produced in the ID has been estimated to be about 70% (sec. 6.3). This reduces the reconstruction efficiency further.

- **Reduced tolerance of non-projective cosmic events** Most electron tracks in cosmic data are non-projective. As a consequence they produce EM clusters that might fail the *sliding-window* algorithm for reconstruction which is optimized for electrons coming from the detector origin (see sec. 4.3.1).
  In fig. 8.9 the projectivity of the electron candidates from cosmic ray data is examined. The corresponding plot for the Monte Carlo is shown in fig. 8.10. The ID tracks of the electron candidates are extrapolated to the surface of the first EM layer. The electron's flight direction is evaluated at this point, and the difference in η and ϕ is calculated between the flight direction and the vector from the detector origin to the electron's impact point in the first EM layer.
  The difference in ϕ is illustrated in the upper left plot for all electron candidates and for the ones which survived the modified medium cuts. Since there is no information on the η track direction for the TRT-only tracks, the $\Delta\eta$ distribution on the upper right is only investigated for the electron candidates which have at least one silicon hit.
  In addition, also the ΔR distribution is investigated only for tracks with at least one silicon hit, this of course constrains also the involved $\Delta\phi$ distribution in comparison to the first plot. It can be noticed that consistently for data and Monte Carlo events, primarily the $\Delta\eta$ distribution is constrained to very small values ($|\Delta\eta| < 0.15$). Tracks which are increasingly non-projective are therefore strongly suppressed during the reconstruction. Based on the detector geometry one can assume that differences in η up to 0.8 can uniformly occur, this reduces the number of candidates by more than 80%. The effect is larger in η direction since the Calorimeter cells in the R-z plane have a small angular acceptance, and the electrons in this plane enter the Calorimeter on straight paths. In contrast, in the ϕ direction the cells have a larger acceptance due to their R-ϕ symmetry, and the electron tracks are bent by the magnetic field. This increases the area which is covered by the shower also for projective tracks, and the difference to non-projective tracks is here smaller. Also the electron identification cuts, which make use of the shower shape in the Calorimeter, are optimized for electrons coming from the detector center and suppress non-projective electron showers.

- **Energy losses outside the Calorimeter** Another effect which might lead to reduced reconstruction efficiencies is the fact that the threshold of E_T =3GeV for the electron shower reconstruction refers to the energy sum deposited in a window of 5 × 5 cells (see sec. 4.3.1) in the Calorimeter. This approach neglects energy depositions outside the window Calorimeter and energy losses in the ID through bremsstrahlung. Not all events with a $E_{\mathrm{T}}^{\mathrm{truth}} > 3$ GeV will therefore overcome the *sliding-window* threshold. The final electron cluster energy is corrected for these losses after the reconstruction as described in sec. 4.3.1. To investigate the fraction of energy deposited outside cluster area, the difference between the reconstructed calibrated electron energy and the energy sum in all three EM layers

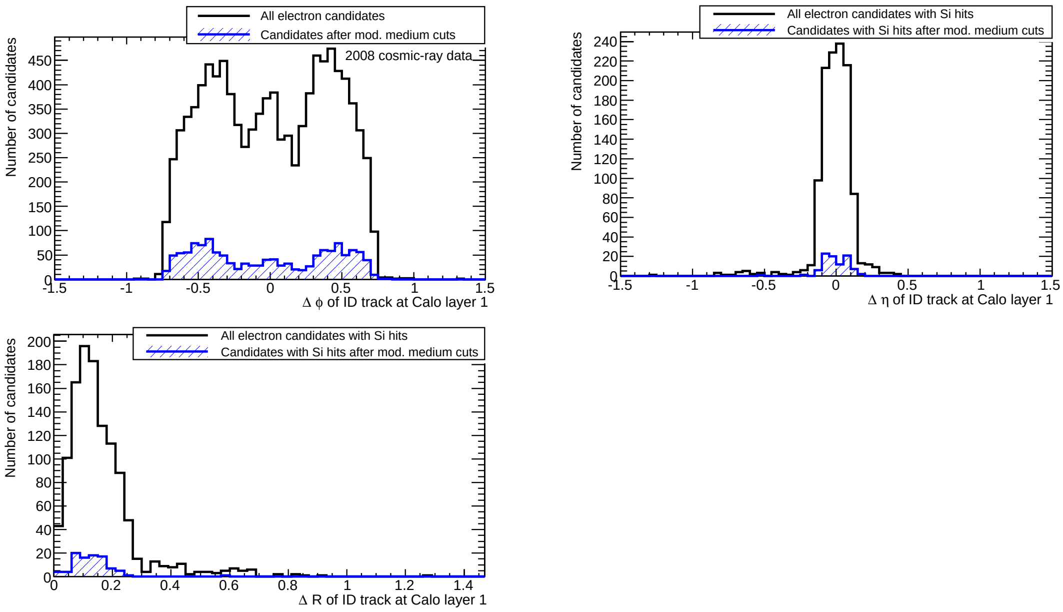

Figure 8.9: Difference in η and ϕ and their combination (ΔR) between the electron's flight direction at the surface of the first EM layer and the vector from the origin to the electron's impact point in the EM layer. The plots show the results from the ATLAS data sample. The black line indicates all electron candidates in the data sample, the blue line marks all events which remain after the modified medium selection. The η and ΔR distributions include only candidates with at least one silicon hit.

and the Presampler[29] is investigated in fig. 8.11 for all electron candidates of the real data sample and the Monte Carlo sample. Fig. 8.12 examines the calibrated electron energy dependent on the absolute difference of the calibrated energy and the sum of energy in all EM layers for the candidates of the real data sample. The deposition of energy outside the cluster window increases with the electrons energy and is on average about 3% of the cluster energy.
In sec. 8.1 it has in addition been observed that also the calibrated cluster energy slightly underestimates the electron truth energy on average by 15%. As a consequence not all events with a total truth energy above 3.27 GeV can be reconstructed which results in a smaller efficiency. If for instance a minimum electron energy of 4 GeV instead of 3.27 GeV is inserted for into the analytical calculation of the number of expected delta electrons (see sec. 6.3), this reduces the number of expected delta electrons in the ID by about 20%.

- **Overlap of electron and muon clusters and tracks** The topology of the electron production processes investigated for cosmic data is relatively challenging for the reconstruction algorithms: The high-energy electrons are emitted under small angles with respect to the muons and thus close-by tracks and clusters need to be resoluted to separate electrons from muons (see sec. 6). If electron and muon have a similar momentum and are of

[29] The finally stored electron cluster object has a size of 3 × 7 cells in $\Delta\eta \times \Delta\phi$ which is slightly different to the initial window of 5 × 5 cells used during reconstruction. This difference is neglected for these investigations.

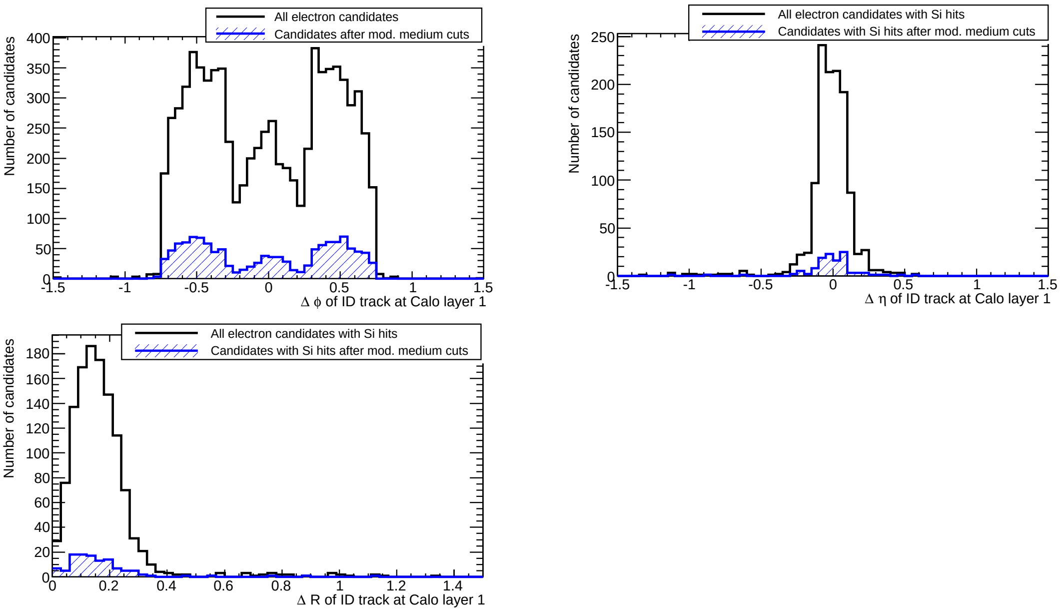

Figure 8.10: Same distribution as in fig. 8.9. The plots show the results from the ATLAS Monte Carlo sample.

the same charge, there is a high probability that their tracks overlap and cannot be distinguished as two separate tracks. Also, their clusters might overlap and fail the identification criteria for the electron object.

It has already been observed that the tracks of many candidates have a small difference in ϕ inside the ID (fig. 7.17 and 8.6). In the bremsstrahlung sample, which features only events with one track in the ID, a large fraction of reconstructed electron candidates matching a truth electron is contained (table 8.2). This shows that in many cases electron and muon track cannot be reconstructed separately. The investigation of $\Delta\phi$ between the two ID tracks extrapolated to the first EM layer (fig. 7.18) is a measure for the angular difference of the energy deposition barycenter of the two particles in the Calorimeter. For a large fraction of the reconstructed candidates the difference in ϕ is smaller than 0.1, while the lateral extension of a cluster in the *sliding-window* algorithm is $\Delta\phi_{\mathrm{cl}} = 0.125$. Thus, the energy depositions in the EM by muon and electron overlap in these cases which leads to the reconstruction of only one single cluster. Falsified position and energy properties will be assigned to this cluster which might cause a rejection of this event by the electron identification cuts. The overlap of energy depositions can also be seen among the positron event displays in appendix B resulting in only one EM cluster.

This might also explain why the cut efficiency for conversion electrons or positrons is smaller than the efficiency for delta electrons. In the former case two electrons are produced very close-by inside the ID, and if both particles have a high energy, the probability for an overlap of tracks and clusters is even higher.

The above listed reasons cause the small cut and reconstruction efficiencies for electrons observed in the cosmic Monte Carlo sample. These arguments apply to the real data events, as

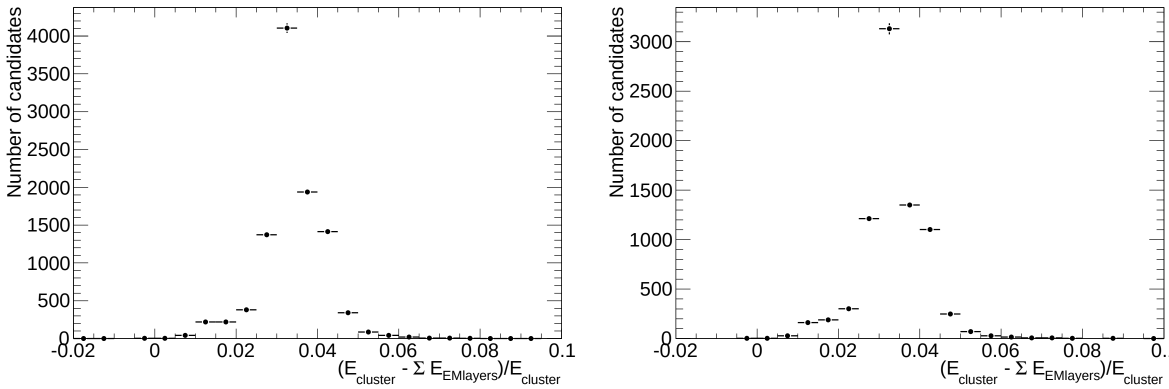

Figure 8.11: Fractional difference of the reconstructed calibrated cluster energy and the sum of energy depositions in the EM layers and the Presampler, shown for all electron candidates of the real cosmic data sample (left) and the cosmic Monte Carlo sample (right). The mean value of both distributions is 0.034 with a standard deviation of 0.008.

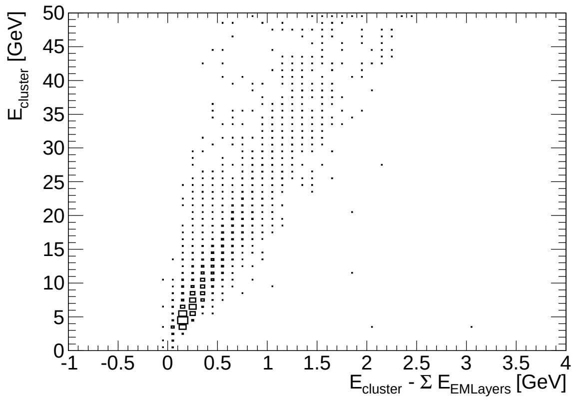

Figure 8.12: The dependency of the absolute difference of the electron's calibrated cluster energy and the sum of energy depositions in EM layers (x-axis) on the calibrated electron cluster energy (y-axis), shown for all electron candidates of the real cosmic data sample.

well, and they explain why much less high-energy electrons are found than anticipated from the theoretical estimations in sec. 6.

Nevertheless, the final sample of electrons found both in Monte Carlo and data is consistent with the expectation that muon-ionization processes are the main source for electrons in cosmic ray data. The emitted high-energy delta electrons are detectable by their special signature of two tracks in the ID. It has been found that the extracted final electron samples have a high purity since the background contained among all reconstructed electron candidates can be reduced by three orders of magnitude by the applied cut selection, and in the final sample a background fraction of only about 25% can be found.

9 Conclusion

This thesis investigates the production of high-energy electrons from cosmic rays in ATLAS and presents the isolation of a clean sample of 34 electrons mainly from ionization processes.

In order to be reconstructed, electrons have to be produced in the Inner Detector with a transverse energy larger than 3 GeV. The three different production processes - muon decay, ionization and bremsstrahlung conversion - are found to have different signatures in the detector by which they can be distinguished. An analytical estimation of the expected probabilities for these processes is provided by assuming a mean energy and effective path length for cosmic muons in ATLAS and mean material quantities for the ID. These calculations predict ionization as the main source of electrons with $(3.7 \pm 1.6) \cdot 10^{-4}$ electrons per cosmic muon. The coarsely estimated numbers agree surprisingly well with the truth electron spectrum in a simulated cosmic data sample. A source of background was found to be muon bremsstrahlung where the EM shower produced by the photon is matched to the muon ID track.

10241 electron candidates in a cosmic data sample of about 3.5 million events with a high-level trigger track candidate in the ID barrel form the basis for the isolation of high-energy electrons. First, the special signature of the ionization process featuring two tracks in the ID is exploited to filter out the background candidates with only one track. Secondly, the standard cut selection for electron identification is applied to the events which makes use of typical properties of electron tracks and clusters in the detector. Several modifications are necessary to account for the special topology of cosmic tracks which often lack Pixel/SCT hits and thus have no accurate η information. Two independent variables, the ratio of the candidate's cluster energy to its ID track momentum and the ratio of high to low-threshold TRT hits indicating the emission of transition radiation are found to be most important for a discrimination of signal and background events. A signal of real electrons has been extracted in form of an accumulation of events around one for E/p and at higher values for the fraction of high-threshold TRT hits.

30 electrons and 4 positrons fulfil all cut criteria of which most have an energy of 5 GeV and are emitted under small angles with respect to the cosmic muon. The investigation of event displays and the agreement of the shower shapes with a simulated electron sample confirms that real electrons mainly from ionization processes have been found. Based on a two-dimensional maximum likelihood fit of the background in the HT-TRT ratio vs. E/p distribution the number of background events in the final sample is estimated to be 8.3 ± 3.0 events. This provides an observation of 25.7 signal electrons with a significance of $6.2\,\sigma$. This proves that the ATLAS tools for electron reconstruction and identification are capable of isolating a clean sample of electrons.

To validate the applied methods the same analysis is performed on 10 million simulated cosmic events with a track in the ID barrel, and well agreeing results are obtained. The number of candidates not matching a truth electron discloses a background fraction of $(25 \pm 7)\%$ among the 40 final candidates which confirms the result obtained from the maximum likelihood fit. The tight cut efficiency for delta electrons is determined to be $(1.0 \pm 0.2)\%$. The investigation of data and MC reveals that this small value can be ascribed to the inefficiency of the reconstruction algorithm at low energies and the special topology of cosmic events which feature non-projective tracks and a frequent overlapping of energy depositions in the EM from electron and muon. This explains why the number of electrons in data is by a factor 40 smaller than initially estimated.

This thesis presents the first observation of electrons in ATLAS, it demonstrates both the excellent commissioning of the Calorimeter and of the Inner Detector with efficient transition radiation and makes confident that early electrons will successfully be reconstructed and identified in ATLAS during the upcoming collision data-taking phase.

A Search for other electron signatures in cosmic data

In order to search explicitly for electrons produced by decay or bremsstrahlung-photon conversion in cosmic ray data, their special signature described in sec. 6 is utilized.

Electrons from decay
As described in sec. 6.2, electrons which result from muon decays feature one incoming muon candidate in the upper MS ($\phi > 0$) and one ID track. The small kink of the electron ID track with respect to the muon ID track can in most cases not be resolved and only one single track is reconstructed. This signature is therefore very similar to the background process of muon bremsstrahlung in which also only one ID track can be found. In decay events no outgoing muon in the lower hemisphere of the detector occurs in contrast to the background process. However, in numerous cases the outgoing muon candidate in the lower hemisphere of the MS is not reconstructed. These background events are then indistinguishable from the decay signature. The application of the modified tight cuts explained in sec. 7.1.2 helps to suppress this background. It has to be taken into consideration, that the reconstructed track candidate is only partially formed from electron track hits, namely only after its production in the decay. The first part of the track hits is left by the traversing muon. This means, that also the fraction of high-threshold hits detected for the entire track is on average smaller, if the electron is produced at an arbitrary point in the detector. To find also electron candidates which come into existence after the muon has already passed a certain distance in the ID, a softer cut on the HT-TRT ratio needs to be applied. The exact requirements to select possible decay events are listed here:

- exactly one ID track
- one electron candidate with $\phi < 0$ fulfilling modified medium cut criteria (sec. 7.1.2)
- electron must survive also the tight cut on E/p and must have a HT-TRT ratio > 0.04
- no reconstructed muon candidate or muon track segments in the lower MS with $\phi < 0$

In the data sample only one event remains which fulfils these criteria. The HT-TRT ratio of this electron candidate is 0.077. The event display is shown in fig. A.1.

Events of this kind are also selected in the cosmic Monte Carlo sample and the origin of the electron candidates is investigated. In the total sample, four events with this signature can be found. Only one of these matches a truth electron from a decay[30], the remaining three do not have a truth electron match and are background events. This shows, that a clean sample of decay events cannot be isolated by this cut selection, the remaining background fraction is too large. Thus, a clear classification of the electron candidate found in the data sample cannot be made, either.

In the Monte Carlo sample only one matched candidate of in total 89 high-energy truth decay electrons remains, which reveals that the efficiency of this cut selection is very small (see sec. 8.2). As a consequence not many decay electrons could have been expected in the data sample, either.

Electron pairs from photon conversions
No event which features two reconstructed electron candidates survives the identification cuts applied to the cosmic data sample (see sec. 7.1.3). Either both conversion electrons have high

[30]It is produced by a muon together with two neutrinos.

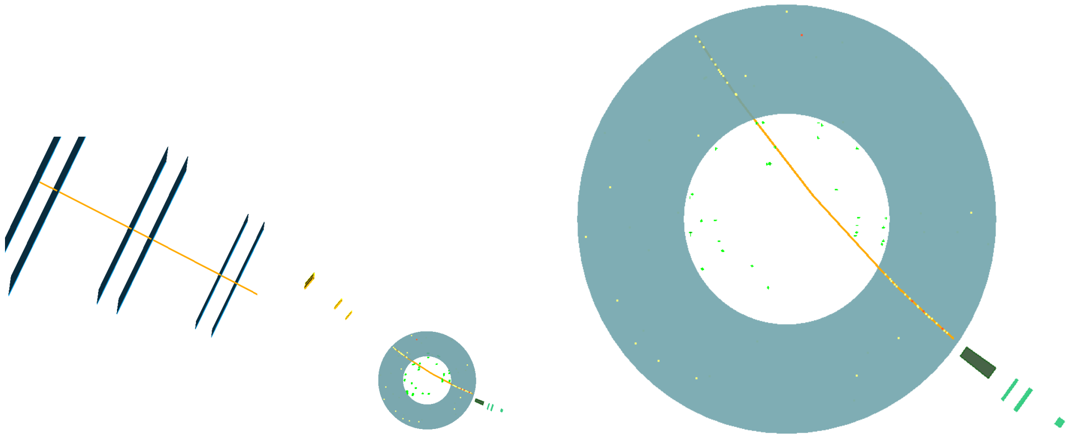

Figure A.1: Event display of a possible decay event in the cosmic data sample (run 91387, event 1749538) in full view (left) and zoomed view (right).

energies and overlap in their cluster, or one electron has a too small momentum to be reconstructed (see appendix B). The expected signature of a photon conversion process (sec. 6.4) can therefore not be found among the cosmic events in ATLAS. However, the investigation of the positively charged electron candidates in the final cosmic ionization sample (see sec. 7.1.3) with two or more tracks, and the examination of the origin of the truth electrons in the cosmic Monte Carlo sample reveals that several electron or positron candidates can be found in which the second candidate of the conversion is not reconstructed. To distinguish them from the main type of electrons resulting from ionization, only the number of reconstructed ID tracks can be utilized. In the case that both candidates from the bremsstrahlung photon conversion have a high energy and their clusters overlap, three ID tracks can be expected in contrast to the ionization events which usually feature only two ID tracks. The selection applied to extract the conversion electron candidates is therefore:

- three or more ID tracks
- one electron candidate with $\phi < 0$ fulfilling modified tight cuts (see sec. 7.1.2)
- one or more muon candidates; if the number of muons is ≥ 2, of the two candidates with the highest momentum one is required to be in the top half ($\phi > 0$) of the detector and the second one in the bottom half ($\phi < 0$) and both are required to have opposite charge.

In the data sample five events fulfilling these cuts remain. The application of the same selection to the Monte Carlo sample yields also five remaining events with this signature. Of these, only two match a truth electron or positron from conversion[31]. Thus, also in this case the background fraction is relatively large and a clear classification of the events in the data sample cannot be made.

One can therefore conclude that only electrons from ionization can successfully be isolated from cosmic data by exploiting their signature and properties, since this is the most probable process. A clean sample of electrons from decay or conversion cannot be isolated from data as expected, because the number of electrons produced is much smaller and the cut selection applied has a too small efficiency to find a reasonable number of candidates.

[31] The truth electrons/positrons originate from a photon.

B Positron event displays

The four positron events in the final sample extracted from the cosmic real data are possible candidates from a bremsstrahlung photon conversion process. Therefore, the individual event displays are examined in detail. All events have in common that only one electron object has been reconstructed. In three of the four event displays the eventual second candidate of the electron pair can be identified by track hits in the ID. The fourth event might be a delta electron with a mismeasured track curvature, or a background event with a faked second track.

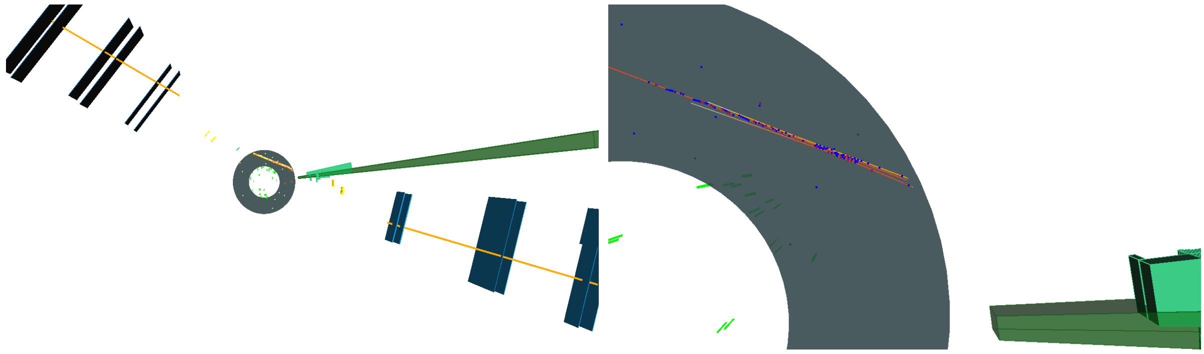

Figure B.1: Event display of a positively charged candidate event (run 90275, event 1456631) in full view (left) and zoomed view (right). The event features three very close-by ID tracks with one overlapping EM cluster.

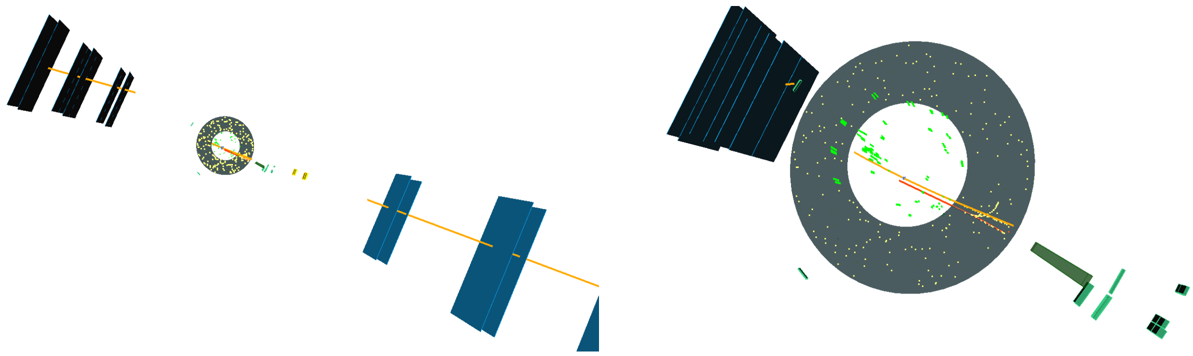

Figure B.2: Event display of a positively charged candidate event (run 91391, event 392571) in full view (left) and zoomed view (right). The event features two tracks in the ID.

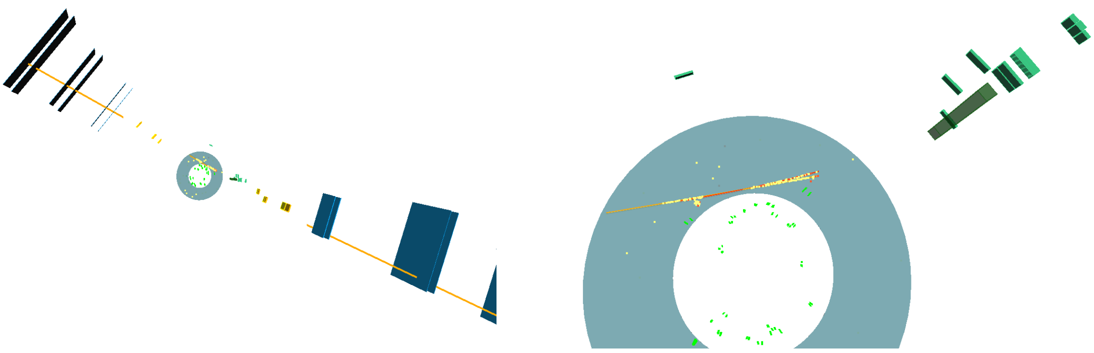

Figure B.3: Event display of a positively charged candidate event (run 91808, event 572857) in full view (left) and zoomed view (right). The event features two reconstructed ID tracks. A particle with a low p_T can be seen by its TRT hits close to the positron ID track.

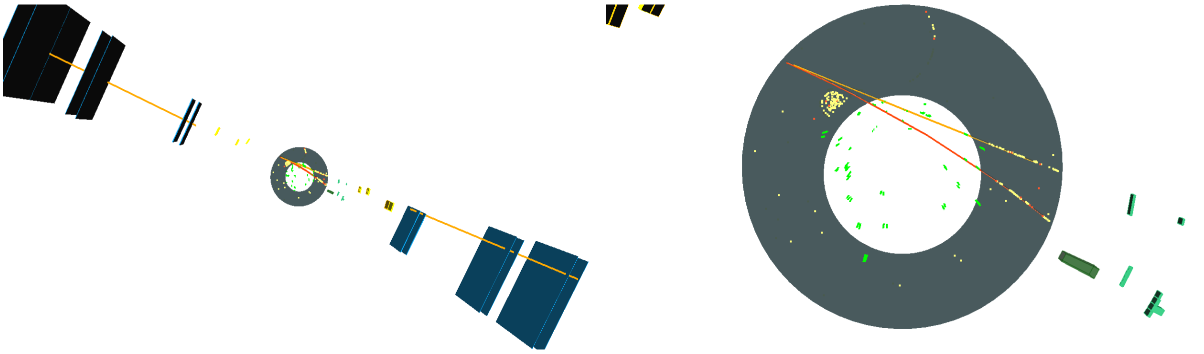

Figure B.4: Event display of a positively charged candidate event (run 91891, event 3470949) in full view (left) and zoomed view (right). The event features two reconstructed ID tracks. A third low momentum track can be seen by its hits in the TRT above the muon ID track in orange.

C Investigation of the trigger information for electrons in cosmic data

In order to investigate the functionality of the level-1 trigger system in cosmic data the different trigger items which were failed or passed are studied for the final tight 34 electron candidates. Since the level-1 trigger only resorts to coarse Calorimeter information, photons and electrons cannot be distinguished. Therefore, also the 13 tight events in the bremsstrahlung sample are investigated. The total number of examined events is thus 47. The pass or fail of high-level trigger chains is not investigated here, since the algorithms for electrons and photons were run in passthrough-mode during cosmic data taking and have only been used for testing the algorithms and filling events in different streams, and not to select events [22]. The exact trigger menu configuration in the different cosmic runs can be found in [21] and [60].

In table C.1 the number of candidates of the two categories are listed which passed different types of level-1 triggers. No prescaling has been applied to these items.[32].

Trigger items	Tight candidates	L1Calo	EM3	TAU5	J5	MU
Electrons	34	24	23	15	15	14
Brem. events	13	8	7	7	7	7

Table C.1: Level-1 trigger items which were passed by the tight electron and bremsstrahlung events. Listed are the number of events in the Calorimeter stream, thus all events found by any Calorimeter trigger, and the number of events found by electron/photon, jet and τ trigger with the respective lowest energy threshold and the number found by different muon triggers.

Only about two thirds of all candidates (30 of 47) have been found by the L1_EM3 trigger, which is the trigger item with the lowest applied threshold used to select electrons and photons. In two cases, only the jet and tau trigger have been passed, while in 15 cases the events have only been selected by one of the muon triggers. The detailed overview of all important physical trigger items which were passed by the investigated events and their correlations is shown in fig. C.1.

In nearly all cases in which trigger items with higher thresholds were passed also the ones with a lower threshold fired, as expected.

To find reasons, why not all electron/photon events have been found by the EM trigger, the efficiency dependent on the offline-reconstructed transverse energy of the 47 candidates is investigated. The efficiency is therefore calculated as the ratio of events which were found by the L1_EM3 trigger in each bin and all reconstructed events in each bin[33]:

$$\epsilon = \frac{N_{\text{candidates that passed L1\_EM3}}}{N_{\text{all reconstructed candidates}}} \tag{C.1}$$

The efficiency curve of the L1_EM3 trigger is shown in fig. C.2.

[32] The notation for the different trigger items is chosen as follows: First, the trigger kind is specified, e.g. 'EM' denotes the electromagnetic trigger for electrons and photons, 'J' denotes the jet, 'TAU' denotes the τ and 'MU' denotes the muon triggers. Next, the cut which is applied on the transverse energy found by the respective trigger algorithms is labeled as a number, e.g. 'L1_EM3' requires an electron or photon with $E_T^{\text{level-1}} > 3$ GeV. An 'I' at the end of the name indicates the application of additional isolation criteria in the Calorimeter [21].

[33] The assigned errors on these efficiencies are calculated according to [61] by applying the Bayes theorem [56] with a Binomial probability and a flat 'prior' distribution in the interval [0,1]. The application of pure Binomial or Poisson uncertainties would result in no or unphysical errors beyond [0,1]. For the calculation of these errors the TGraphAsymmErrors class of the ROOT software is used.

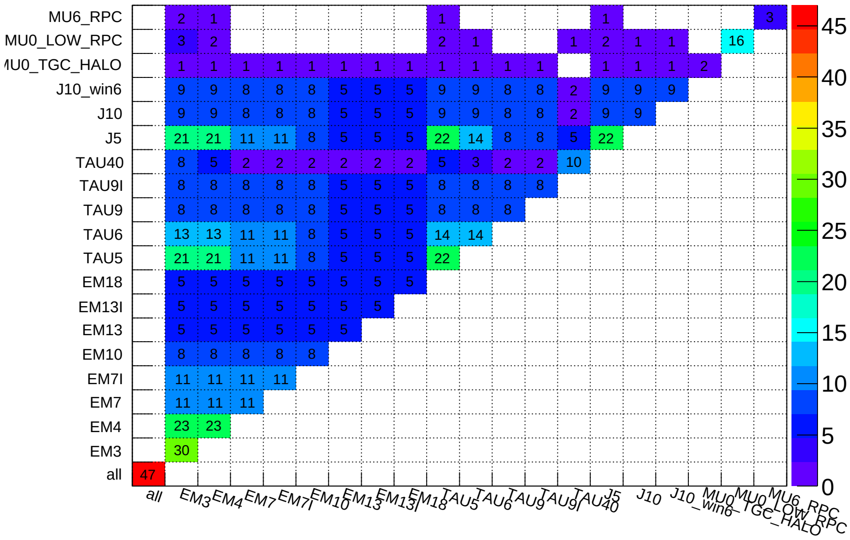

Figure C.1: Number tight electron/bremsstrahlung candidates which pass the important level-1 trigger items.

It can be noticed that many events which have not been found by this trigger feature low energies. In the zoomed view (right) a clear turn-on curve around the trigger threshold of 3 GeV can be observed. The fact that several of the low-energy electrons with transverse energies below 10 GeV fail the trigger threshold can therefore be ascribed to the expected inefficiency of this trigger near its threshold. However, several candidates featuring higher reconstructed energies between 15 and 50 GeV did not pass the trigger threshold, either. Finding an explanation for this is rather difficult, since for the events which have not been found by a Calorimeter trigger, no Calorimeter RoI is stored and no information of the exact energies measured from the trigger algorithms can be gained. The cosmic Monte Carlo sample cannot be investigated, either, since no simulation of the trigger is included. Instead, only the events which passed the trigger threshold can be investigated. For these events the offline-reconstructed energy and the energy found for in the level-1 trigger Calorimeter towers are compared. The difference of these transverse energies can be seen in fig. C.3.

In several cases the reconstructed transverse energy is more than 10 GeV larger than the trigger transverse energy. This might also explain why events with reconstructed energies above 15 GeV failed the L1_EM3 trigger: For the transverse energy found by the level-1 trigger, which uses much coarser Calorimeter information, a much smaller value might have been determined than in the offline reconstruction, and thus the event failed the trigger threshold. These energy discrepancies might be ascribed to the non-projectivity of many of the electrons in cosmic data. They produce showers which cannot efficiently be reconstructed by offline and even less by the coarser trigger algorithms (compare also sec. 8.2).

A second explanation for the non-triggered high-energy candidates might be the special timing situation for cosmic events arriving randomly at the detector. All detection and trigger timings in the subdetectors need to be corrected for the offset of the muon arrival time with respect to the signal of the LHC bunch clock (see sec. 4). If the timing sychronization is not entirely correct, the information on the passed trigger items might be assigned to the previous or subsequent bunch clock signal [19]. This has not been accounted for in the analysis above. Unfortunately, there was not enough time to investigate this further in the framework of this thesis.

In summary, the investigation of the trigger information for the final electron and bremsstrahlung

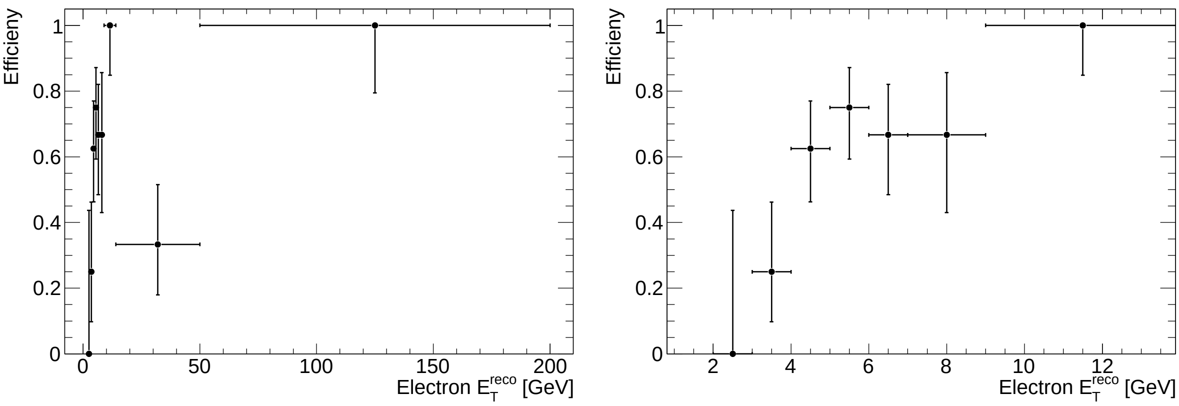

Figure C.2: Zoomed (left) and full (right) view of the efficiency curves for the level-1 electromagnetic trigger with a threshold of $E_T^{\text{level-1}} > 3$ GeV dependent on the offline-reconstructed transverse cluster energy of the 47 electron/bremsstrahlung candidates. To avoid the display of empty bins, a variable bin size is chosen.

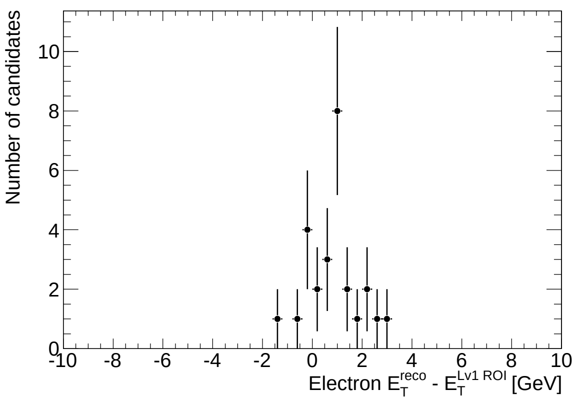

Figure C.3: Difference of the offline reconstructed transverse energy and transverse energy found by the level-1 trigger algorithms in the Calorimeter, displayed for all 32 candidates found by any level-1 Calorimeter trigger. Six events have an energy difference larger than 10 GeV in the overflow and are not displayed.

candidates revealed that in most cases the electromagnetic trigger worked properly. A turn-on curve for the level-1 trigger with the smallest threshold could be extracted. Several candidates with higher reconstructed energies failed the level-1 EM trigger. This might be ascribed to the special topology of cosmic events with non-projective tracks leading to a decrease in the trigger efficiency and the random arrival times with causes problems in the event information storage.

References

[1] S.P. Swordy. The energy spectra and anisotropies of cosmic rays. *Space Science Reviews*, 99:85, 2001.

[2] C. Amsler et al. Particle Data Group: Cosmic rays. *Physics Letters*, B667(1), 2008.

[3] P. L. Biermann and G. Sigl. Introduction to Cosmic Rays. 2002. arXiv:astro-ph/0202425v1.

[4] L. Bergström, J. Edsjö, and P. Ullio. Cosmic antiprotons as a probe for supersymmetric dark matter? 1999. arXiv:astro-ph/9902012v1.

[5] T.K. Gaisser. *Cosmic Rays and Particle Physics*. Cambridge University Press, 1990.

[6] H.V. Klapdor-Kleingrothaus and K. Zuber. *Teilchenastrophysik*. Teubner Studienbücher Physik, Stuttgart, 1997.

[7] C. Amsler et al. Particle Data Group: Summary Tables. *Physics Letters*, B667(1), 2008.

[8] D. Griffiths. *Introduction to Elementary Particles*. Wiley-VCH, 2008.

[9] P. Le Coultre and the L3-C Collaboration. L3+C The atmospheric muon momentum spectrum. *Phys. Lett. B*, 598:15, 2004.

[10] L.N. Bogdanova, M.G. Gavrilov, V.N. Kornoukhov, and A.S. Starostin. Cosmic muon flux at shallow depths underground. 2006. arXiv:nucl-ex/0601019.

[11] ATLAS Homepage. http://www.atlas.ch.

[12] G. Aad et al. *The ATLAS Experiment at the CERN Large Hadron Collider*. ATLAS Collaboration, 2008. Jingst 3 S08003.

[13] C. Amsler et al. Particle Data Group: Passage of particles through matter. *Physics Letters*, B667(1), 2008.

[14] F. Simon. Teilchendetektoren: Grundlagen, Neuerungen. Talk at the 'Herbstschule für Hochenergiephysik Maria Laach' in Bautzen, September 2009.
http://maria-laach.physik.uni-siegen.de/2009/index.php?ID=program.

[15] ATLAS Inner Detector Community. ATLAS Inner Detector Technical design report. 1, 1997. CERN/LHCC/97-16.

[16] ATLAS Collaboration. ATLAS Calorimeter Performance Technical design report. 1997. CERN/LHCC/96-14.

[17] ATLAS Muon Collaboration. ATLAS Muon Spectrometer Technical design report. 1997. CERN/LHCC/97-22.

[18] G. Aad et al. *Expected Performance of the ATLAS Experiment - Detector, Trigger and Physics*. ATLAS Collaboration, 2008. CERN-OPEN-2008-020.

[19] C. Padilla. The ATLAS Trigger System. 2009. ATL-DAQ-PROC-2009-018.

[20] ATLAS Level-1 Trigger Group. Level-1 Trigger Technical Design Report. 1998. ATLAS-TDR-12.

[21] R. Mackeprang. ATLAS TWiki page on Trigger Menus used for cosmic data. https://twiki.cern.ch/twiki/bin/view/Atlas/StartupTriggerMenus.

[22] C. Padilla. Commissioning of the ATLAS High Level Trigger with Single LHC Beam and Cosmic Rays. 2009. ATL-DAQ-PROC-2009-017.

[23] T. Cornelissen. Track fitting in the ATLAS experiment. 2006. Cern-thesis-2006-072.

[24] C. Schmitt. Commissioning of the ATLAS reconstruction software with first data. *Proceedings of the 11th Topical Seminar on Innovative Particle and Radiation Detectors (IPRD08).* ATL-SOFT-PROC-2008-004.

[25] T. Cornelissen. Commissioning of the ATLAS offline software with cosmic rays. *J. Phys.: Conf. Ser.*, 110, 2008.

[26] J. Maneira. Commissioning of the ATLAS Offline Software with cosmic rays. *Nuclear Science Symposium Conference Record IEEE*, 1:204, 2007.

[27] A. Salzburger. The ATLAS Track Extrapolation Package. 2007. ATL-SOFT-PUB-2007-005.

[28] T. Cornelissen. CTBTracking: track reconstruction for the beam and cosmics. 2006. ATL-INDET-INT-2006-001.

[29] T. Cornelissen et al. Concepts, Design and Implementation of the ATLAS New Tracking (NEWT). 2007. ATL-SOFT-PUB-2007-007.

[30] M.J. Costa. Vertex and track reconstruction in ATLAS. *Nucl. Instrum. Meth.*, A582:785–789, 2007.

[31] S. Hassani. A muon identification and combined reconstruction procedure for the ATLAS detector at the LHC using the (MUONBOY, STACO, MuTAg) reconstruction packages. *Nucl. Instrum. Meth.*, A572(1):77–79, 2007.

[32] D. Levin. ATLAS TWiki page on muon reconstruction. https://twiki.cern.ch/twiki/bin/view/AtlasProtected/MuonRecoPedia.

[33] F. Derue. ATLAS TWiki page on electron reconstruction. https://twiki.cern.ch/twiki/bin/view/AtlasProtected/ElectronReconstruction.

[34] W. Lampl et al. Calorimeter Clustering Algorithms: Description and performance. 2008. ATL-LARG-PUB-2008-002.

[35] D. Banfi, L. Carminati, and L. Mandelli. Calibration of the ATLAS electromagnetic calorimeter using calibration hits. 2007. ATL-LARG-PUB-2007-012.

[36] E. Turlay. Electron and Photon Reconstruction and Identification with the ATLAS detector. *Proceedings of the conference Physics at LHC in Split, Croatia, September 29 - 4 October 2008.* ATL-PHYS-PROC-2009-018.

[37] N Kerschen. Electron Reconstruction and Identification with the ATLAS detector. 2009. ATL-COM-PHYS-2009-369.

[38] Input datasets for the 2008 reprocessing campaign. https://twiki.cern.ch/twiki/pub/Atlas/DataPreparationReprocessing/repro08_inputDS.txt.

[39] M. Boonekamp, F. Gianotti, R.A. McPherson, M. Nessi, and P. Nevski. Cosmic Ray, Beam-Halo and Beam-Gas Rate Studies for ATLAS Commissioning. 2004. ATL-GEN-2004-001.

[40] Z. Marshall. The ATLAS Simulation Software. 2008. ATL-SOFT-PROC-2008-001.

[41] Grant Gorfine. Private communication, providing average Inner Detector properties for $\eta = 0$ and $\eta = 1$.

[42] C. Berger. *Elementarteilchenphysik*. Springer, 2002.

[43] C. Amsler et al. Particle Data Group: Kinematics. *Physics Letters*, B667(1), 2008.

[44] C. Grupen. *Teilchendetektoren*. BI-Wiss.-Verl., 1993.

[45] J.D. Jackson. *Classical electrodynamics*. Wiley, New York, 1998.

[46] B. Rossi. *High Energy Particles*. Prentice-Hall Inc., New York, 1952.

[47] D. Groom, N. Mokhov, and S. Striganov. Muon stopping-power and range tables. *Atomic and Nuclear Data Tables, Issue 2*, 78:183, 2001.

[48] S.R. Kelner, R.P. Kokoulin, and A.A. Petrukhin. About cross section for high-energy muon bremsstrahlung. 1995. preprint MSEPI 024-95, Moscow, available as CERN Preprint Server SCAN-9510048.

[49] Y.S. Tsai. Pair production and bremsstrahlung of charged leptons. *Rev. Mod. Phys.*, 46:815, 1974.

[50] H.A. Bethe and W. Heitler. On the Stopping of Fast Particles and on the Creation of Positive Electrons. *Proc. R. Soc.*, A146:83, 1934.

[51] Y.M.. Andreev and E.V. Bugaev. Muon bremsstrahlung on heavy atoms. *Phys. Rev.*, D55:1233, 1996.

[52] J.W. Motz, H.A. Olsen, and H.W. Koch. Pair production by photons. *Rev. Mod. Phys.*, 41:581, 1969.

[53] A.A. Petrukhin and V.V. Shestakov. The influence of the nuclear and atomic form factors on the muon bremsstrahlung cross section. *Canadian Journal of Physics*, 46:377, 1968.

[54] Egamma Identification tools, list of exact PID cuts. http://alxr.usatlas.bnl.gov/lxr-stb4/source/atlas/Reconstruction/egamma/egammaPIDTools/python/egammaElectronCutIDToolBase.py?v=release_15_0_0.

[55] V. Maleev. Validation for egamma: from 14.2 to 15.2. Talk at egamma meeting at 3rd of June 2009 at Cern. http://indico.cern.ch/conferenceDisplay.py?confId=48803.

[56] R.J. Barlow. *Statistics, A guide to the Use of Statistical Methods in the Physical Sciences*. John Wiley & Sons, 1989.

[57] H. Kolanoski. Introductory lecture on fitting. Talk at Fitting Workshop/School at DESY, Hamburg 30th March - 1st April 2009.
https://indico.desy.de/contributionDisplay.py?contribId=1&confId=1582.

[58] A.G. Frodesen, O. Skjeggestad, and H. Toefte. *Probability and statistics in particle physics.* Universitetsforlaget, 1979.

[59] S. Fratina. Approval Request for Cosmic Plots: Level 2 Track Trigger Efficiency in 2008 Cosmic Data. ATLAS approved plots, 2009. ATL-COM-DAQ-2009-016.

[60] ATLAS Run Query Webpage, detailed information on trigger menus/chains used for cosmic data.
http://atlas-service-db-runlist.web.cern.ch/atlas-service-db-runlist/query.html.

[61] M. Paterno. Calculating efficiencies and their uncertainties. 2004. FERMILAB-TM-2286-CD.

[62] J. Kraus, C. Schmitt, L. Serin, and D. Froidevaux. Search for electrons from ionisation in 2008 cosmic-ray data. ATLAS approved plots, May 2009. ATL-COM-PHYS-2009-238.

[63] J. Kraus. Studies of electrons from cosmic event data in ATLAS, proposal for approved plots. Plenary talk, April 2009.
http://indico.cern.ch/conferenceDisplay.py?confId=50680#12.

[64] J. Kraus, C. Schmitt, and E. von Toerne. First observation of electrons in the ATLAS detector. Internal note, December 2009. ATL-PHYS-INT-2009-112.